Identifying signatures of and designing searches for unexplored SUSY models with the CMS detector

(Identifizierung von und Suche nach nicht untersuchten SUSY Modellen mit dem CMS Detektor)

Master Thesis in Physics

by

Malte Mrowietz

(6338104)

(born: 22.06.1991)

angefertigt im

Institut für Experimentalphysik

vorgelegt der

Fakultät für Mathematik, Informatik und Naturwissenschaften

Universität Hamburg

DER FORSCHUNG | DER LEHRE | DER BILDUNG

1. Gutachter : Prof. Dr. Peter Schleper

2. Gutachter : Prof. Dr. Johannes Haller

Hamburg, den 16.04.2018

Zusammenfassung

Ergebnisse von ATLAS und CMS am LHC am CERN schränken bereits jetzt Supersymmetrie auf der elektroschwachen Skala ein. Vor allem natürliche Szenarien sind zu einem großen Teil ausgeschlossen. Diese Arbeit nutzt einen Parameterscan des phänomenologischen minimalen supersymmetrischen Standart Models (pMSSM) um Supersymmetrie auf niedriger Skala genauer zu untersuchen. Das Programm `SmodelS` wird benutzt um die Punkte des Parameterscans in ihr Spektrum von vereinfachten Modellen zu zerlegen und diese gegen ATLAS und CMS Analysen zu testen. Vereinfachte Modelle mit nahezu massenentarteten Gauginos tauchen sehr häufig in dem Parameterscan auf. Es wird gezeigt, dass die Natürlichkeit von diesen vereinfachten Modellen vergleichsweise niedrig ist. Der natürlichste Parameterpunkt wird bezüglich seines Hauptprozesses $\widetilde{\chi}_2^0\,\widetilde{\chi}_1^\pm \rightarrow \mathrm{Z}^*\mathrm{W}^*\widetilde{\chi}_1^0\,\widetilde{\chi}_1^0$ im hadronischen Zerfallskanal des Z^* mit dem CMS Detektor untersucht. In diesem Zusammenhang wird zusätzlich zu einer Ereignisselektion eine simultane Optimierung von Spurobservablen und Ereignisobservablen durchgeführt. Es konnte eine Signifikanz von $\Sigma = 0.1116$ erreicht werden.

Abstract

Experimental results from the ATLAS and CMS experiments at the CERN LHC already challenge electroweak-scale supersymmetry, and its naturalness in particular. In this thesis, a scan of the phenomenological minimal supersymmetric Standard Model (pMSSM) is employed to study this further. The tool `SmodelS` is used to derive simplified model spectra and to compare corresponding ATLAS and CMS results to predictions of pMSSM parameter points. Compressed gaugino models are identified as the type of simplified model that occurs most often in the simplified model spectra of the studied pMSSM parameter points. A study on the naturalness of these models reveals that compressed gaugino models tend to occur in pMSSM parameter points with comparatively low levels of fine tuning. The pMSSM parameter point with the lowest level of fine tuning is selected for a sensitivity study. The main process in this pMSSM point is $\widetilde{\chi}_2^0\,\widetilde{\chi}_1^\pm \rightarrow \mathrm{Z}^*\mathrm{W}^*\widetilde{\chi}_1^0\,\widetilde{\chi}_1^0$, for which a search at the CMS detector is developed targeting the hadronic channel of the virtual Z boson. An event selection, as well as a simultaneous optimization of track observables and event-level observables, was developed. The best significance reached is $\Sigma = 0.1116$.

Contents

1 Introduction

The Standard Model of particle physics has been enormously successful in describing experimental results from first principles within a consistent quantum field theory. However, it fails to describe a number of important phenomena, such as dark matter and gravity. It also has some aesthetic problems, such as the large number of 19 free parameters, and the hierarchy problem. Supersymmetry seems ideally suited to address these issues, while at the same time, it allows the Standard Model to emerge as a low-energy effective field theory of more fundamental theories at high scales. If supersymmetry is to solve the hierarchy problem, it has to manifest at the TeV scale. This makes searches for supersymmetry particularly interesting for the LHC[1]. Since the first collisions at the LHC in 2010, many searches for new physics have been performed. Many of the searches were guided by and interpreted in terms of simplified models, in hopes that new physics will resemble some region in the simplified model parameter space. However, no new particle has been found yet. Now that the most obvious signatures have been searched for, it is time to look to more exotic signatures. The possibility to identify such signatures exists within the tool `SmodelS`, which works by decomposing complete models such as supersymmetry into their simplified model spectra and testing the spectra against CMS[2] and ATLAS results. Simplified models in the spectra that are not constrained by CMS or ATLAS are ideal candidates for further investigation.

In this thesis, a small set of non-excluded points from a pMSSM parameter scan is tested by `SmodelS`, with the aim of identifying signatures in the pMSSM that warrant a dedicated search. After the identification of one such simplified model, a case study is performed using CMS 2016 simulations. In the context of this study, a simultaneous optimization with respect to sensitivity of an object selection and an event-level observable was performed.

[1]**L**arge **H**adron **C**ollider
[2]**C**ompact **M**uon **S**olenoid

2 The Standard Model of particle physics

The Standard Model (SM) of particle physics is a lagrangian quantum field theory describing three of the four known fundamental interactions and all known fundamental particles. Particles in quantum field theories are excitations of the quantum fields therein. Interactions and correlations between different field configurations are, where possible, calculated as a perturbation series, where the different orders can be interpreted in the Feynman diagram formalism as the interaction of particles. The interactions between the particles of the Standard Model are introduced via the local gauge symmetries of the lagrangian of the Standard Model. As of 2012, with the discovery of a Higgs boson, all predicted particles of the Standard Model have been found.
Section 2.1 gives a summary on how local gauge symmetries induce interactions between fields. Feynman diagrams are briefly explained in Section 2.2. Section 2.3 discusses the symmetries of the Standard Model. The particle content of the Standard Model is given in Section 2.5, the interactions that occur in the Standard Model are discussed in Section 2.6. Finally, open questions whose answers must necessarily lie outside the Standard Model are discussed in Section 2.8. For a comprehensive description of the Standard Model, consider [1, 2, 3, 4].

2.1 Local Gauge Symmetries

In field theory, a local gauge symmetry is the form invariance of a physical quantity, usually the Lagrangian, under a gauge transformation of the fields. Local gauge symmetries naturally lead to interactions between a given field and the gauge field associated to the symmetry.
Consider the following Dirac Lagrangian, containing only the kinetic term of a spinor field Ψ:

$$\mathscr{L} = i\bar{\Psi}\gamma^{\mu}\partial_{\mu}\Psi \tag{1}$$

We require that the Lagrangian should be form invariant under transformations of the field Ψ of the form:

$$\Psi \to \Psi' = U\,\Psi\ ,\ \bar{\Psi} \to \bar{\Psi}' = \bar{\Psi}U^{\dagger}\ ,\ \text{where } U = e^{iqW_aT^a} \text{ is unitary,} \tag{2}$$

where q is the charge associated to the symmetry, W_a are scalar functions depending on spacetime coordinates, and T^a the generators of the transformation. In the case of the gauge symmetries of the Standard Model, the generators are hermitian matrices that satisfy the commutation relation $[T_a, T_b] = if_{abc}T_c$, where f_{abc} is a real number. Applying this type of transformation to

Equation 1 yields

$$
\begin{aligned}
\mathscr{L} \to \mathscr{L}' &= i\bar{\Psi}'\gamma^{\mu}\partial_{\mu}\Psi' \\
&= i\bar{\Psi}U^{\dagger}\gamma^{\mu}\partial_{\mu}U\Psi \\
&= i\bar{\Psi}\gamma^{\mu}U^{\dagger}U\partial_{\mu}\Psi + i\bar{\Psi}\gamma^{\mu}U^{\dagger}[\partial_{\mu},U]\Psi \\
&= i\bar{\Psi}\gamma^{\mu}\partial_{\mu}\Psi + i\bar{\Psi}\gamma^{\mu}U^{\dagger}[\partial_{\mu},U]\Psi \ , \qquad (3)
\end{aligned}
$$

where $[\partial_{\mu},U]$ is the commutator between ∂_{μ} and U. For global symmetries, the commutator vanishes trivially, as the operator U does not depend on the coordinates x_{μ}. However, for local symmetries this commutator evaluates as

$$
\begin{aligned}
[\partial_{\mu},U]\Psi =&\partial_{\mu}(U\Psi) - U\partial_{\mu}\Psi \qquad (4) \\
=&(\partial_{\mu}U)\Psi + U\partial_{\mu}\Psi - U\partial_{\mu}\Psi \qquad (5) \\
=&iq(\partial_{\mu}W_a)T^a\,U \quad , \qquad (6)
\end{aligned}
$$

where the definition of U in Equation 2 was used in the last step. This term does not usually vanish, breaking the invariance of the Lagrangian under the transformation U. In order to construct a gauge invariant Lagrangian, i.e. one that is invariant under transformations U, the partial derivative is replaced by the covariant derivative D_{μ}, given by

$$D_{\mu} \equiv \partial_{\mu} + iqA_{\mu}. \qquad (7)$$

A_{μ} is a newly introduced vector field that transforms like

$$A'_{\mu} = A_{\mu} - \partial_{\mu}W^aT_a = UAU^{\dagger}. \qquad (8)$$

The last term in Equation 8, which contains the derivative, exactly cancels the extra term obtained by the partial derivative in Equation 3, leaving the Lagrangian invariant. The newly introduced field A_{μ} is the gauge field corresponding to the symmetry transformation. In order to consistently describe it, a kinetic term for the gauge field has to be added to the Lagrangian. It then has the form

$$
\begin{aligned}
\mathscr{L}_{kin} = i\bar{\Psi}\gamma^{\mu}D_{\mu}\Psi - \frac{1}{4}W_a^{\mu\nu}W_{a\mu\nu} \quad , \qquad (9) \\
\text{where } W_a^{\mu\nu} = D^{\mu}W_a^{\nu} - D^{\nu}W_a^{\mu} + g\sum_{bc} f^{abc}W_b^{\mu}W_c^{\nu}
\end{aligned}
$$

is the field strength tensor. The introduction of the covariant derivative automatically introduces terms in the Lagrangian which are proportional to $\bar{\Psi}\gamma^{\mu}A_{\mu}\Psi$ and describe the interaction of the spinor field Ψ and the gauge field A. Additional terms of order $\mathscr{O}(A^3)$ and $\mathscr{O}A^4)$ appear as a result of the kinetic term of the gauge field, provided the symmetry group to which A corresponds is non-abelian, i.e. the commutators of the generators are non-zero. These terms describe the self interaction between gauge bosons.

2.2 Feynman Diagrams

Systems in quantum field theories (QFT) are described by correlation functions of field configurations, also called N-point Green's functions. The transition amplitude for a state $|i\rangle$ to transition into a state $\langle f|$ is given by $\langle f| S_{fi} |i\rangle$, where S is the S-matrix. Perturbative approaches to quantum field theory have yielded enormous success in calculating transition amplitudes and describing the measured distributions of observables at particle accelerators. In perturbative QFT, the S-matrix is calculated as a perturbation series in orders of the interaction Lagrangian. Historically, one of the most illuminating developments in quantum field theory is the formalism of Feynman diagrams. The perturbation series can be interpreted in a diagrammatic way as the interaction between particles at vertices. The number of vertices in a Feynman diagram corresponds to the order of the term in the perturbation series.
The symbols of Feynman diagrams are the following:

- Incoming fermions and outgoing antifermions are represented by a line with an arrow pointing towards the vertex.

- Outgoing fermions and incoming antifermions are represented by a line with an arrow pointing away from the vertex.

- Gauge bosons are represented by yvy line.

- Colored gauge bosons are represented by a spiraling line.

- Scalar bosons are represented by a dashed line.

In this thesis, Feynman diagrams with supersymmetric particles are used. In these, all supersymmetric particles are represented by a wavy line, overlaid with a straight line that has no arrow.

Conservation laws correspond to quantum numbers which are conserved at every vertex. Figure 3 describes the leading order interaction terms of the interaction Lagrangian introduced in Section 2.1.

2.3 Symmetries of the Standard Model

The underlying symmetry of the Standard Model is the symmetry of spacetime under transformations of the Poincaré group, which include translations in space and time, as well as rotations in space, and Lorentz boosts.
According to Noether's theorem, symmetries lead to conserved currents that are associated with the generators of transformations, as well as the conservation in time of the zero'th component of the current: the charge. The Poincaré symmetry of the Standard Model leads to the well known conservation of energy, momentum and angular momentum.

In addition to the spacetime symmetries, the Standard Model contains three internal local gauge symmetries:

- $\mathrm{SU(3)_C}$ symmetry: C refers to the color charge. By convention, the color charges are red, blue, and green.
- $\mathrm{SU(2)_L}$: L refers to the left handed component of chirality (see Section 2.4). The associated charge is the isospin, which can take on values of $+\frac{1}{2}$ and $-\frac{1}{2}$.
- $\mathrm{U(1)_Y}$: Y is the hypercharge. Y can take the values +1, 0 and -1. It is noted that the hypercharge is not the electric charge.

The generators of SU(3) give rise to the gluons, the mediators of the strong interaction. The $\mathrm{SU(2)_L}$ and the $\mathrm{U(1)_Y}$ symmetries are unified in the electroweak theory to the group $\mathrm{SU(2)_L} \times \mathrm{U(1)_Y}$. It is spontaneously broken and gives rise to the electric charge Q, as well as the well known gauge bosons, the photon, the Z boson, and the W boson, which are the mediators of the electromagnetic and weak interactions. Finally, the spontaneously broken symmetry results in massive gauge bosons via the Higgs mechanism. The massive Higgs boson is an additional consequence of the symmetry breaking.

2.4 Chirality

The $\mathrm{SU(2)_L}$ transformations of the Standard Model act only on left chiral fields, the transformation of right handed fields under $\mathrm{SU(2)_L}$ is the identity transformation.
The fermion fields of the Standard Model can be expressed in terms of their left handed and right handed chiral components using the projection operators

$$\mathrm{P_L} = \frac{1-\gamma^5}{2} \ , \ \mathrm{P_R} = \frac{1+\gamma^5}{2} \ , \tag{10}$$

such that

$$\Psi = \mathrm{P_L}\Psi + \mathrm{P_R}\Psi \equiv \Psi_\mathrm{L} + \Psi_\mathrm{R} \quad . \tag{11}$$

The fermion fields thus transform as $\Psi_\mathrm{L} \to e^{i\Phi_\mathrm{L}}\Psi_\mathrm{L}$ and $\Psi_\mathrm{R} \to \Psi_\mathrm{R}$. The chiral nature of fermions leads to parity violating processes [5].

2.5 Particle Content

The particles of the Standard Model are the different fundamental representations of the Poincaré algebra. All particles with the same spin are in the same representation. The spin-$\frac{1}{2}$ fermion fields are introduced in an ad-hoc manner required by experimental results, while the spin-1 boson fields are naturally introduced by the internal symmetries of the Standard Model. They are in the adjoint representation of their respective internal symmetry group, which means they transform as $A_\mu \to UA_\mu U^\dagger$ under transformations U. Figure 1 shows the particle content of the Standard Model, as well as their respective electric charges, their spin and their masses. To each fermion in that figure, there also exists a corresponding antiparticle with opposite charges.

The fermion sector of the Standard Model is shown in Table 1. It contains two types of particles, the quarks and the leptons. There are 6 types of quarks, ordered in generations of $\mathrm{SU(2)_L}$ doublets and by their weak isospin. The right handed fields are not in $\mathrm{SU(2)_L}$ doublets but are instead singlet states, which do not transform under $\mathrm{SU(2)_L}$ transformations. The up quark (u), charm quark (c), and top quark (t) make up the so called up-type quarks. They have a weak isospin of $\frac{1}{2}$ and a fractional electric charge of $Q = \frac{2}{3}$. The down quark (d), strange quark (s), and bottom quark (b) make up the down-type quarks. They carry a weak isospin of $-\frac{1}{2}$ and an electric charge of $Q = -\frac{1}{3}$.The $\binom{u}{d}$ is the first generation doublet, the $\binom{c}{s}$ the second generation doublet and the $\binom{t}{b}$ the third generation doublet. All quarks also carry one unit of color charge.

As with the quarks, the leptons are ordered in generational $\mathrm{SU(2)_L}$ doublets. Each doublet contains an integer charged lepton with a weak isospin of $-\frac{1}{2}$ and an electrically neutral lepton with a weak isospin of $\frac{1}{2}$, its corresponding neutrino. Ordered by ascending generation, the doublets are $\binom{\nu_e}{e^-}$, $\binom{\nu_\mu}{\mu^-}$, $\binom{\nu_\tau}{\tau^-}$. The e^- is the electron, the μ^- is called the muon and the τ^- is called the tau lepton. The ν_e, ν_μ and ν_τ are the electron-, muon- and tau neutrino, respectively. The fermion masses increase towards the higher generation, except in the case of the neutrinos, for which the mass hierarchy is unknown.

The boson sector contains the spin-1 gauge bosons corresponding to the $\mathrm{SU(2)_L} \times \mathrm{U(1)_Y}$ symmetry, which are the photon, the Z boson and the W bosons, as well as the gauge bosons of the $\mathrm{SU(3)_C}$, the gluons. Additionally, there is the spin-0 Higgs boson, a byproduct of the spontaneously broken $\mathrm{SU(2)_L} \times \mathrm{U(1)_Y}$ symmetry, which couples to the particle masses. The photon and the Z boson are electrically neutral and also carry no color charge. The W bosons carry electric charges of ± 1, but no color charge. The Z boson and the W boson couple to the weak isospin and are responsible for the decay of particles. The gluons are the only color charged bosons, but couple neither to electric charge nor to the isospin.
Figure 2 gives a comprehensive overview of the field content of the Standard Model, as well as their interactions.

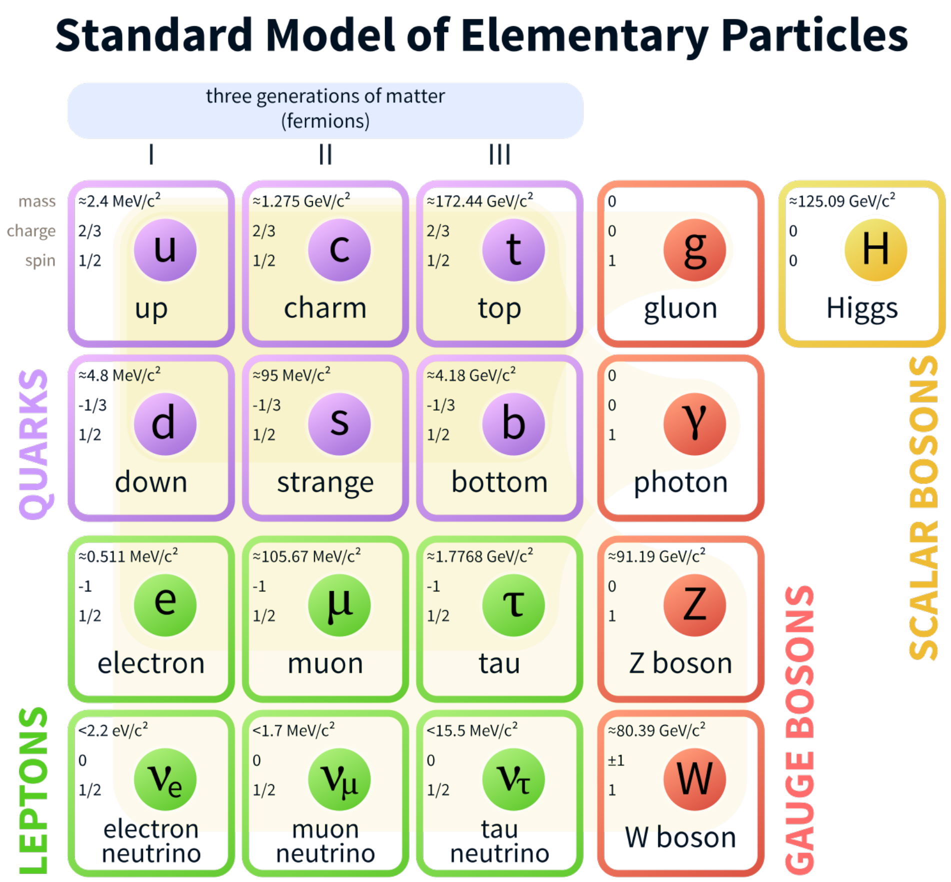

Figure 1: Particle content of the Standard Model. The quarks (purple) and leptons (green) make up the fermions, the gauge bosons (red) mediate the interactions between particles, and the Higgs boson (yellow) is related to the mechanism that gives the particles their masses. Figure taken from [6].

	1st Generation	2nd Generation	3rd Generation
Leptons	$\binom{\nu_e}{e_L}$, e_R	$\binom{\nu_\mu}{\mu_L}$, μ_R	$\binom{\nu_\tau}{\tau_L}$, τ_R
Quarks	$\binom{u_L}{d_L}$, u_R , d_R	$\binom{c_L}{s_L}$, c_R , s_R	$\binom{t_L}{b_L}$, t_R , b_R

Table 1: Fermion content of the Standard Model. Leptons and Quarks come in three generations of ascending mass. Left chiral fields, denoted by L, are in $SU(2)_L$ doublets, while right handed fields R are singlets of that symmetry. Neutrinos do not have a right handed component in the Standard Model.

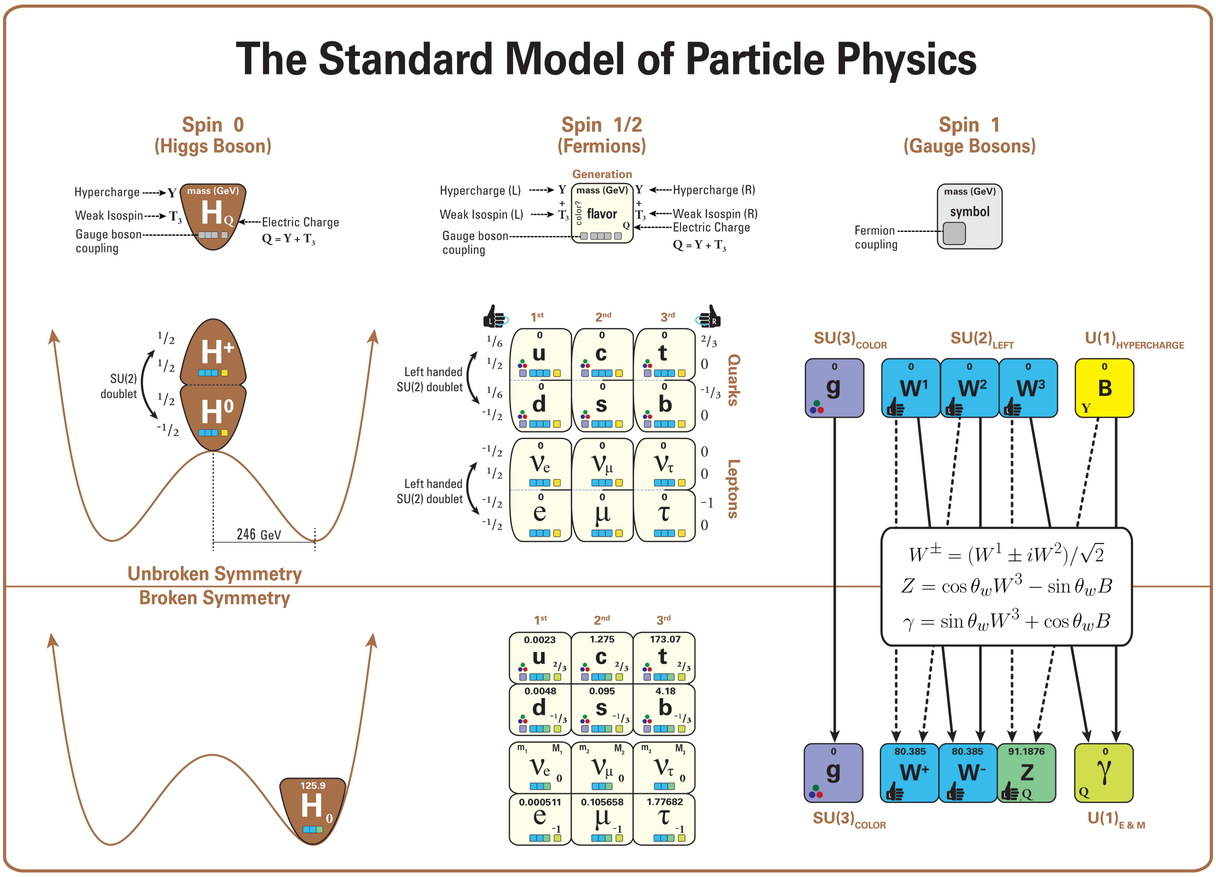

Figure 2: The field content of the Standard Model before and after symmetry breaking. The left side of the Figure is an illustration of the Higgs potential. The Standard Model is symmetric with respect to the center point of the potential. However, the vacuum state occupies the minimum of the potential, freeing up the remaining degrees of freedom to be "eaten" via the Higgs mechanism to create the gauge boson masses. Figure taken from [7].

2.6 Particle interactions

The main strength and goal of quantum field theories is that they enable to calculate correlation functions between field configurations, as well as the probability amplitude for certain processes to occur. These can usually be expressed and calculated as a perturbation series, and interpreted as the interactions between particles. The different orders and integrals that appear in the perturbation series can be interpreted in a diagrammatic way within the formalism of Feynman diagrams. Historically, the interactions of the Standard Model have been separated into three separate theories: Quantum Electrodynamics (QED), Weak interaction Theory (WT) and Quantum Chromodynamics (QCD):

QED
QED describes the interactions of fermions with photons as a $\mathrm{U(1)_Q}$ gauge theory, where Q is the electric charge. The fundamental interaction of QED is depicted in Figure 3.

WT
Weak Theory describes the interactions of particles with the Z boson and the W boson ($\mathrm{SU(2)_L}$ gauge theory). This symmetry group is non-abelian, which leads to interactions between the Z and W bosons. The fundamental interactions of WT are depicted in Figure 4. QED and WT have since been unified into the electroweak theory (EWT) with the underlying $\mathrm{SU(2)_L \times U(1)_Y}$ symmetry group spontaneously broken into the $U(1)_\mathrm{Q}$ symmetry of QED.

QCD
QCD describes the interactions of the colored particles in the Standard Model, the quarks and gluons. The fundamental interactions of QCD are depicted in Figure 5.

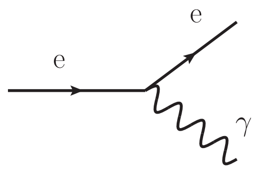

Figure 3: Fundamental interaction of QED. All physical processes in QED can be constructed from this diagram using the Feynman rules. Feynman diagram produced with `Jaxodraw`[8].

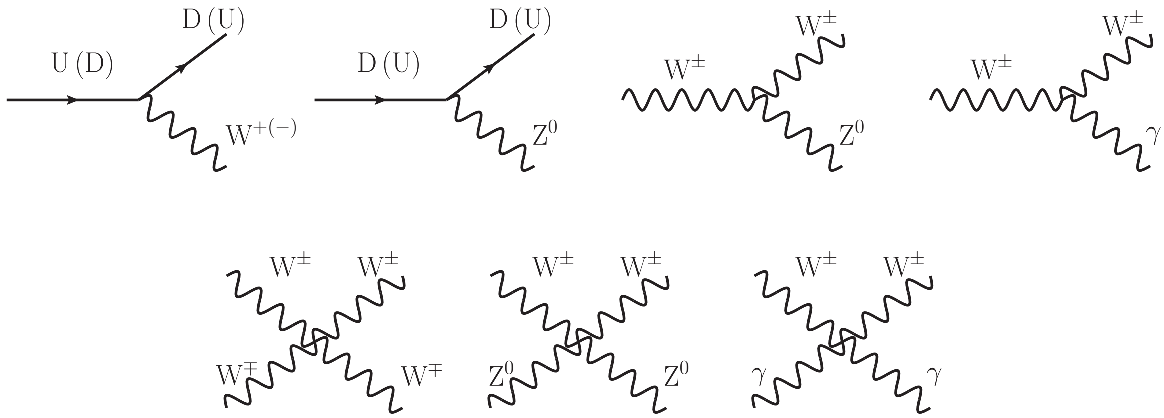

Figure 4: Fundamental interactions of the Weak Theory. U denotes left handed fermions with an isospin of $+\frac{1}{2}$, D refers to the $-\frac{1}{2}$ isospin component of a $\mathrm{SU(2)_L}$ doublet. The non-abelian nature of the $\mathrm{SU(2)_L}$ leads to the self-interaction diagrams of the gauge bosons. Feynman diagrams produced with `Jaxodraw`[8].

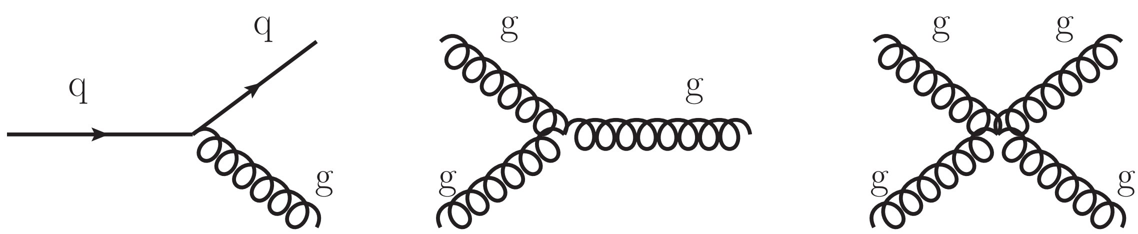

Figure 5: Fundamental interaction of QCD. The q denotes a quark, g denotes a gluon. Self interactions of gluons arise from the non-abelian nature of $\mathrm{SU(3)_C}$. Feynman diagrams produced with `Jaxodraw`[8].

2.7 Fermion Masses

Due to their chiral nature, the straightforward fermionic mass term $\mathscr{L}_{\text{Mass}} = m\bar{\Psi}\Psi$ is not gauge invariant. Instead, fermions acquire their mass through interaction with the Higgs field, so-called Yukawa interactions. They have the form

$$\mathscr{L}_{\text{Yukawa}} = Y\bar{\Psi}_{\text{L}} H \Psi_{\text{R}} \quad , \tag{12}$$

where Y is the Yukawa coupling and H the Higgs field. The Yukawa coupling is related to the fermion mass m_f by $Y = \frac{m_f}{v}$, where v is the Higgs field vacuum expectation value. Because the Yukawa coupling is proportional to the fermion mass, the Higgs boson couples primarily to the top quark, with a Yukawa coupling strength of order $\mathscr{O}(1)$. This is why one of the main production channels of the Higgs boson at the LHC is through a loop made of top quarks.

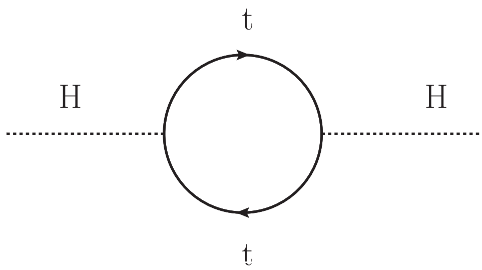

Figure 6: Fermion loop contribution to the Higgs mass.

2.8 Shortcomings of the Standard Model

Although the Standard Model is hugely successful in describing most experimental results, there are physical phenomena that the Standard Model is not able to explain. Some of these shortcomings are introduced below.

Gravity

Gravity cannot be described by a renormalizable quantum field theory [9, 10]. The field candidate for gravity, with its corresponding particle, the graviton, is not renormalizable. For this reason, gravity is not included in the Standard Model.

Hierarchy Problem

The inclusion of a scalar particle with a mass at the scale of the electroweak gauge bosons $\mathscr{O}(100\,\mathrm{GeV})$, introduces the hierarchy problem. Fermion loop contributions to the Higgs boson mass (see Figure 6) diverge quadratically with the renormalization cutoff scale, suggesting a mass of the Higgs boson at the Planck scale. In order for the Higgs boson mass to be at the electroweak scale, excessive fine tuning would have to occur among the other parameters. The leading term for the radiative corrections of a fermion to the Higgs boson mass is [11]:

$$\delta m_H^2 = -\frac{|\lambda_f|^2}{8\pi^2}\Lambda_{UV}^2 \quad , \tag{13}$$

where λ_f is the Yukawa coupling of the fermion contributing to the loop and Λ_{UV} is a cutoff scale introduced during renormalization.

Dark Matter

The existence of dark matter is well established by astrophysical observations like the rotation curves of galaxies [12], gravitational lensing phenomena [13], as well as observations of the cosmic microwave background [14]. However, no particle in the Standard Model has the properties necessary to be dark matter. A dark matter candidate must fulfill two conditions: It must be a stable particle, and it must not interact electromagnetically or via the strong force, otherwise it would have been observed directly by now.

Unification of Coupling Constants

A requirement on a grand unified theory, from which the Standard Model emerges as a low-energy limit, is that the running coupling constants unify at some large scale. As can be seen in Figure 7, within the Standard Model, the coupling constants of QED, EWT and QCD never unify at any scale.

3 Supersymmetry

This section is based on [15].
Supersymmetry (SUSY) is the only possible extension of the Poincaré algebra that is allowed while still preserving the Standard Model [16]. In addition to the bosonic generators of the Poincaré algebra, fermionic generators are introduced. The additional structure that is added to the Poincaré algebra is:

$$\{Q_\alpha, \bar{Q}_\beta\} = 2(\sigma^\mu)_{\alpha\beta}\, P_\mu, \tag{14}$$

$$[\Lambda^{\mu\nu}, Q_\alpha] = \frac{1}{2}\left(\frac{i}{2}[\gamma^\mu, \gamma^\nu]\right)_\alpha^{\ \beta} Q_\beta \tag{15}$$

$$[Q_\alpha, P^\mu] = 0 \quad , \tag{16}$$

where Q and $\bar{Q}$ are new spinors, σ^μ are the Pauli matrices, P_μ is the momentum operator, γ^μ are the Dirac matrices and $\Lambda^{\mu\nu}$ is the generator of Lorentz transformations. The newly introduced spinors Q have the property that

$$\begin{aligned} Q\,|\text{boson}\rangle &\sim |\text{fermion}\rangle \\ Q\,|\text{fermion}\rangle &\sim |\text{boson}\rangle \quad . \end{aligned} \tag{17}$$

This results in at least a doubling of the field content compared to a non-supersymmetric theory. These new fields or particles are called superpartners or sparticles and have the spin of their Standard Model counterparts reduced by $\frac{1}{2}$. The superpartners of the Standard Model fermions are thus spin-0 bosons, which by convention get the name of the Standard Model particle with an "s" in front ("sfermion" in general), e.g. top $\rightarrow$ stop ("scalar top"). The superpartners of the gauge bosons of the Standard Model are spin-$\frac{1}{2}$ fermions. They take the name of their Standard Model counterpart, combined with the suffix "ino", e.g. Wino, Photino. They are sometimes also called gauginos.

An exact symmetry would lead the supersymmetric particles to have the same mass as their Standard Model counterpart. As this is ruled out by experiments, if SUSY exists, it must be a broken symmetry. It is usually assumed that SUSY is an exact symmetry that is spontaneously broken, as opposed to an explicitly broken symmetry. In this case, SUSY is formulated at a high scale in a so-called "hidden sector", which is decoupled from the scale of Standard Model interactions. The spontaneous breaking of SUSY then results in a visible sector at the scale of Standard Model interactions.

3.1 Motivation

SUSY directly addresses several shortcomings of the Standard Model. The hierarchy problem is solved by loop contributions of supersymmetric particles to the Higgs boson mass that counteract the loop contributions of the Standard Model particles. The supersymmetric partners of the fermions and their Standard Model counterparts share the same Yukawa coupling and would also contribute to the radiative corrections. However, their bosonic nature leads to a change in sign of the contribution in Equation 13, exactly canceling the quadratic divergence. The radiative corrections to the Higgs boson mass would no longer scale quadratically but logarithmically, like [15]

$$\delta m_H^2 = -\frac{|\lambda_f|^2 m_S^2}{8\pi^2} \ln(\frac{\Lambda_{UV}}{m_S}) \quad , \tag{18}$$

where m_S is the mass scale of the supersymmetric particle. If SUSY is not present at the TeV scale however, this solution to the hierarchy problem introduces the so-called "little hierarchy problem", where the radiative corrections to the Higgs boson mass again become large due to the quadratic dependence on the mass of the supersymmetric particles in Equation 18.

SUSY naturally accommodates a dark matter candidate by requiring the conservation of an additional quantum number called R-parity, defined as

$$P_R = (-1)^{(B-L)+2S} \quad , \tag{19}$$

where B and L are the baryon and lepton number and S is the particle spin. Standard Model particles have a value of $P_R = 1$, while supersymmetric particles have $P_R = -1$. If we require R-parity conservation, supersymmetric particles can only be created or annihilated in pairs, resulting in a stable lightest supersymmetric particle (LSP), which can neither decay to other supersymmetric particles due to the kinematic mass constraint, nor to Standard Model particles, as this would violate R-parity. If the lightest supersymmetric particle is also electrically neutral and carries no color charge, it can serve as a dark matter particle. Lastly, a SUSY interpretation of dark matter is compatible with the dark matter relic density observations from cosmology [17]. The presence of such **w**eakly **i**nteracting **m**assive **p**articles (WIMPs) in the gaugino sector of supersymmetry is often called the WIMP miracle [17].
Introduction of SUSY at the TeV scale modifies the renormalization group equations of the running coupling constants of the Standard Model gauge group. This modification allows for the unification of the coupling constants at the scale of grand unified theories, which is a key requirement of a grand unified theory (see also Figure 7).

Finally, while SUSY does not intrinsically include gravity, the only mathematically consistent quantum theory of gravity that is known today, superstring theory, requires that there is supersymmetry at some scale, although not necessarily at the TeV scale.

3.2 The Minimal Supersymmetric Standard Model

The Minimal Supersymmetric Standard Model (MSSM) is the minimal way that the Standard Model can be extended to include SUSY, containing a minimal number of new parti-

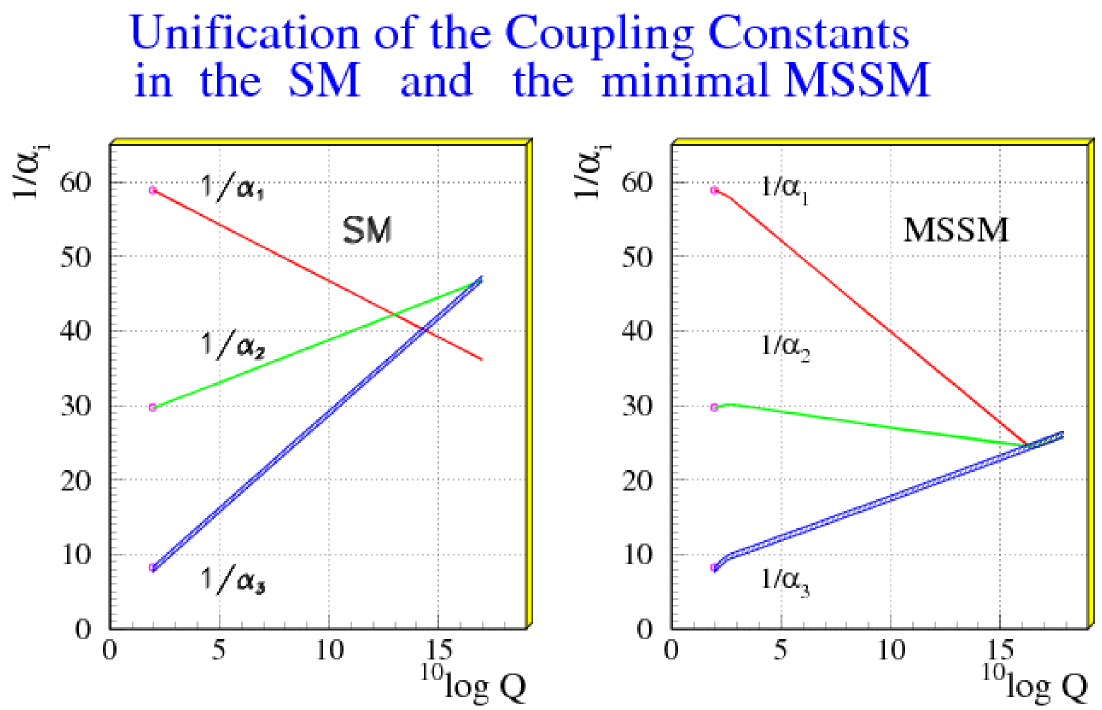

Figure 7: Scaling behavior of the coupling constants in the Standard Model (left) and the TeV-scale MSSM (right). The coupling constants never unify at any scale Q in the Standard Model, while a unification at the scale of grand unified theories is possible in the MSSM [18].

cles and interactions. The Higgs sector of the Standard Model is extended by a second Higgs $SU(2)_L$ doublet. Each of the two Higgs doublets gets a superpartner, a spin-0 higgsino doublet. This leads to five physical Higgs bosons:

- A Standard Model like scalar Higgs boson h;
- A heavy scalar Higgs boson H;
- A CP-odd scalar Higgs boson A^0;
- A pair of charge conjugate scalar Higgs bosons $H^{\pm}$.

All of the Higgs bosons have an R-parity of $P_R = 1$.

Electroweak Gaugino Mixing

The flavor eigenstates of the gauginos are not aligned with their mass eigenstates. This leads to mixing in the electroweak gaugino sector similar to the quark sector in the Standard Model. The flavor eigenstates of the winos mix with the charged higgsino eigenstates to form two charged mass eigenstates, $\tilde{\chi}_1^{\pm}$, and $\tilde{\chi}_2^{\pm}$, called charginos. The photino, neutral higgsinos, and the Zino form four mass eigenstates $\tilde{\chi}_1^0$, $\tilde{\chi}_2^0$, $\tilde{\chi}_3^0$, and $\tilde{\chi}_4^0$, called neutralinos. The mass eigenstates are defined in order of ascending mass, making the state with the index "1" the lightest neutralino or chargino, respectively. The MSSM contains 105 new parameters in addition to the Standard

Model parameters and features a huge number of possible realizations. Many of these versions of the MSSM present features that are already excluded by experimental constraints on, e.g. large flavor changing neutral currents [19], or a large electric dipole moment of the neutron [20, 21], and are thus not interesting from an experimental perspective. In the next section, a version of the MSSM is introduced that drastically reduces the number of new parameters of the MSSM by imposing such phenomenological constraints.

3.3 The phenomenological Minimal Supersymmetric Standard Model

The phenomenological MSSM (pMSSM) is a 19 parameter version of the MSSM in which a number of well motivated constraints are implemented. The resulting parameter space is much smaller than the full MSSM parameter space, which makes it much easier to interpret and accessible to a simplified model approach.
These constraints of the pMSSM are [22]:

- No new sources of CP-violation;
- No flavor changing neutral currents;
- First and second generation universality;

The last requirement is motivated by observations, e.g. in the $\mathrm{K}^0 - \bar{\mathrm{K}}^0$ mixing, which puts strong constraints on the mass difference of potential first and second generation sfermions. This constraint applies as long as the sfermion masses are at the low-TeV scale.
The 19 new parameters are:

- $\tan\beta$: The ratio of the vacuum expectation values of the two Higgs doublets;
- M_A: The mass of the pseudoscalar Higgs boson;
- μ: The higgsino mass parameter;
- M_1, M_2, M_3: The mass parameters of the bino, wino and gluino;
- $m_{\tilde{q}}, m_{\tilde{u}_R}, m_{\tilde{d}_R}, m_{\tilde{l}}, m_{\tilde{e}_R}$: First/second generation sfermion masses;
- $m_{\tilde{Q}}, m_{\tilde{t}_R}, m_{\tilde{b}_R}, m_{\tilde{L}}, m_{\tilde{\tau}_R}$: Third generation sfermion masses;
- A_t, A_b, A_τ: Third generation trilinear couplings.

The work done is this thesis is primarily within the context of the pMSSM.

3.4 Simplified Models

New physics can appear in many different models with many different kinds of signatures, the exact ones that it will appear in are impossible to predict however. Most of these models beyond the Standard Model (BSM) also contain a large number of new parameters, providing a huge variety of possible new signatures. This makes their analysis and presentation extremely challenging.
In order to handle new parameter spaces in a consistent way and to present analysis results in a model independent way, simplified models were introduced. These simplified models are effective lagrangian descriptions of possible new physics, in which only a few new parameters and particles exist (see Figure 8).
It is possible to interpret simplified models in the context of more complete models like the pMSSM. In that context, simplified models represent extremely fine-tuned versions of the complete theory, with all processes not described by the simplified model "frozen out" by setting the masses of non-contributing particles to very high values. Additionally, the branching fractions are set to zero for unwanted decays. The simplified model approach becomes problematic if the number of particles it contains is high, e.g. like in supersymmetric cascade decays. In that case, the simplified model loses its simplicity and, with that, most of its purpose.
It should be noted that these extremely fine-tuned models are not expected to be realized in nature. Simplified models can nevertheless be used to constrain a wide variety of new physics. Some key advantages of simplified models are listed below.

Possibility of Covering Large Parameter Spaces
In many simplifying search strategies and theories like the cMSSM or mSUGRA that are embedded in bigger theories, strict relations between the new parameters are imposed. This severely limits the phenomenology covered by these models, as especially the exchange of the mass order of new BSM particles can lead to drastically different signatures. The simplified model approach avoids this problem, as the restrictions that are in place here are only on the topologies that occur, not on which topologies are possible.

Generalization to Realistic Models
Simplified model results can usually be generalized to full, realistic models [23]. This works best when the particles that are introduced when going from the simplified to the full model do not dramatically change the kinematics of the relevant signal regions. Limits on simplified models represent upper limits on the same final states that occur in full models, as the cross section times branching fraction into a given final state is typically assumed to be maximal in the case of simplified models.

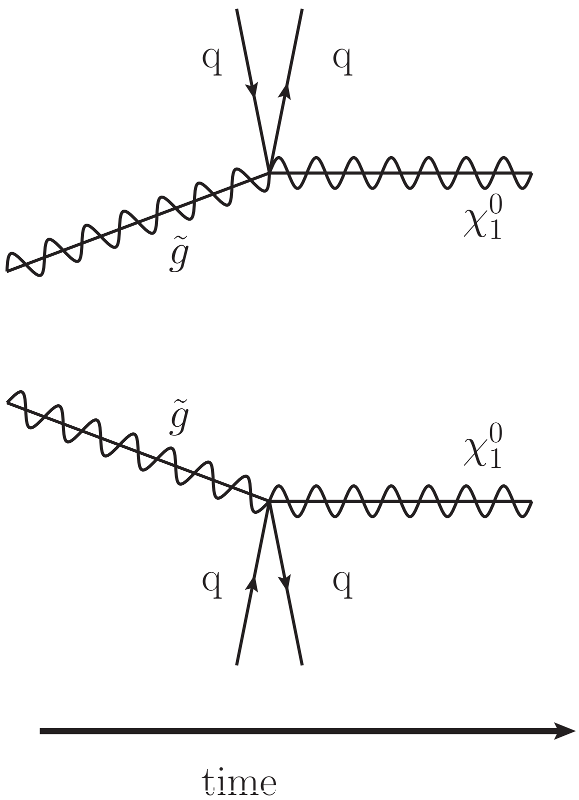

Figure 8: Example of a simplified model. Only two new particles are introduced, a neutralino $\widetilde{\chi}_1^0$ and a gluino $\widetilde{g}$. The branching fraction into the final state is set to one. Feynman diagram produced with `Jaxodraw`[8].

4 The Experimental Setup

Particle accelerators are one of the most powerful tools of physics today. Much of our knowledge of fundamental particle physics was experimentally verified at particle accelerators. Their most important recent success is the discovery of the Higgs boson in 2012 at the Large Hadron Collider (LHC) at the Conseil européen pour la recherche nucléaire (CERN) facility near Geneva. The LHC will be discussed next in Section 4.1. This work uses Monte Carlo (MC) simulations of one of the experiments situated at the LHC, the Compact Muon Solenoid (CMS), which is presented in Section 4.2.

4.1 The Large Hadron Collider

The LHC [24] is currently the most powerful particle accelerator available. It is built in the tunnels of the older LEP collider, 40-170 meters underground, with a circumference of 26.7 km. In its current normal operation mode, protons are accelerated to energies of 6.5 TeV and collided at interaction points along the accelerator ring. In an alternative operation mode, heavy ions are collided. The LHC uses the preexisting accelerators at CERN to accelerate the protons before they are injected into the main ring. The CERN accelerator complex is shown in Figure 9. Starting with the Linac2 linear accelerator, the protons are brought to higher energies in successive steps using the proton synchrotron booster (PSB), the proton synchrotron (PS) and the super proton synchrotron (SPS). The protons are then injected into the LHC at an energy of 450 GeV. The design luminosity of the LHC is $10^{34}\,\mathrm{cm}^{-2}\,\mathrm{s}^{-1}$, colliding bunches of on average $1.1 \cdot 10^{11}$ protons every 25 ns.
There are currently 7 experiments at the LHC. The main ones are ATLAS [25], CMS [26], LHCb [27], and ALICE [28]. The three smaller experiments are TOTEM [29], LHCf [30], and MoEDAL [31]. The ATLAS and CMS experiments are multi-purpose detectors designed to be sensitive to a wide range of signatures. LHCb is designed to investigate b-hadron decays and, with that, CP-violation. ALICE uses the heavy-ion collisions at the LHC to investigate the resulting quark-gluon plasma. TOTEM aims to measure total cross sections, elastic scattering and diffractive processes in proton-proton collisions. LHCf is set up to detect neutral pions to take data for the calibration of hadron interaction models used in the study of ultra-high-energy cosmic rays [30]. The aim of the MoEDAL detector is primarily the search for a magnetic monopole.

4.2 The CMS Experiment

This section concerns the CMS experiment. Monte Carlo simulations (see Section 4.4) of particles and the detector response were used in this thesis.
The CMS detector is built as a multi-purpose detector, designed to detect a very wide range of physics signatures, and reconstructs the proton-proton collisions at the LHC as completely as possible. The different subsystems that enable this are introduced below. A schematic view

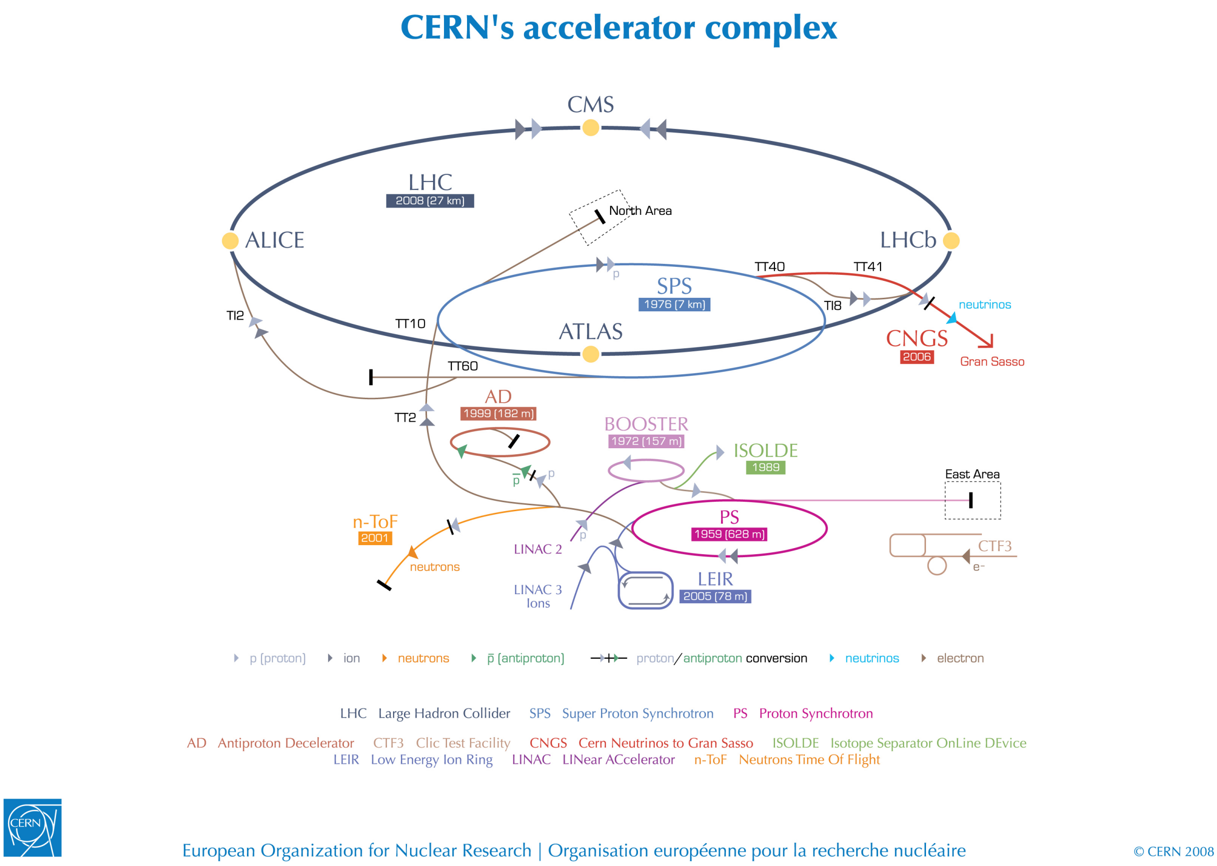

Figure 9: The CERN accelerator complex. Shown is the LHC with its main experiments and its pre-accelerator complex [32].

of the CMS detector that displays its different subsystems is given in Figure 10. Closest to the interaction point is the tracking system, followed by the electromagnetic calorimeter and the hadronic calorimeter. These three subsystems are located inside a solenoid magnet, which creates a homogeneous magnetic field of 3.8 T on the inside of the solenoid. A dedicated muon detection system is located on the outside of the magnet, inside the return yoke of the magnet [26].

The Coordinate System

The coordinate system of CMS [26] is centered at the nominal collision point. The y axis points toward the surface, the x axis points radially inward toward the center of the LHC. The z axis points along the beam direction. A cylindrical coordinate system is used, where the azimuthal angle Φ is measured from the x axis in the x-y plane, and r is the radial coordinate in that plane. The polar angle θ is measured from the z axis. As angles are not invariant under Lorentz transformations, the pseudorapidity η is used. It is defined as

$$\eta = -\ln\tan\left(\frac{\Phi}{2}\right) \tag{20}$$

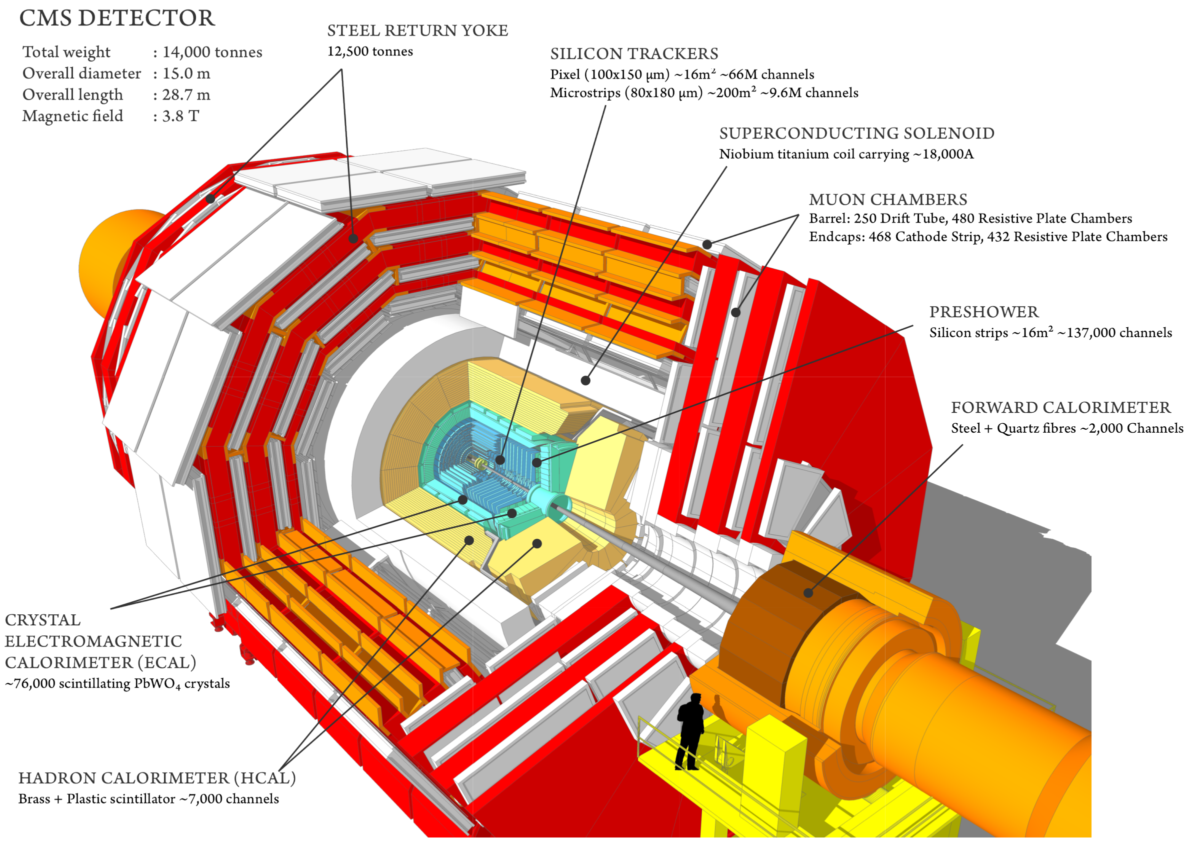

Figure 10: Schematic of the CMS detector [33].

and has the property that differences $\Delta\eta = \eta_1 - \eta_2$ are invariant under Lorentz transformations along the beam direction. Distances in the $\eta - \Phi$ plane use the measure

$$\Delta R = \sqrt{\Delta\Phi^2 - \Delta\eta^2} \quad . \tag{21}$$

The Magnet

The magnet that CMS uses is a superconducting magnet with a length of 12.5 m and a diameter of 6.3 m. It is capable of generating a homogeneous magnetic field of 3.8 T inside the coil. This magnetic field is used to bend the trajectories of electrically charged particles in the x-y plane in order to measure their momenta. An iron yoke is used to return the magnetic flux [26].

The Tracking System

The tracking system is the subsystem that is closest to the interaction point. It consists of a pixel detector and a silicon-strip detector. A schematic of the tracking system containing the layout and η coverage can be found in Figure 11. The purpose of the tracking system is to reconstruct the trajectories, or tracks, of electrically charged particles in the detector. From these trajectories, important physical quantities like the momentum are calculated. For a precise momentum determination, the track of the particle must be reconstructed as precisely as possible. The strip detector consists of 10 layers in the barrel region, and 9 layers in the forward regions [26].

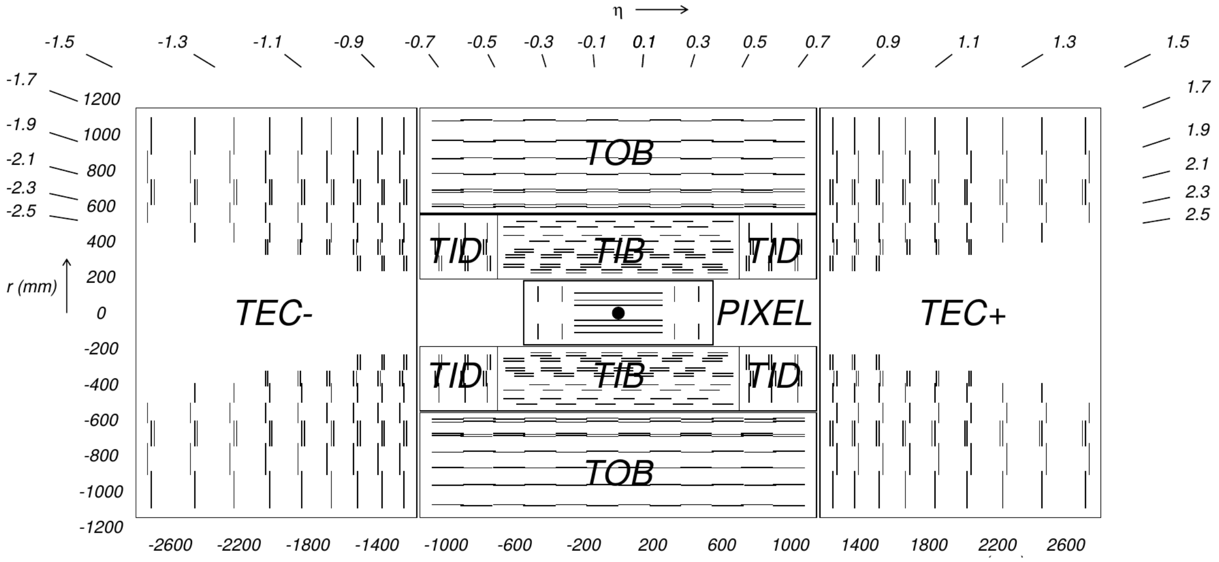

Figure 11: Schematic of the CMS tracking system. Figure taken from [26].

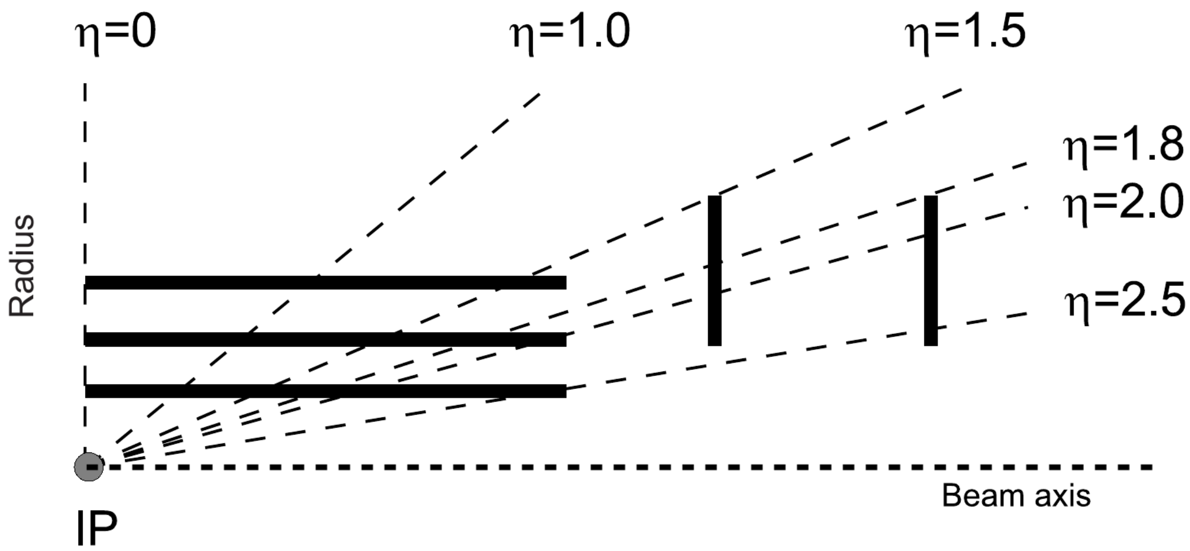

Figure 12: Schematic view of the CMS phase-0 pixel detector [26].

The Pixel Detector

The pixel detector is part of the tracking system. Its purpose is to precisely pinpoint the origin of particle trajectories to identify interaction vertices and secondary vertices. The pixel detector described here is the phase-0 pixel detector [26], which was used by CMS until an upgraded pixel detector was installed for phase-1 in 2017. As the simulations used in this thesis are for data taken in 2015 and 2016, the phase-0 detector is described instead of the phase-1 detector. The barrel contains three layers, the closest of which has a radial distance of $r = 44\,\mathrm{mm}$ from the center of the beam pipe. Two endcaps contain two discs each and extend the range to a pseudorapidity of $|\eta| < 2.5$. The pixel detector contains 48 million pixels in the barrel and a further 18 million in the endcaps. The pixel modules have the dimensions $100 \times 150\,\mu\mathrm{m}^2$. A schematic view of the pixel detector is shown in Figure 12.

The Electromagnetic Calorimeter

The electromagnetic calorimeter (ECAL) is used to measure the energy of photons and electrons. Photons and electrons that enter the ECAL undergo a series of bremsstrahlung and pair-production processes, called an electromagnetic shower, depositing their energy. The characteristic length scale of the shower is called the radiation length for electrons, and mean free path for photons. Both lengths are denoted by X_0. A calorimeter that aims to measure the complete energy of a shower must necessarily have a length of multiple X_0.

The CMS ECAL is located at a distance of $r = 1.3\,\mathrm{m}$ and extends to $r = 1.77\,\mathrm{m}$. It is split into a barrel region ($|\eta| < 1.479$) and endcaps ($1.479 < |\eta| < 3.0$). It is a homogeneous calorimeter using lead-tungstate crystals ($PbWO_4$) with a radiation length of $X_0 = 0.89\,\mathrm{cm}$ as scintillating material. The light is converted to an electric signal using avalanche photodiodes in the barrel and vacuum photodiodes in the endcaps. The barrel contains 61,200 crystals, each with a length of $25.8\,X_0$. The endcaps each contain 7,324 crystals with a length of $24.7\,X_0$. The relative energy resolution is approximately

$$\left(\frac{\sigma}{E\,[\mathrm{GeV}]}\right)^2 \approx \left(\frac{2.8\%}{\sqrt{E}\,[\sqrt{\mathrm{GeV}}]}\right)^2 + \left(\frac{0.12}{E\,[\mathrm{GeV}]}\right)^2 + (0.3\%)^2 \quad , \tag{22}$$

where the first term is stochastic, the second due to noise and the third due to calibration and systematic effects. These parameters have been established with a test beam measurement.

An additional sampling calorimeter is placed in front of the ECAL in the region $1.653 < |\eta| < 2.6$ as a preshower detector. It is used to detect the decay of neutral mesons to two photons. It uses lead as a shower initiator and silicon as active material [26].

The Hadron Calorimeter

Hadrons have a much larger characteristic interaction length scale than electrons and photons and thus deposit only a fraction of their energy in the ECAL. The hadron equivalent of the radiation length X_0 is the interaction length X_1.

In CMS, a dedicated hadron calorimeter (HCAL) is placed between the ECAL and the magnet at radii $1.77\,\mathrm{m} < r < 2.95\,\mathrm{m}$ extending to $|\eta| < 3$. It is realized as a sampling calorimeter, using alternating layers of brass and plastic-scintillators as absorber and active material, respectively. It is split into a barrel ($|\eta| < 1.4$) and endcaps ($1.3 < |\eta| < 3.0$). The barrel is made up of 36 identical wedges, each covering an area of $(\Delta\eta, \Delta\Phi) = (0.087, 0.087)$ with a total of $5.82\,X_1$ at $\theta = 90^\circ$ incidence and $10.6\,X_1$ at $|\eta| = 1.3$.

An additional hadron calorimeter is placed in the barrel region outside the magnet, using its additional stopping power to increase the total interaction length of the calorimeter by $\frac{1.3\,X_1}{\sin\theta}$. The granularity up to $|\eta| = 1.6$ remains the same as for the barrel, decreasing to

$(\Delta\eta, \Delta\Phi) = (0.17, 0.17)$ for $|\eta| > 1.6$. This outer HCAL uses quartz fibers embedded in steel absorbers to detect the Cherenkov light emitted by electromagnetically interacting particles and is thus mostly sensitive to the electromagnetic component of hadron showers [26].

The Muon System

Muons are minimally ionizing particles that pass the whole detector. A muon detector is situated inside the iron return yoke, consisting of drift tube chambers in the barrel ($|\eta| < 1.2$), cathode strip chambers in the endcaps ($0.9 < |\eta| < 2.4$) and resistive plate chambers in both barrel and endcaps. The resistive plate chambers are mainly used for triggering [26].

Trigger System

The LHC collision rate of approximately 40 MHz is too high to read out every event, as the corresponding data volume is too large. Additionally, most events are not needed for physics research. To address this, CMS uses a trigger system to select interesting events to read out. The trigger system consists of fast, hardware based elements called the level-1 trigger (L1) and software based high-level trigger (HLT). The L1 trigger reduces the event rate of 40 MHz to approximately 30 KHz, the HLT further reduces the rate to approximately 100 Hz, which is a manageable storage rate [26].

Track Reconstruction

Tracks are reconstructed from hits in the tracker and pixel detector. The reconstruction algorithm works in an iterative manner, starting with the tightest quality criteria, which are then loosened in each subsequent iteration. The track reconstruction is seeded with triplets of hits in either the pixel detector or the inner layers of the tracker. Along the trajectory given by the seed, additional hits are associated to the track candidate and the trajectory of the track candidate is fitted, at which point the candidate becomes a track. During this, the track candidate is also subject to various quality criteria. Once all tracks in an iteration are found, the criteria are loosened, the hits of high purity tracks removed, and the next iteration begins [34].

Particle Flow Algorithm

The particle flow algorithm attempts to reconstruct an event as completely as possible, reconstructing both the charged and neutral particles in an event. For this, it uses information from all subsystems of the CMS detector. Starting from the subsystem with the highest energy resolution, candidates are linked to their signature in the other subsystems of the CMS detector. In this way, their type, momentum and energy is determined [35].
Electrons are identified by a track with an associated deposit in the ECAL.
Muons are identified by a track in the muon system that is associated to a track in the tracking system.
Photons are found as ECAL deposits that cannot be associated to any track, as well as ECAL

deposits that have an excess in the deposited energy that does not come from associated electrons.
Quarks and gluons are reconstructed as jets, as discussed next.

Jet Reconstruction
The particles resulting from the hadronization of primary quarks and gluons are reconstructed as jets. The challenge lies in associating the correct particles to a jet and reject particles that did not come from the primary quark or gluon. The jet reconstruction algorithm used in this thesis is the anti-k_t clustering algorithm [36]. It is used with a distance parameter $D = 0.4$, which corresponds to the size of the jet, on particle flow objects. All particle flow objects are initially designated as jet candidates and sequentially merged. The pair of jet candidates i and j to be merged is that with a minimal value in the distance measure $d_{i,j}$, defined as

$$d_{i,j} = \min\left\{k_{\mathrm{T}i}^{-2}, k_{\mathrm{T}j}^{-2}\right\} \cdot \frac{\Delta_{ij}^2}{D^2} \quad , \tag{23}$$

where k_T is the transverse momentum, Δ_{ij} the euclidean distance with respect to y and Φ, and D the above mentioned distance parameter. The merge procedure is terminated once $d_{i,j}$ is larger for all pairs i and j than the cutoff value $d_{iB} \equiv k_{\mathrm{T}i}^{-2}$, the distance between the jet candidate i and the beam axis. To reduce the influence of pileup, charged hadrons that do not originate in the primary vertex are rejected. Several other criteria have to be fulfilled before a jet candidate is considered a jet. These are:

- The transverse momentum $\mathrm{p_T}$ (see Section 4.3) must exceed some lower threshold. In this thesis, $\mathrm{p_T} > 30\,\mathrm{GeV}$;
- $|\eta| < 3$;
- The jet has to have at least two constituents;
- The energy fraction of both neutral hadrons and neutral electromagnetic objects must not exceed 99%;
- The charged electromagnetic energy fraction cannot exceed 99%;
- The multiplicity of charged constituents must exceed zero;
- At least one charged hadron constituent.

The jet energies are calibrated, accounting for pileup, the modeling of jets, and nonlinearity of the detector response in $\mathrm{p_T}$ and η [37, 38].

b-tagged Jets
Jets whose primary particle is a b quark can be identified by the displacement of the jet origin from the primary vertex, resulting from the long lifetime of B hadrons. The point of origin of these jets is called a secondary vertex. In this thesis, the combined secondary vertex algorithm CSV2 [39] is used to identify b jets, with a working point of CSV = 0.8484.

4.3 Definitions of Observables

Transverse Momentum
Due to the nature of hadronic interactions, the momenta of the interacting particles are in general not equal at hadron colliders. This leads to an unknown total longitudinal momentum of the final state of an interaction. The transverse momentum of the primary interacting particles is negligible however, which implies that the sum of all transverse momenta of the final state particles of an interaction is always zero. An important physical quantity at hadron collider is therefore the transverse momentum $\mathrm{p_T}$, defined as

$$\mathrm{p_T} = \sqrt{\mathrm{p}_x^2 + \mathrm{p}_y^2}\,. \tag{24}$$

Missing Transverse Energy
Missing transverse energy, or more precisely missing transverse momentum, is defined as

$$\not{E}_\mathrm{T} = -\sum_{\mathrm{pfc}} \mathrm{p_T} \cdot \hat{e}_\mathrm{T} \quad , \tag{25}$$

the negative sum of the $\mathrm{p_T}$ times the directional unit vector of all particle flow candidates in an event. Invisible particles such as neutrinos do not interact with the detector and leave no visible signature. They do upset the $\mathrm{p_T}$ balance of the event however, leading to a high $\not{E}_\mathrm{T}$ signature. Dark matter searches usually produce a $\not{E}_\mathrm{T}$ signature, as, like neutrinos, the stable dark matter is expected not to interact with the detector. Another large contribution to the $\not{E}_\mathrm{T}$ of an event results from mis-measured jet momenta, even in events that are balanced in $\mathrm{p_T}$.

4.4 Data Samples

This thesis uses official CMS Monte Carlo samples for a sensitivity study. They were created using `MadGraph` [40] and `Pythia` [41]. The most relevant samples are the following:

$\mathbf{Z+Jets \rightarrow \nu\nu + Jets}$
`/ZJetsToNuNu_HT-[X]_13TeV-madgraph/RunIISummer16DR80Premix-PUMoriond17_80X`
`_mcRun2_asymptotic_2016_TrancheIV_v6-v1/AODSIM`
[X] are the following $\mathrm{H_T}$ ranges: [`100To200, 200To400,400To600,600To800,800To1200`].

$\mathbf{W + Jets \rightarrow l\nu + Jets}$

/WJetsToLNu_HT-[X]_TuneCUETP8M1_13TeV-madgraphMLM-pythia8/RunIISummer16DR80Premix-PUMoriond17_80X_mcRun2_asymptotic_2016_TrancheIV_v6-v1/AODSIM

[X] are the following H_T ranges: [200To400,400To600,600To800,800To1200].

The signal samples were created using Pythia8[41] at next-to-leading order precision. The production cross sections are taken from [42, 43, 44] at next-to-next-to-leading order precision and then interpolated to the relevant masses. The produced signal samples correspond to an integrated luminosity of 267 fb.

5 SmodelS

Part of the aim of the thesis is to identify BSM signatures within the pMSSM that have not been considered yet. For this purpose, the tool `SmodelS` is used. First, a general introduction into `SmodelS` is given in Section 5.1. The most important assumptions that `SmodelS` makes are discussed in Section 5.2. Important terms of the nomenclature within `SmodelS` are introduced in Section 5.3. Next, the simplified model decomposition that is the core of `SmodelS` is described in Section 5.4. The categorization of simplified models by `SmodelS` is described in Section 5.5. Section 5.6 concerns the output formats that `SmodelS` uses for its results. A list of all CMS and ATLAS analyses used by `SmodelS`is given in Section 5.7. Finally, Section 5.8 describes the modifications done to `SmodelS` in the context of this thesis.

5.1 Introduction

`SmodelS` [45, 46, 47] is a tool that allows to test input models against LHC results from CMS and ATLAS. The idea is to cover a realistic model, for example a point in the pMSSM parameter space, with a spectrum of simplified models. To that end, `SmodelS` decomposes the model into its **s**implified **m**odel **s**pectrum (SMS). For each simplified model in the SMS, a weight is computed that includes production cross sections and branching ratios. This weight is tested against a large database of CMS and ATLAS results (see section 5.7). These results come in the form of upper limit (UL) maps and efficiency maps, presented in simplified models. The main requirement on the input models is that they exhibit a $\mathbb{Z}_2$ symmetry (like R-parity in SUSY) and produce an $\not{E}_T$ signature in the detector. Unlike tools with a similar purpose, such as `CheckMATE` [48, 49], `SmodelS` does not rely on Monte Carlo simulations for the input model. This makes it very fast compared to Monte Carlo based tools and ideally suited for use in concert with large BSM parameter scans. An overview of how `SmodelS` works is given in Figure 13. A model is given as input in the `SLHA` [50] file format or a more general `LHE` [51] file, together with the cross section of all pairs of BSM particles above a given cross section threshold. The model is then decomposed into its SMS and for each simplified model in the SMS, the weight is computed. The simplified models in the SMS are then combined into more general topologies, corresponding to the constraints of the CMS and ATLAS results in the `SmodelS` database and tested against the upper limit maps or efficiency maps provided therein. If any of the weights of the simplified models in the SMS exceeds the upper limit of any CMS or ATLAS result in the `SmodelS` database, the whole input model is excluded. However, no statistical combination of constraints from different CMS or ATLAS analyses is done. Note that for computation time purposes, a lower threshold on the weight is present, which means that not all processes that are in principle possible in the input model are present in the SMS of the input model. This leads to the fact that the SMS of two different versions of the same theory framework, e.g. two points in the pMSSM parameter space, in general do not contain the same simplified models.
A more detailed description of the decomposition process can be found in Section 5.4.

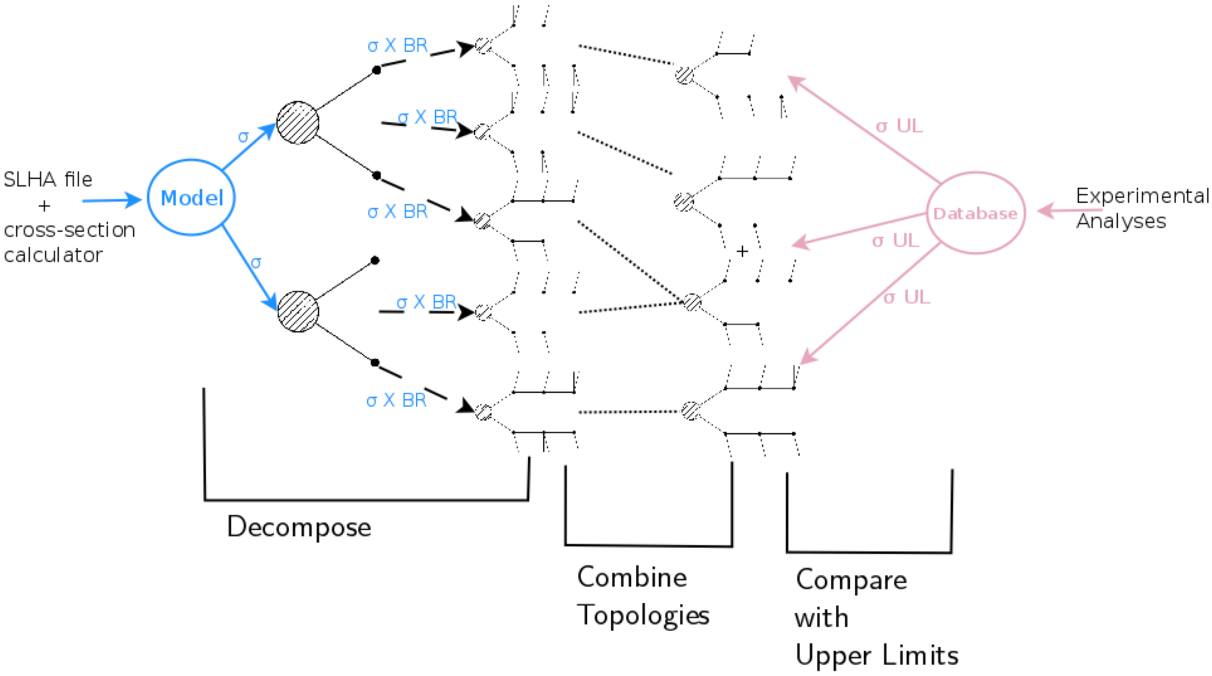

Figure 13: The `SmodelS` process from left to right: A model is given as input to `SmodelS`, including the production cross sections of all pairs of particles that occur. The model is decomposed into its SMS, and each element of the SMS is given a weight $\sigma \cdot \sum \mathrm{BR}$. Elements of the SMS are combined into topologies such that they match the constraints of the analyses published by CMS or ATLAS. The SMS is tested against the constraints in the `SmodelS` database (see Section 5.7) [46].

5.2 Assumptions

`SmodelS` relies on several assumptions to be valid in order to be safe in its predictions:

- Signal efficiencies depend sufficiently exclusively on the event kinematics and do not depend highly on details of a given model. Specifics of a model such as the particle spin or the production mode are assumed to only effect the signature marginally [46]. This is not always valid. Cases where this assumption is not valid include searches that rely heavily on the shape of kinematic distributions [46];

- From the assumption above it follows that the properties of a simplified model and its behavior in a given signal region can be reduced to its mass spectrum, production cross section and branching fractions [46];

- Simplified models in the spectrum are independent of each other and do not interfere.

An important example of where these assumptions do not hold are monojet dark matter searches (Mono-X searches). In these cases, the production mode is expected to play an important role in the event kinematics and as such, the first assumption listed above does not hold.

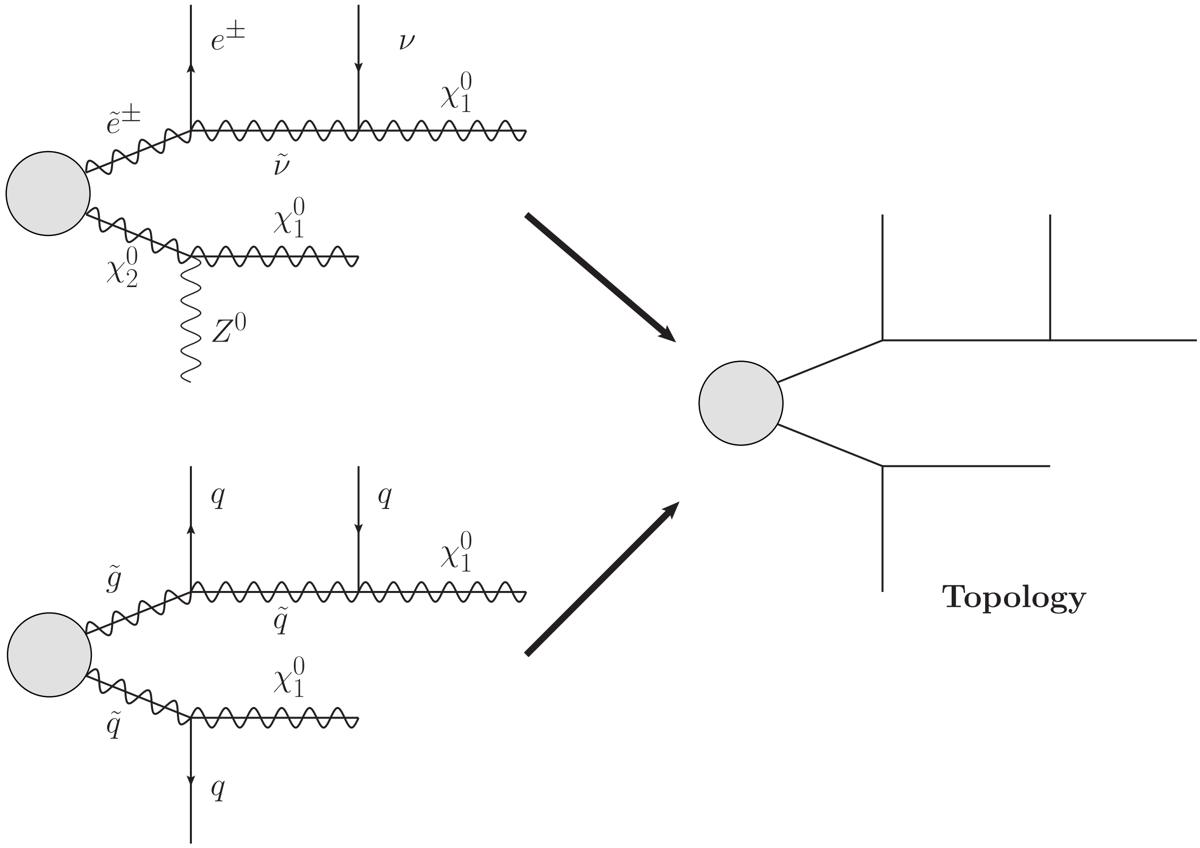

Figure 14: Topologies and simplified models: Complete Feynman diagrams of two simplified models (left), containing the full information of all particles involved. The topology (right) contains only the general structure of particle lines and vertices. Different simplified models can share the same topology. Feynman diagrams produced with `Jaxodraw`[8].

5.3 SmodelS Nomenclature

`SmodelS` uses a variety of terms to describe simplified models. A brief explanation of terms relevant to this thesis is given here.

Branch
Since `SmodelS` requires a $\mathbb{Z}$ symmetry in the input model, all simplified models produce pairs of BSM particles, called branch mothers. The two branches contain the decay chain of the respective branch mother.

Topology
Simplified models can be fully described by all occurring particles, their masses, and the Feynman diagram that provides the information of the specific decay chain. In `SmodelS` language, the topology of a simplified model is its branch structure and Standard Model final state. Compared to the simplified model, it no longer contains any information about the specific BSM particles appearing in the diagram, or their masses. It is introduced as a way to group similar simplified models in order to better test them against experimental constraints in the database. Figure 14 illustrates the difference between a simplified model and its corresponding topology.

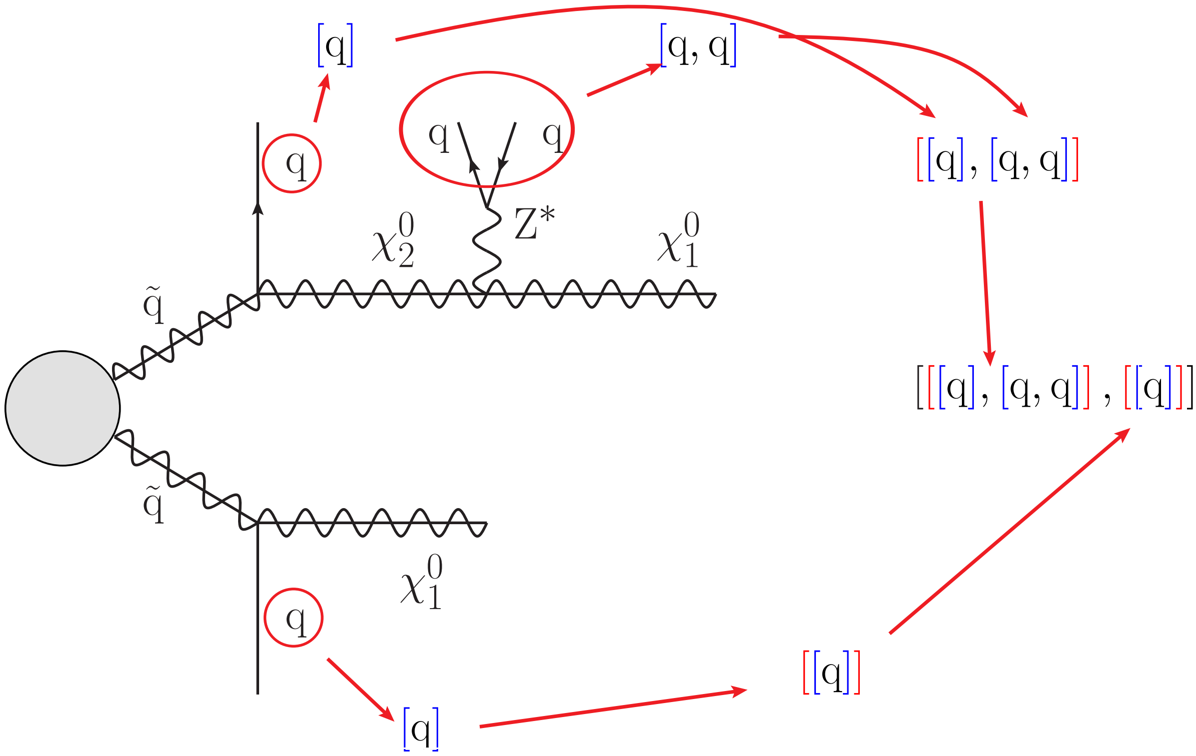

Figure 15: Translation of an example simplified model into its corresponding bracket. The innermost set of brackets consists of vertices (blue brackets), where the Standard Model particles appearing at a vertex are separated by a comma. All the vertices in a branch are collected, separated by commas, and encapsulated by another set of brackets (red brackets). The branched are again collected, separated by a comma, and enclosed in the outer set of brackets (black bracket). Figure produced with `Jaxodraw`[8].

Bracket Notation

`SmodelS` uses a notation of nested brackets to represent a simplified model or more general topologies, called bracket notation [45] (compare Figure 15). The outermost set of brackets goes around the entire model descriptor. The two branches, encapsulated by the next set of brackets, are separated by a comma. In the branch brackets, each vertex in given inside its own set of brackets, and separated by commas. The particles inside each vertex are separated by commas, as well. The resulting template is:

- model = [[first branch],[second branch]] ,
- branch = [[first vertex],[second vertex],...] ,
- vertex = [1st particle, 2nd particle, ...].

The TxName

`SmodelS` assigns so-called TxNames [45] to simplified models. They were invented by the CMS collaboration in the context of simplified model searches [52]. They serve as a shorthand for the constraints in the `SmodelS` database. TxNames are built according to the template T+"prefix"+"appendix". The prefix contains information about the branch mothers (e.g.: TChipChim describes the production of a $\tilde{\chi}^+\tilde{\chi}^-$-pair). The prefix also depends on whether the

Production mode	Prefix old convention 1 vertex per branch	Prefix old convention >1 vertex per branch
$[\widetilde{g},\widetilde{g}]$	1	5
$[\widetilde{q},\widetilde{q}]$	2	6
$[\widetilde{g},\widetilde{q}]$	GQ	GQ
$[\chi^0,\chi^0]$	Chi	ChiChi
$[\chi^0,\chi^\pm]$	Chi	ChiChipm
$[\chi^\pm,\chi^\mp]$	Chi	ChipChim
$[\widetilde{l},\widetilde{l}]$	SlepSlep	SlepSlep

Table 2: Table of TxName prefixes in the TxName convention.

simplified model contains only one vertex per branch or multiple vertices per branch. There is no consistent way to recognize prefixes for models with just one vertex per branch however. They have to be known beforehand. As examples, the simplified model T2tt, with the prefix "2", describes pair production of squarks (stops, in this case) that each decay via a top quark to the LSP. There is no simplified model T2ttqq, however, as this would require more than one vertex per branch. Instead, simplified models with a pair of squarks as their branch mothers that contain more than one vertex per branch are given the prefix "5". The correct TxName is therefore not T2ttqq, but T5ttqq. A table covering all production modes and their handle prefixes can be found in Table 2.

The appendix can either be the Standard Model final state or some information of the sparticles involved that can be used to identify the model. As an example for the latter case, the TxName TChiChipmSlepStau corresponds to the process in Figure 16, which is written [[[L],[L]],[[nu],[ta]]] in bracket notation. It corresponds to the production of a $\widetilde{\chi}_2^0$-$\widetilde{\chi}_1^\pm$ pair, with the $\widetilde{\chi}_2^0$ decaying via an intermediate slepton to the LSP, and the $\widetilde{\chi}_1^\pm$ decaying via an intermediate stau to the LSP.

Should no appendix appear at the end of a TxName, then a default one is assumed (usually light quarks). An example is the T2 simplified model, which contains no appendix and describes pair production of squarks that decay to a light quark and the $\widetilde{\chi}_1^0$. It should be noted that simplified models that differ only by the exchange of branch ordering are considered the same simplified model and get the same name.

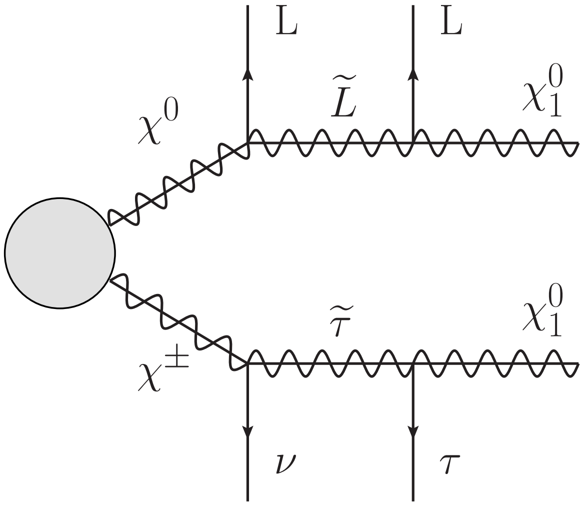

Figure 16: Example of a simplified model where the TxName TChiChipmSlepStau is defined by the intermediate sparticles in the simplified models and not the Standard Model final state. Feynman diagrams produced with `Jaxodraw`[8].

5.4 Simplified Model Decomposition

`SmodelS` has two types of decomposition modes, a Monte Carlo based method and a `SLHA` based method.
In the Monte Carlo based method, a `LHE` file, containing parton level events, is given as input. Each event can then be directly translated into a simplified model. This method is subject to the statistics of the Monte Carlo simulations used in the creation of the `LHE` file. This uncertainty directly contributes to the uncertainty of the weight of the simplified model.

For the `SLHA` based method, the input file is in the `SLHA` format and contains all the parameters and particles of the model, as well as all possible decays of each particle and their respective branching fraction. In addition to this, the cross sections for the primary particles have to be provided. These are not technically part of the `SLHA` format and have to be provided by the user. `SmodelS` provides a tool to calculate leading order cross sections using `Pythia6` or `Pythia8` [53, 53, 41]. The tool also has an option to generate next-to- leading order cross sections for squarks and gluinos, and soft gluon resummation with next-to-leading logarithm precision, using `NLL-fast` [54, 55, 56, 57, 58, 59, 60].
In the context of this thesis, only the `SLHA` based approach was used. Using this method, `SmodelS` decomposes an input model into its simplified model spectrum in an iterative manner in the following way:

For each pair of primary particles that the user provided cross sections for, a branch is initiated. Processes for which no cross section is provided are not considered. Using the decay tables in the input `SLHA` file, vertices corresponding to the decays therein are added to the branches one at a time. At each vertex addition, the weight of the current diagram is computed as

$$\text{weight} = \sigma \cdot \prod_{\text{Vertices}} \text{BF}_{\text{Vertex}} \ , \tag{26}$$

where σ is the production cross section for the pair of branch mothers, and the product consists of the branching fractions BF at all vertices appearing in the current diagram.
The decomposition process for any simplified model under construction terminates if one of two criteria apply:

- If during the construction of a simplified model the weight passes a lower threshold, the simplified model is rejected. All simplified models derived from this rejected model, i.e. simplified models containing the rejected simplified model as a submodel, are also rejected, since adding more vertices always decreases the weight. By default the weight threshold is set at 0.03 fb, corresponding to approximately one particle produced at a luminosity of $36\,\text{fb}^{-1}$. The threshold can be changed freely, according to the requirements of the user.

- If both branches end in the LSP without crossing the lower threshold on the weight, the model is considered valid and added to the spectrum. If there is a decay path that does not end in the LSP, the model violates the `SmodelS` assumptions and can not be decomposed properly.

At the end of the decomposition, all processes occurring in the input model that pass the cross section threshold and end in the LSP are part of the spectrum. Processes that have a weight below the threshold are not part of the spectrum, which results in the fact that the SMS of any two input models are not isomorphic. An schematic example of the decomposition process is depicted in Figure 17.

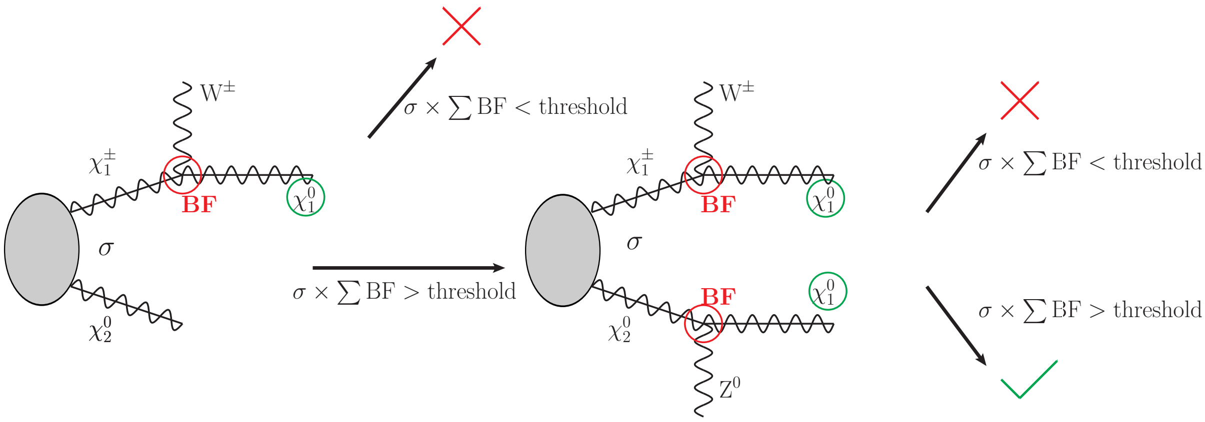

Figure 17: An example of the decomposition process. The primary particles produced are taken from the `SLHA` file of the input model. The production cross section σ is given as input by the user. If the user does not have the cross sections at hand, `SmodelS` provides a tool to compute the leading order cross section using `Pythia` (and `NLL-fast`, where possible). The vertices and their branching fractions BF are taken from the decay table of the `SLHA` file of the input model. The decomposition is aborted if the weight $\sigma \times \prod \mathrm{BF}$ is below the threshold value specified in the `SmodelS` parameters.ini file. If both branches end in the LSP, in this case the χ_1^0, the model is added to the spectrum and the next model is considered. Figure produced with `Jaxodraw`[8].

Weight Threshold

`SmodelS` uses a lower weight threshold for the decomposition in order to not produce simplified models in which the user is not interested in due to their small cross section. Choosing a low value for the threshold can lead to a significant increase in computation time.

It should be noted that the weight threshold applies to the elementary simplified models, not to any grouping. For example, the simplified model TChiWWoff actually describes a group of more elementary simplified models corresponding to the decay modes of the off shell W boson. It may happen that the combined weight of the W decay modes is above the threshold, but individual processes are not. These subprocesses are then not considered for the total weight of the simplified model. In extreme cases, the entire model might not be added to the spectrum if all individual weights are below the threshold. The problem becomes more like to occur the more possible decay modes a particle has, and the more of these particles occur in a given simplified model. This fact must be considered when choosing a value for the threshold, for example by setting the weight threshold an order of magnitude or two below what the naive value would be.

Compression

There are cases where simplified models look like different simplified models once the detector is taken into account. This can occur when part of the Standard Model final state of the simplified model is not reconstructed. This happens when:

1. The Standard Model particles produced at a vertex are exclusively neutrinos;
2. The mass difference between the decaying BSM particle and the resulting BSM particle is so small that the Standard Model particles at the vertex are usually produced with too little energy to be reconstructed. The threshold when this happens depends on the exact kinematics of the model, as a boost of the decaying BSM particle can enlarge the energy of the Standard Model particles in the lab frame such that they are again reconstructed by the detector, even if the mass difference is small.

To illustrate this, consider the simplified model in Figure 18. The upper branch contains the decay $\widetilde{q} \to \widetilde{\chi}_1^0$ q with a very low value of $m_{\widetilde{\chi}_1^0, \widetilde{q}}$. Unless the $\widetilde{q}$ has a very high boost, the quark will not be reconstructed by the detector. Similarly, the neutrinos in the lower branch will never be reconstructed. Thus, `SmodelS` performs what it calls "mass compression" in the first case and "invisible compression" in the second case. The vertex and intermediate particle is removed, resulting in a different simplified model. The value of Δm at which `SmodelS` starts to perform mass compression can be chosen by the user. Note that `SmodelS` only performs invisible compression if the invisible vertex is the last vertex of a branch. This is done because invisible vertices can significantly alter the kinematics of the remaining branch. The branch can be safely compressed however, if the only particles occurring after the invisible vertex are invisible as well, since it then has no influence on the $\not{E}_T$ signature. The compression features can be enabled or disabled by the user, as well as the value of the mass compression threshold.

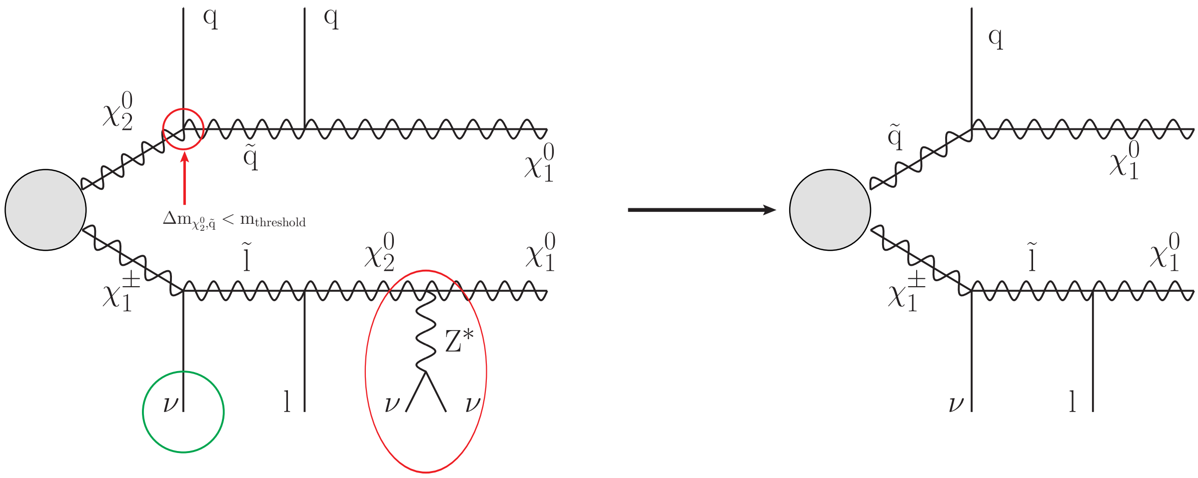

Figure 18: Illustration of the two `SmodelS` compression scenarios: Mass compression (top branch) and invisible (bottom branch) compression.
Mass compression occurs when a sparticle decays into a nearly mass degenerate sparticle, leading to a very low-energy Standard Model final state at that vertex. If the mass difference is below a threshold value set by the user, `SmodelS` removes the vertex and the lighter of the two sparticles is kept.
Invisible compressions removes all consecutive vertices, starting from the last one, that contain neutrinos. All invisible vertices that come ahead of a vertex with a visible final state are kept. Figure produced with `Jaxodraw`[8].

5.5 Categorization of Simplified Models

For each input model, `SmodelS` categorizes the simplified models in the SMS into three categories, depending on whether the simplified model is constrained by results in the `SmodelS` database. These categories are:

Constrained Topologies

These are simplified models or topologies in the SMS which are constrained by at least one result in the `SmodelS` database (see Section 5.7). The simplified models herein are used to exclude the input model, if there exists a constraint in the database that is capable of doing so.

Outside Grid Topologies

Outside Grid topologies are simplified models in the SMS of the input model for which there exists a result in the database, but that can not constrain the model because the masses in the input model are not constrained by the result in the database (see Figure 19).

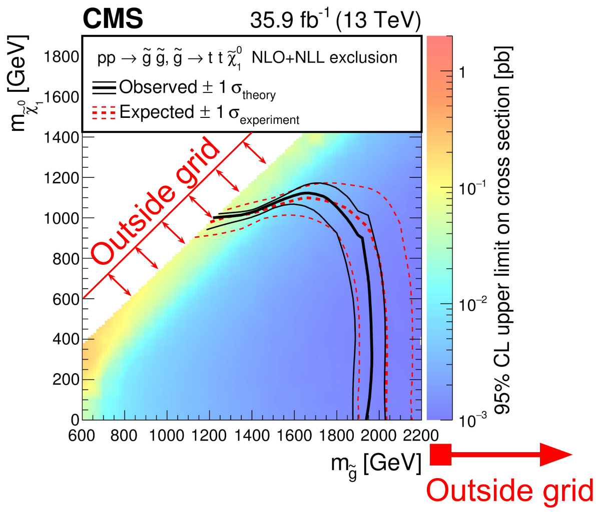

Figure 19: Illustration of outside grid topologies: If the masses of a input model are constrained by a result like the one shown here, but there are no limits on the masses of the input model, the topology is "outside grid". Figure taken from [61].

Missing Topologies

Simplified models that are part of the spectrum but are not constrained by any database entry are labeled missing topologies by `SmodelS`. They give possible avenues to still exclude the model if the database can be extended by an analysis that targets the topology in question. This can either be done by adding more existing analyses into the database or by designing a new analysis entirely. Missing topologies are, when applicable, classified as:

- Asymmetric branches: If the branches of the missing simplified model are not identical, the simplified model is categorized as "asymmetric branches".

- Long cascade: If one of the branches contains at least three vertices, the missing simplified model is categorized as "long cascade".

5.6 SmodelS Output

`SmodelS` presents its results in five different formats, which more or less contain the same information. The information included in the output is introduced in this section. This section closely follow the `SmodelS` manual [45].
The five output formats that `SmodelS` uses are:

- Std output: Printed to the screen when running `SmodelS`, also saved in a plain .log file;
- Summary output: Saved in the output directory as <input file name>.smodels;
- Python dictionary output: Saved in the output directory as <input file name>.py;
- `SLHA` output: Uses the `SLHA` block structure, saved in the input directory;
- XML output: complete information saved in a human-readable XML file in the output directory.

In the context of this thesis, only the XML output format was extensively used. The output information listed below refers to the XML output format specifically and can be slightly different in the other output formats. Detailed information on exactly what `SmodelS` information is contained in which output formats can be found in the `SmodelS` manual.
The XML output of `SmodelS` contains the following information:

- Input parameters:
  - Weight threshold;
  - Mass compression threshold;
  - `SmodelS` version;
  - Database version;
- Information on all simplified models in the SMS above the weight threshold, including:
  - The simplified model in bracket notation;
  - The weight;
  - The pdg ids of the intermediate sparticles in the interaction;
  - The masses of the intermediate sparticles;
- The theory predictions (weights) for the topologies that are constrained by a result in the `SmodelS` database, as well as information on the result that constrains the topology;

- The missing topologies. For each missing topology, the following information is presented:
  - The bracket notation of the topology;
  - The weight;
  - The list of contributing simplified models in bracket notation, as well as their indices;
- The outside-grid topologies, their weight and contributing elements;
- The long cascade topologies, their weight and the pairs of branch mothers that produced long cascades;
- The asymmetric branch topologies, their weight and the pairs of branch mothers that produced the asymmetric decays.

5.7 SmodelS Result Database

The database of CMS and ATLAS results that was used in this thesis is version 1.1.1. A full list of the analyses in the database is given in Table 3.

CMS $\sqrt{s} = 8\,\mathrm{TeV}$	ATLAS $\sqrt{s} = 8\,\mathrm{TeV}$
CMS-PAS-SUS-13-015[62]	ATLAS-CONF-2012-166[63]
CMS-PAS-SUS-13-016[64]	ATLAS-CONF-2013-007[65]
CMS-PAS-SUS-13-018[66]	ATLAS-CONF-2013-061[67]
CMS-PAS-SUS-13-023[68]	ATLAS-CONF-2013-089[69]
CMS-SUS-12-024[70]	ATLAS-SUSY-2013-02[71]
CMS-SUS-12-028[72]	ATLAS-SUSY-2013-04[73]
CMS-SUS-13-002[74]	ATLAS-SUSY-2013-05[75]
CMS-SUS-13-004[76]	ATLAS-SUSY-2013-08[77]
CMS-SUS-13-006[78]	ATLAS-SUSY-2013-09[79]
CMS-SUS-13-007[80]	ATLAS-SUSY-2013-11[81]
CMS-SUS-13-011[82]	ATLAS-SUSY-2013-12[83]
CMS-SUS-13-012[84]	ATLAS-SUSY-2013-15[63]
CMS-SUS-13-013[85]	ATLAS-SUSY-2013-16[86]
CMS-SUS-13-019[87]	ATLAS-SUSY-2013-18[88]
CMS-SUS-14-010[89]	ATLAS-SUSY-2013-19[90]
CMS-SUS-14-021[91]	ATLAS-SUSY-2013-21[92]
	ATLAS-SUSY-2013-23[93]
	ATLAS-SUSY-2014-03[94]

CMS $\sqrt{s} = 13\,\mathrm{TeV}$	ATLAS $\sqrt{s} = 13\,\mathrm{TeV}$
CMS-PAS-SUS-16-014[95]	ATLAS-SUSY-2015-01[96]
CMS-PAS-SUS-16-015[97]	ATLAS-SUSY-2015-02[98]
CMS-PAS-SUS-16-016[99]	ATLAS-SUSY-2015-06[100]
CMS-PAS-SUS-16-019[101]	ATLAS-SUSY-2015-09[102]
CMS-PAS-SUS-16-022[103]	
CMS-SUS-15-008[104]	

Table 3: A full list of the analyses contained in the `SmodelS` database 1.1.1.

5.8 SmodelS Modification

In the context of this work, `SmodelS` was slightly modified in order to enable a phenomenological study on a pMSSM parameter scan. The modifications are discussed in this section.

5.9 Modified SmodelS XML Output

In order to perform a study on the most common simplified models occurring in the remaining pMSSM parameter space, the `SmodelS` XML output was modified. The necessary information is given in two ways by `SmodelS`. One can either extract the more general missing topologies introduced by `SmodelS` or the more traditional missing simplified models. The former neglects all information of the BSM particles involved in the process. This is done because the additional information, e.g. spin, is assumed to have little influence on the kinematics of the final state and thus the exclusion power of `SmodelS` (see Section 5.2). For this thesis, it was decided to use the traditional simplified models instead of topologies, as this makes an interpretation within the pMSSM easier.
Following the modification, the XML output contains a list of all the missing simplified models in the SMS of the input model. The following information can be found in the output:

- The missing simplified model in extended bracket representation, ordered by decreasing weight;
- The TxName of the missing simplified model in the extended nomenclature;
- The weight of the missing simplified model;
- The outside grid weight of the simplified model. For each missing simplified model, multiple diagrams can contribute. For these, the following information is displayed:
  - The diagram in extended bracket notation;
  - The weight it contributes to the missing simplified model;
  - A boolean for compression;
  - A boolean for asymmetric decays;
  - A boolean for outside grid;
  - A boolean for long cascades;
  - The masses and particle IDs for both branch mothers;
  - The mass of the LSP in the model;
  - The masses and particle IDs of the sparticles for both branches, ordered by occurrence.

5.10 Extended Bracket Notation

In the original bracket notation used by `SmodelS`, the sparticles in the simplified model are not tracked. This can lead to ambiguities where two different simplified models appear as the same simplified model when looking at the bracket that represents it. Any given bracket could thus be understood as a sum over all simplified models that produce the same topology and final state. This approach follows the primary `SmodelS` assumption that the effects of the missing sparticle information on any given signal region is small, provided they have similar masses.

For the phenomenological study that was carried out in this thesis, it was decided that the diagrams and their representing bracket should correspond to the simplified models unambiguously. For this purpose, the bracket notation is extended to include the sparticles in a straightforward way. The sparticles are appended to the original bracket as a set of nested brackets that is one layer deep. The outer set of brackets encapsulates the whole sparticle content. The two branches are each encapsulated by an inner set of brackets. Inside the branches, the sparticles are listed and separated by commas (see Figure 20). This extended bracket notation now contains the complete information inherent in the Feynman diagram.

5.11 Extended TxName Convention

The original TxName convention aims to associate short identifiers, the TxName, to simplified models (see Section 5.3). However, the original convention only covers a small fraction of the enormous number of possible simplified models, so that in order to do a thorough study of simplified model spectra, this gap had to be filled. The extension created in the context of this work covers all simplified models that:

- Contain only particles that exist within the MSSM;
- Produce a pair of SUSY particles, each initiating a branch;
- End in the lightest neutralino $\widetilde{\chi}_1^0$, which is the LSP.

The TxName in the extended convention is also slightly modified with respect to the old convention. The handle prefix TChi previously described models with pair production of gauginos and only one vertex per branch, while the prefixes TChiChi, TChiChipm and TChipChim described simplified models with multiple vertices per branches and $\widetilde{\chi}_1^0\,\widetilde{\chi}_1^0$, $\widetilde{\chi}_1^0\,\widetilde{\chi}_1^{\pm}$, and $\chi^{\pm}\chi^{\mp}$ production, respectively. A similar case existed in the strong sector: The T1 and T3 prefixes describe simplified models with paired production of gluinos with one and multiple vertices per branch, respectively. Similarly, the T2 and T5 prefixes for squark production.
This dependence of the prefix on the number of branch vertices was abandoned in the extended convention, since it was deemed to leave too much inference on the side of the user. The extended convention uses the T1, T2 and TGQ in the case of strong simplified models, and the >1 vertices per branch prefix version in all other cases (see Table 4). As an example, the model

Production mode	Prefix old convention 1 vertex per branch	Prefix old convention >1 vertex per branch	Prefix extended convention
$[\tilde{g}, \tilde{g}]$	1	5	1
$[\tilde{q}, \tilde{q}]$	2	6	2
$[\tilde{g}, \tilde{q}]$	GQ	GQ	GQ
$[\chi^0, \chi^0]$	Chi	ChiChi	ChiChi
$[\chi^0, \chi^\pm]$	Chi	ChiChipm	ChiChipm
$[\chi^\pm, \chi^\mp]$	Chi	ChipChim	ChipChim
$[\tilde{l}, \tilde{l}]$	SlepSlep	SlepSlep	SlepSlep

Table 4: Table of TxName prefixes in the original TxName convention and the extended convention.

[[[t],[b]],[[t],[b]]] has the TxName T5tbtb in the original convention and the TxName T2tbtb in the extended convention. An example in the electroweak sector is given by [[[W]],[[Z]]], which maps to TChiWZ in the original convention and to TChiChipmZW in the extended convention. The order of the final state in the TxName appendix WZ is changed to conform to a reverse lexicographical ordering ZW in the extended convention. This is done to avoid mapping branch symmetric models, e.g. [[[W]],[[Z]]] and [[[Z]],[[W]]] to different TxNames. The choice of reverse lexicographic order over a lexicographic order is arbitrary and serves no other purpose.

Another change is done to the appendix of the TxName. Whereas in the original nomenclature, anything that can identify a simplified model was allowed to define in the appendix, in the extended convention the appendix is always the Standard Model final state. This also means that there are no more default final states if no appendix is specified. The extended convention has the following logic (see Figure 20):

- Assign the prefix according to Table 4 if the model existed in the original convention. If it did not exist, the prefix is generated in a regular way by writing out the branch mother identifiers one after another (see Table 5);

- Append the Standard Model final state particles in order of branch and vertex they appear in the branch. By convention, the upper branch is the first one, the lower branch the second one. Branch symmetric models are mapped to the prefix that comes last in lexicographical order.

Sparticle	Identifier
$\widetilde{q}$	Q
$\widetilde{g}$	G
$\widetilde{l}$	Slep
$\widetilde{\nu}$	Snu
$\widetilde{\tau}$	Stau
χ^0	Chi
$\chi^\pm$	Chipm

Table 5: Regular way of creating the prefix of the TxName from the branch mothers. The prefix is the concatenation of the identifiers of the branch mothers. Branch symmetric models are mapped to the prefix that comes last in lexicographical order.

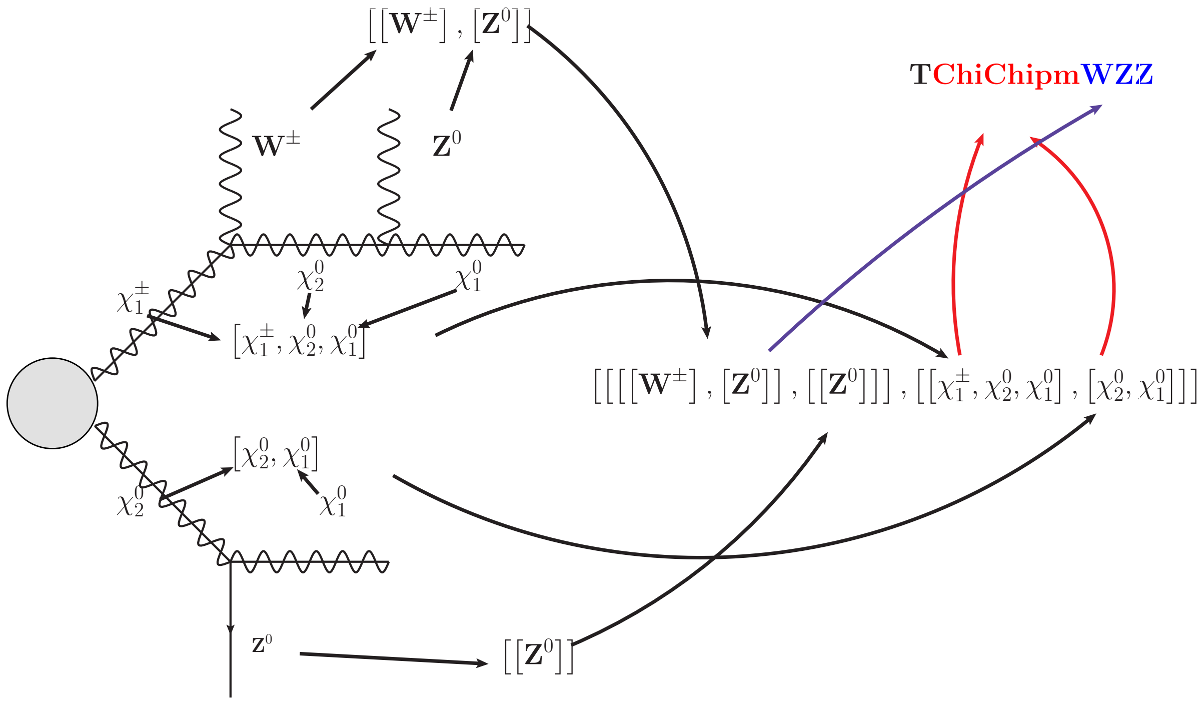

Figure 20: Translation of a Feynman diagram into its bracket notation and corresponding TxName. The prefix "ChiChipm" corresponds to the branch mothers. The final state is appended afterwards. Figure produced with `Jaxodraw`[8].

It should be noted that some grouping of diagrams is still included in the simplified models, their bracket representation, and corresponding TxName. This grouping includes:

- Simplified models that differ only by particle charges. In general, charges are not explicitly tracked;
- Antiparticles are not tracked. They are denoted by their particle counterpart;
- Light quarks (u,d,s) are not differentiated and simply denoted by "q";
- Only three types of squarks are differentiated: The $\widetilde{t}$ and $\widetilde{b}$ are tracked separately from the squarks, which include the $\widetilde{u}$, the $\widetilde{d}$, the $\widetilde{s}$ and the $\widetilde{c}$. These light squarks are denoted $\widetilde{q}$;

- Similarly, the $\widetilde{e}$ and the $\widetilde{\mu}$ are combined to the slepton, denoted as $\widetilde{l}$, while the $\widetilde{\tau}$ is tracked separately.

5.12 Inclusion of Off Shell Gauge Bosons

`SmodelS` does not identify or track off shell gauge boson decays, instead it saves each separate final state of the gauge boson as its own simplified model. This can artificially reduce the weight of an otherwise highly weighted process if some of the different final states of the gauge boson are below the weight threshold for the decomposition.

It was decided to group the different simplified models that correspond to the decay of an off shell gauge boson into one simplified model containing the off shell gauge boson instead of different simplified models describing the individual final states. In the bracket notation, off shell gauge bosons are denoted with an additional "off" after the particle identifier, e.g. $[[[\mathrm{Z}]],[[\mathrm{W}]]] \rightarrow [[[\mathrm{Zoff}]],[[\mathrm{Woff}]]]$. The TxName is modified in a likewise fashion, adding "off" after the particle identifier in the appendix. Using the same example: TChiChipmZW $\rightarrow$ TChiChipmZoffWoff.
Note that here, off shell particles always have a smaller mass than their on shell version, e.g. Zoff $\Leftrightarrow m_{\mathrm{Z_{off}}} < m_{\mathrm{Z}}$.
This change can lead to some confusion regarding the categorization of simplified models that `SmodelS` performs. CMS and ATLAS results constrain the final state and not the (off shell) gauge boson that produced them. For that reason, while e.g. the leptonic decay mode of an off shell gauge boson may be constrained (or outside grid), the same does not have to be true for the hadronic decay modes. The leptonic decay mode might then be categorized as outside grid, while the hadronic decay mode is categorized as missing.[3]

[3] See Section 5.5 for definition of constrained, outside grid, and missing.

6 Scan of pMSSM Parameter Space

A phenomenological study was performed using `SmodelS` on the surviving points of a parameter scan of the pMSSM done by the CMS collaboration [105]. The goal was to identify the missing simplified models that occur most often in the pMSSM scan. Information on the scan is given in Section 6.1. The results using `SmodelS` are discussed in Section 6.2. An analysis on the naturalness of the important missing simplified models that `SmodelS` uncovered is detailed in Section 6.3.

6.1 The Parameter Scan

The original scan [105] was created using a Markov Chain Monte Carlo method, where the point density follows a flat distribution in the initial scan parameters and contains approximately 20 million points. The points are subject to the following constraints:

- All BSM masses are below 3 TeV;
- The LSP is the $\tilde{\chi}_1^0$;
- Constraints by low-energy physics results, including:
  - The anomalous magnetic moment of the muon, a_μ;
  - Constraints from B meson decays;
  - Pre-LHC constraints of the top mass and the Higgs mass. Notable, these do not contain dark matter contraints to avoid a bias from cosmological assumptions.
- No long lived BSM particles. This constraint is only added to the prior after the sampling of the 20 million points and reduces their number by approximately 30%.

The argument for restricting the masses of BSM particles to less than 3 TeV is that the scan was performed with the LHC in mind. Higher masses are unlikely to be accessible by the LHC and were thus not included in the scan. However, this choice also excludes points where some SUSY particles might be discoverable at the LHC but at least one of the SUSY particles has a mass above 3 TeV. This introduces an inherent bias against models where the masses of the SUSY particles cover a large range. This scenario is present in a very large fraction of the possible realizations of the pMSSM. However, such scenarios are not expected to provide new phenomenology that is testable with LHC, since masses of $\mathcal{O}(3\,\text{TeV})$ are already quite decoupled from the masses that LHC is sensitive to. Thus, any increase in the masses of particles whose mass is near the boundary of 3 TeV will not notably change the phenomenology.

The parameter points used for this thesis are arrived at in the following way (See also Figure 21).

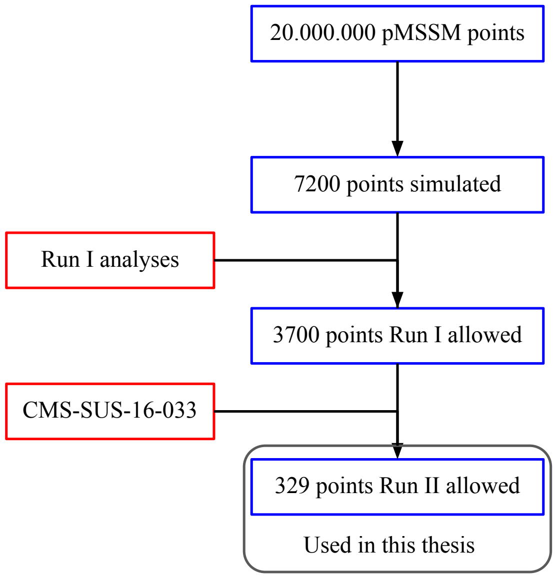

Figure 21: Origin of the parameter points used in this thesis. 20 million points were created and 7200 simulated in the context of a CMS analysis [105]. This CMS analysis then applied an extensive set of run I analyses on the 7200, 3700 of which are still allowed afterwards. One additional CMS run II analysis [61] was applied in the context of a group internal study, excluding all but 329 points.

Of the original 20 million points, which are subject to the constraints above, 7200 were randomly selected and simulated. This constitutes a very sparse scan that can not be expected to cover the whole phenomenology of the pMSSM. The 7200 points were then subjected to the constraints given by all LHC run I results. After that, about 3700 points remain that are not excluded. The 3700 points that are not excluded by the run I results are further subjected to one CMS run II analysis [61] within the context of that analysis. The run II search targets multijet events with missing transverse momentum and is very constraining in the strong sector. This one run II analysis reduces the non excluded points of the scan by another factor of 10, with only 329 points remaining that can not be excluded. It is expected that this analysis is the most constraining run II analysis to date, so that the number of 329 remaining points can only be reduced by a negligible amount if more run II analyses were used to constrain them.
These 329 remaining points are taken as the basis for study in this thesis.

6.2 SmodelS Results

`SmodelS` was used on the 329 parameter points that are arrived at in the previous section. It was found that none of the surviving points can be excluded by CMS and ATLAS using `SmodelS`. This is not unexpected, as these parameter points were subjected to an extensive set of run I results, as well as the most constraining result from run II. Furthermore, `SmodelS` does not include all run II results, and its limits are always weaker than those of dedicated analyses.

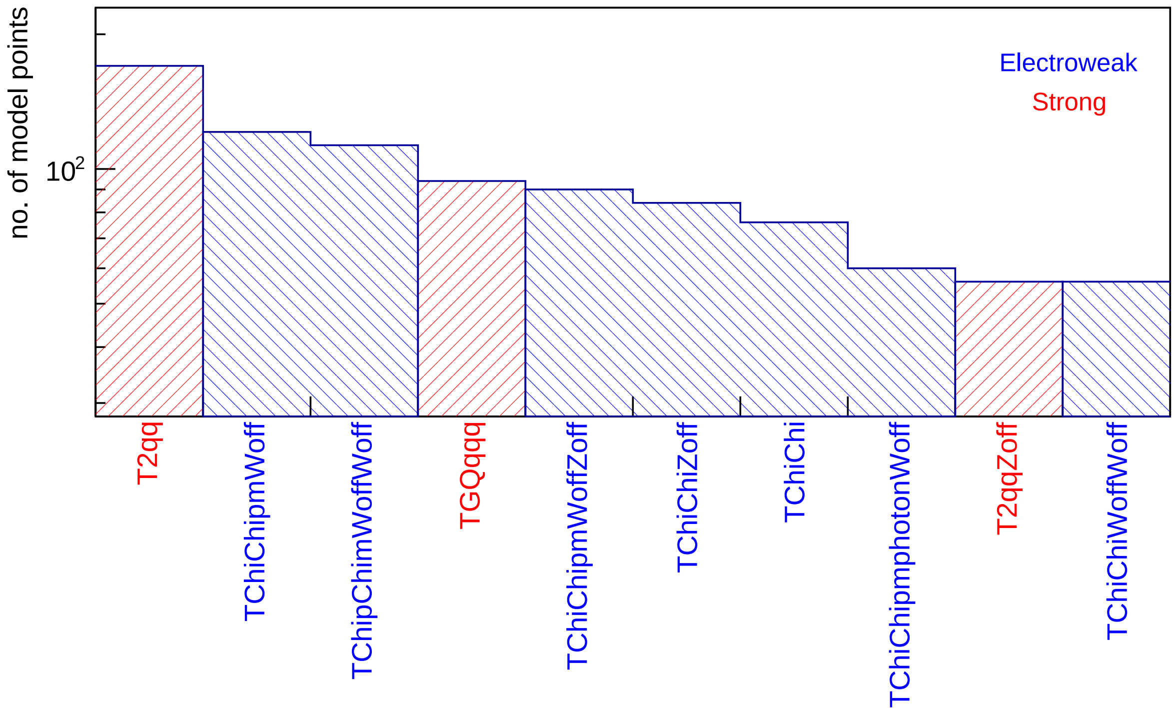

Figure 22: Occurrence multiplicity of missing topologies and outside grid topologies in the surviving 329 parameter points. The label on the x axis is the TxName of the model, its value on the y axis is the number of parameter points it occurred in. Models are colored red if they are produced via the strong force, and blue if they are produced via the electroweak force.

The weight threshold for this analysis is set to 0.005 fb. The value corresponds to roughly 1 particle expected at 200 fb^{-1} and should avoid the problem of the elementary decay mode weights falling below threshold for models that would otherwise produce a signal that may be detectable. The invisible compression and mass compression features of `SmodelS` are enabled with the mass compression threshold at $m_{\mathrm{compress}} = 0.1\,\mathrm{GeV}$. The threshold is set so as to avoid including cases where the decay products are unlikely to be reconstructed by the CMS detector. Figure 22 shows the number of full models among the 329 input models in which the respective missing simplified models (and outside grid simplified models) occur. As a reminder, the fact that not every pMSSM points has the same simplified models in its spectrum is owed to the fact that there is a weight threshold in place, below which simplified models are rejected and not included in the SMS.

Of the 10 most common missing simplified models, three are simplified models predominantly produced by strong interaction (red). The remaining 7 are simplified models produced by the electroweak interaction (blue). In decreasing order of the number of pMSSM points they occurred in, the 10 most commonly occurring simplified models are (see also Figure 23):

- T2qq ($\tilde{q}\,\tilde{q} \rightarrow qq\tilde{\chi}^0_1\,\tilde{\chi}^0_1$): The most commonly occurring missing simplified model. This model has been thoroughly analyzed (see e.g. [61, 106]) and is part of the outside grid topologies, i.e. the squark masses in the 329 parameter points are above the masses considered by CMS and ATLAS analyses and are currently out of reach of any experiment. As the purpose of this work is the identification of simplified models that have not yet been thoroughly analyzed, this model is not considered further here.

- TChiChipmWoff ($\tilde{\chi}_1^{\pm}\,\tilde{\chi}_1^0 \to W^*\tilde{\chi}_1^0\,\tilde{\chi}_1^0$): Production of a $\tilde{\chi}_1^{\pm}$-$\tilde{\chi}_1^0$ pair. The $\tilde{\chi}_1^{\pm}$ decays into the $\tilde{\chi}_1^0$ and an off shell W, due to a mass difference $\Delta m_{\tilde{\chi}_1^{\pm},\tilde{\chi}_1^0} < m_W$.

- TChipChimWoffWoff ($\tilde{\chi}_1^{\pm}\,\tilde{\chi}_1^{\pm} \to W^*W^*\tilde{\chi}_1^0\,\tilde{\chi}_1^0$): Branch symmetric version of TChiChipm-Woff. Almost all parameter points that contain TChiChipmWoff also contain this simplified model. In the few parameter points were this in not the case, the weight of TChipChimWoffWoff falls below the weight threshold.

- TGQqqq ($\tilde{g}\,\tilde{q} \to q\,q\,q\,\tilde{\chi}_1^0\,\tilde{\chi}_1^0$): Production of a $\tilde{g}$-$\tilde{q}$ pair. At first glance, this model constitutes a candidate for a search in this thesis. An argument against this model is that the cross section of this simplified model is usually very low among the pMSSM points. For example, it does not appear in Figure 25.

- TChiChipmWoffZoff ($\tilde{\chi}_2^0\,\tilde{\chi}_1^{\pm} \to Z^*W^*\tilde{\chi}_1^0\,\tilde{\chi}_1^0$): Production of a $\tilde{\chi}_2^0$-$\tilde{\chi}_1^{\pm}$ pair. Both of them decay into the $\tilde{\chi}_1^0$ and an off shell gauge boson. This means that in the pMSSM parameter points this models occurs in, both $\Delta m_{\tilde{\chi}_1^{\pm},\tilde{\chi}_1^0} < m_W$ and $\Delta m_{\tilde{\chi}_2^0,\tilde{\chi}_1^0} < m_Z$ are true.

- TChiChiZoff ($\tilde{\chi}_2^0\,\tilde{\chi}_1^0 \to Z^*\tilde{\chi}_1^0\,\tilde{\chi}_1^0$):Production of a $\tilde{\chi}_2^0$-$\tilde{\chi}_1^0$ pair, where the $\tilde{\chi}_2^0$ decays to the $\tilde{\chi}_1^0$ and a Z^*. In parameter points that feature this simplified model, $\Delta m_{\tilde{\chi}_2^0,\tilde{\chi}_1^0} < m_Z$ is true.

- TChiChi ($\tilde{\chi}_2^0\,\tilde{\chi}_1^0 \to \tilde{\chi}_1^0\,\tilde{\chi}_1^0$): The same model as TChiChiZoff, but with the Z^* decaying to neutrinos, which are then compressed by `SmodelS`.

- TChiChipmphotonWoff ($\tilde{\chi}_2^0\,\tilde{\chi}_1^{\pm} \to \gamma W^*\tilde{\chi}_1^0\,\tilde{\chi}_1^0$): Production of a $\tilde{\chi}_2^0$-$\tilde{\chi}_1^{\pm}$ pair, similar to the simplified model TChiChipmWoffZoff. The difference between the two simplified models is that the $\tilde{\chi}_2^0$ decays to a photon instead of a Z^*. If the $\tilde{\chi}_2^0$ is bino-like, the cross section for this simplified model is higher than for TChiChipmWoffZoff. If the $\tilde{\chi}_2^0$ is higgsino-like, the cross section for TChiChipmWoffZoff is higher.

- T2qqZoff ($\tilde{q}\,\tilde{q} \to q\,q\,Z^*\tilde{\chi}_1^0\,\tilde{\chi}_1^0$): Pair production of squarks, where one squark directly decays to the $\tilde{\chi}_1^0$, and the squark in the other branch first decays into the $\tilde{\chi}_2^0$ and a quark. The $\tilde{\chi}_2^0$ then decays into the $\tilde{\chi}_1^0$ and an off shell Z.

- TChiChiWoffWoff ($\tilde{\chi}_2^0\,\tilde{\chi}_1^0 \to W^*W^*\tilde{\chi}_1^0\,\tilde{\chi}_1^0$): Production of a $\tilde{\chi}_2^0$-$\tilde{\chi}_1^0$ pair. The $\tilde{\chi}_2^0$ first decays into a W^* and a $\tilde{\chi}_1^{\pm}$, which then decays into another W^* and the $\tilde{\chi}_1^0$. This simplified model occurs when the pMSSM point features a mass hierarchy of $m_{\chi_1^0} < m_{\chi_1^{\pm}} < m_{\chi_2^0}$. We can conclude that this mass hierarchy occurs at least as often among the pMSSM points as this simplified model does in the simplified model spectra.

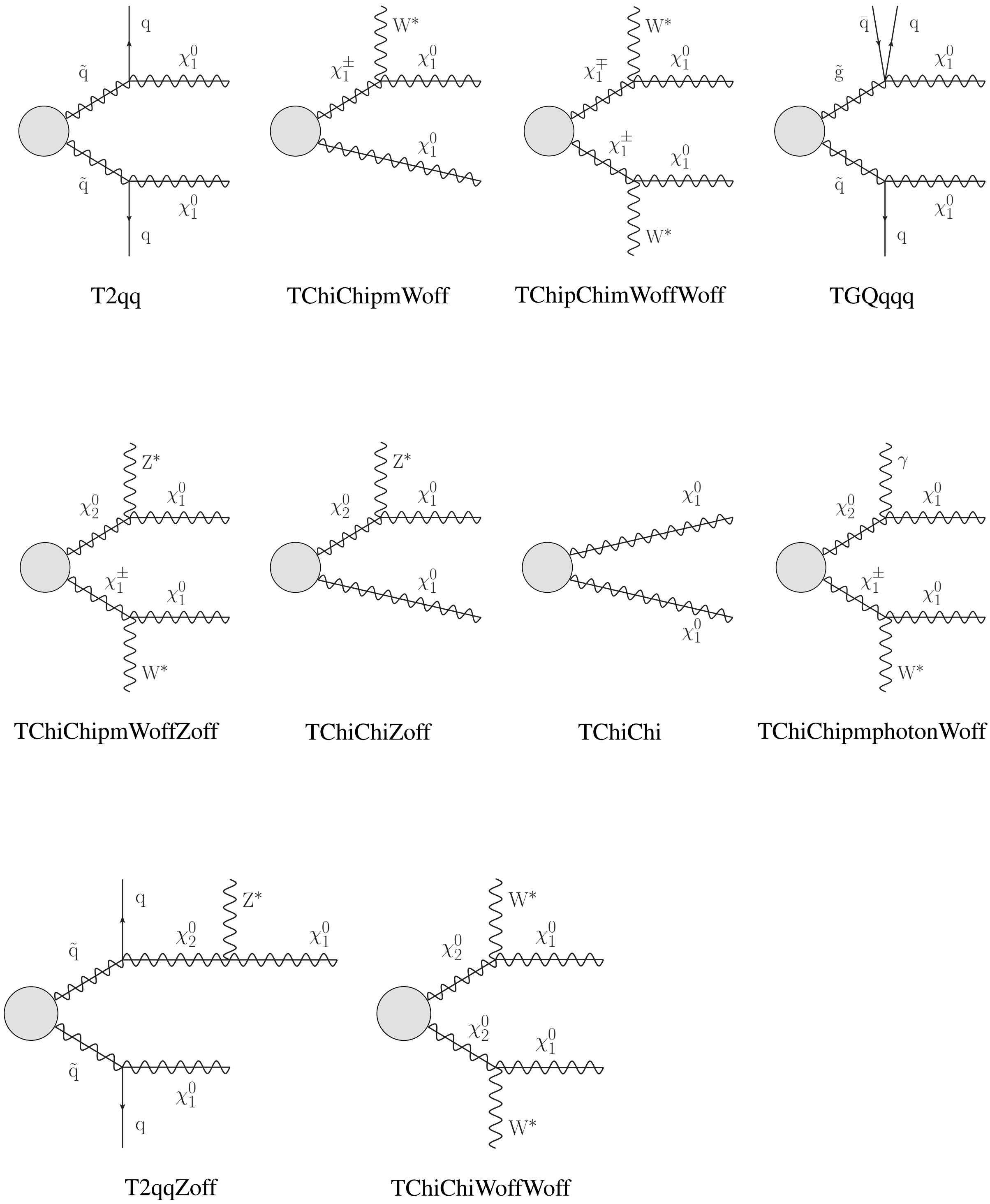

Figure 23: Most common outside grid and missing simplified models in the surviving parameter points. Feynman diagrams produced with `Jaxodraw`[8].

Simplified models whose TxName prefix contains "Chi" are simplified models with electroweak production of gauginos (compare Table 5). These electroweak gaugino simplified models also contain the tag "off" in the appendix of their TxName (except for TChiChi), which means that the mass difference of the SUSY particles involved at the vertices that also contain an off shell gauge boson have a mass difference of less than the on shell mass of the gauge boson. Figure 24 shows the Feynman diagrams of the four most common electroweak simplified models, the TChiChipmWoff, the TChipChimWoffWoff, the TChiChipmWoffZoff and the TChiChiZoff. Their weight distribution against the mass differences of the respective primary SUSY particle and the $\widetilde{\chi}_1^0$, namely $\Delta m_{\widetilde{\chi}_1^{\pm},\widetilde{\chi}_1^0}$, and $\Delta m_{\widetilde{\chi}_2^0,\widetilde{\chi}_1^0}$, can be seen in Figures 26 and 27, respectively. The figures show that most of the pMSSM points that contain any of these electroweak simplified model display a compressed gaugino spectrum with characteristic mass differences between 1 GeV and 10 GeV. The distribution of $\Delta m_{\widetilde{\chi}_1^{\pm},\widetilde{\chi}_1^0}$ values is shifted towards smaller mass differences compared to $\Delta m_{\widetilde{\chi}_2^0,\widetilde{\chi}_1^0}$. This abundance of compressed gaugino spectra is taken as a motivation to study them.

One also has access to the weights of the simplified models for each point. A possible use of the weight is shown in Figure 25, which is ordered by and shows the summed weights of the simplified models occurring in the simplified models spectra of the surviving pMSSM parameter points. An idea might be to use the weight to decide which model to analyze, as the higher cross section that comes with higher weights can only make an analysis easier. It was decided to not use that approach for the following reasons:

- Since the potential limits on the weight of different simplified models differ vastly due to different analysis strategies and requirements, the weight is not a good measure for comparing the different simplified models.

- Very few points might contribute the majority of weight to the sum, which means that an analysis might only help to eliminate very few points with high cross section that are not very relevant to the parameter space as a whole (see also Figures 26 and 27).

- The additional information that the weight carries are the cross sections and branching fractions for the particular model point. Since the parameter scan from which the model points used here originate is very sparse compared to the 19 dimensional parameter space of the pMSSM, any one point represents a big chunk of that parameter space. The exact values of the weight should be interpreted as benchmark points only.

- The weights that `SmodelS` uses are only computed up to leading order in this thesis.

There are some things that can be learned from Figure 25 however. The summed cross section of the T2qq model, which is the simplified model that occurs most often among the surviving pMSSM parameter points, is only the fifths highest, while the electroweak gaugino simplified models that occur most often among the pMSSM points also have the most summed weight of all simplified models. This is due to the fact that pMSSM parameter points with higher cross sections of the T2qq simplified model are excluded by existing searches. Note that the simplified model TGQqqq, which is the third most common missing simplified model in the parameter points, does not appear at all in Figure 25.

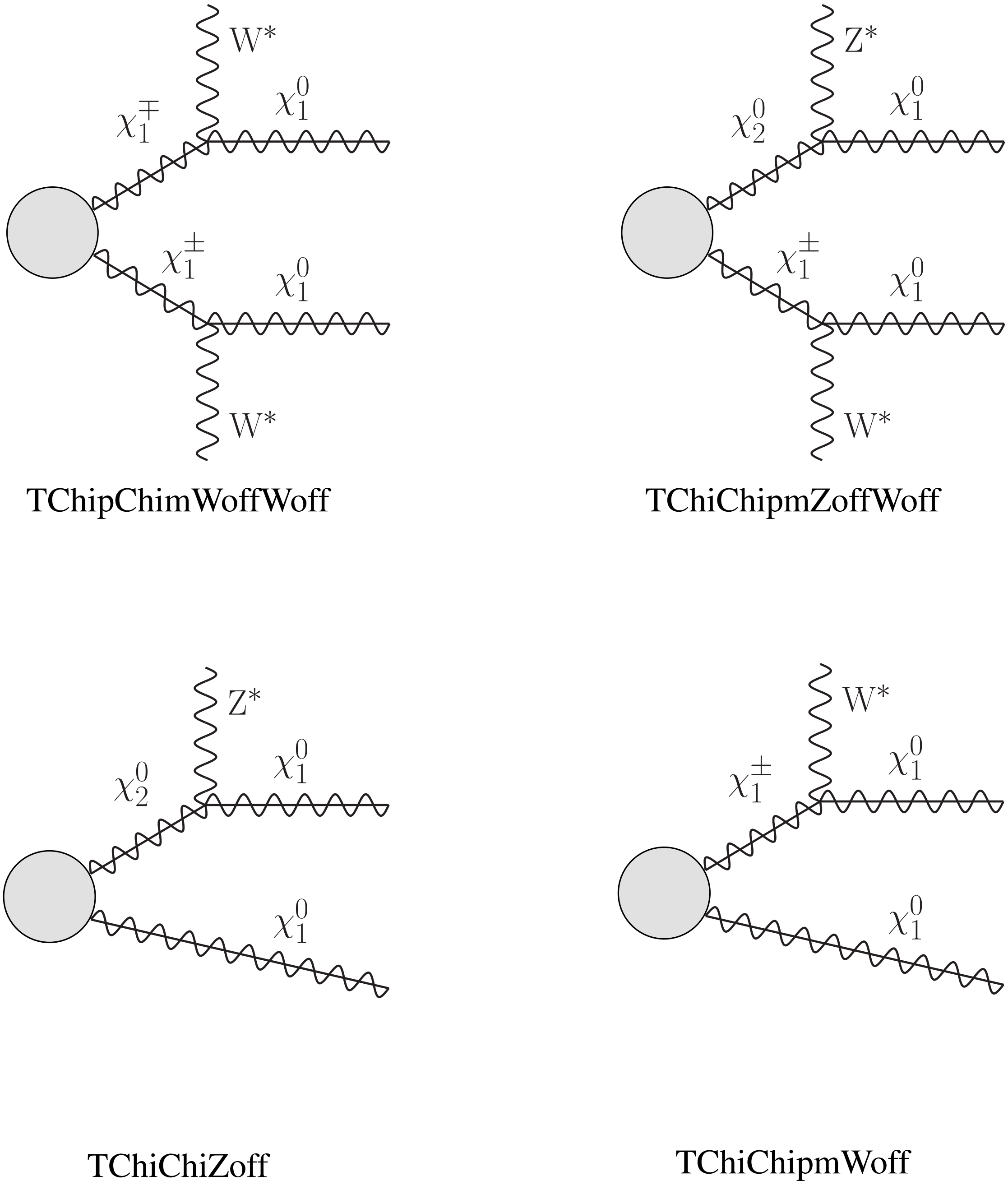

Figure 24: The four most common electroweak simplified models in the surviving points of the scan. They are the TChipChimWoffWoff (top left), the TChiChipmZoffWoff (top right), the TChiChiZoff (bottom left) and the TChiChipmWoff (bottom right). Feynman diagrams produced with `Jaxodraw`[8].

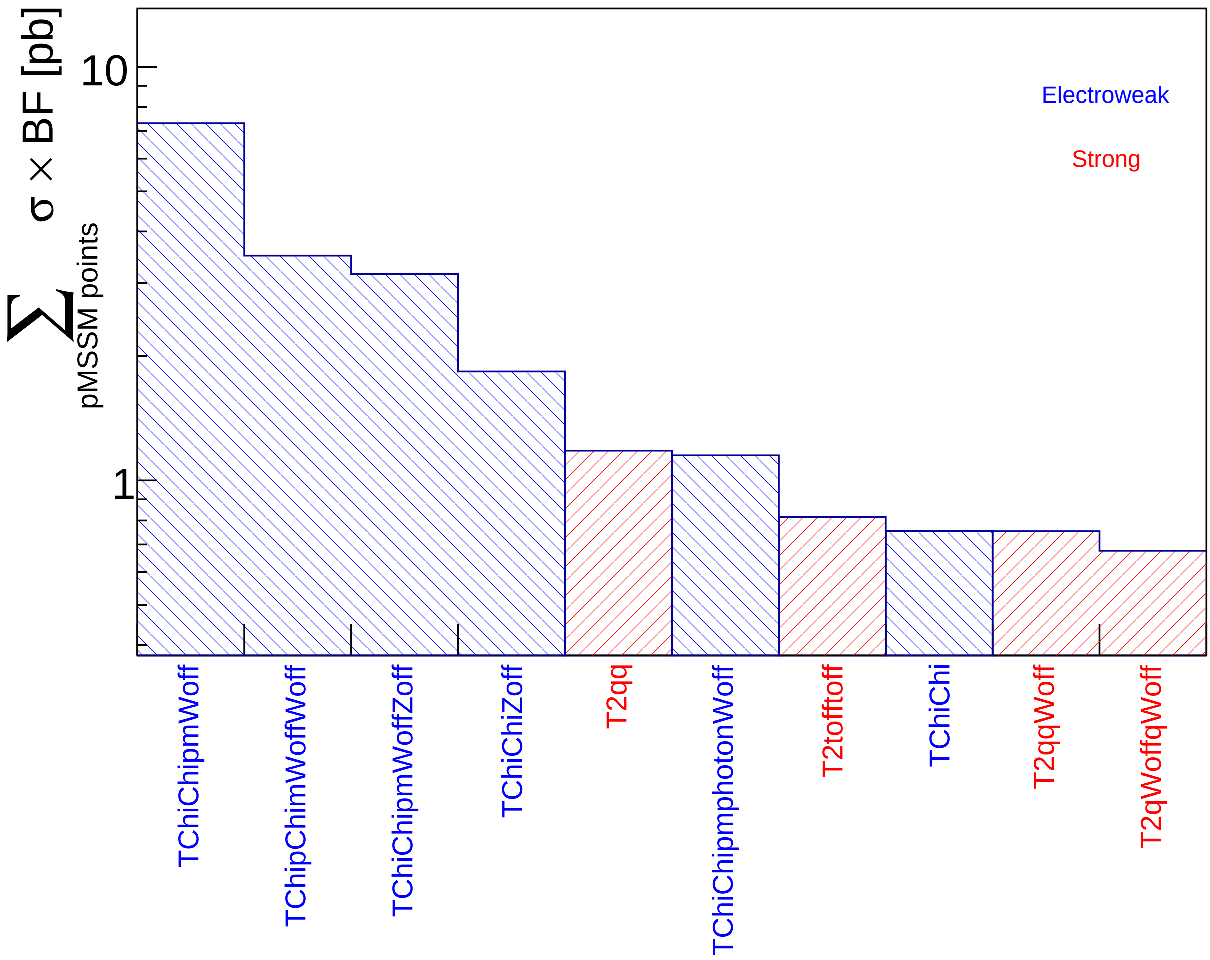

Figure 25: Top ten summed weights of missing simplified models in the surviving parameter scan points. Electroweak simplified models are given in blue, strong simplified models in red.

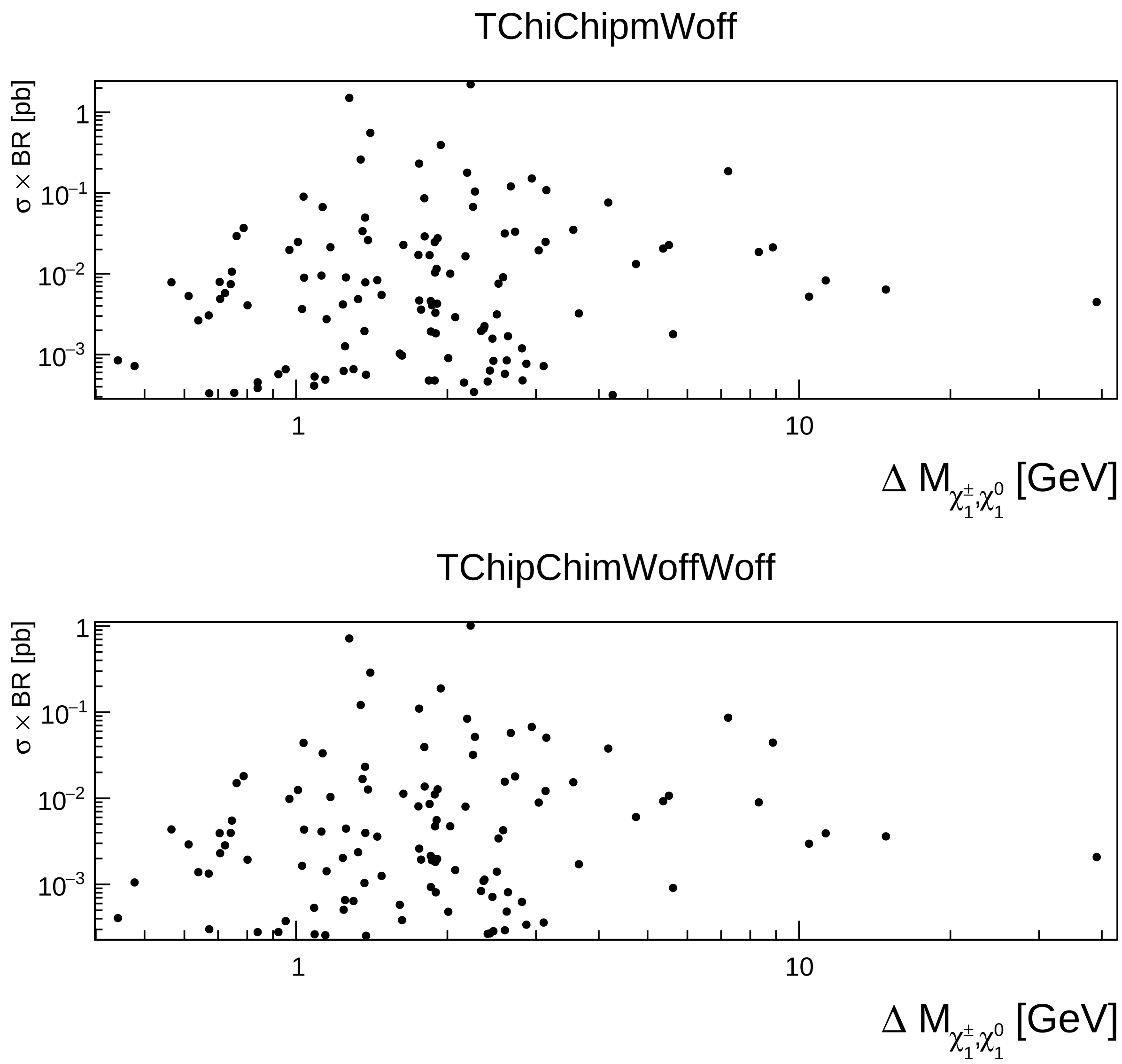

Figure 26: Distribution of the surviving pMSSM points in the weight-$\Delta m_{\tilde{\chi}_1^\pm,\tilde{\chi}_1^0}$ plane for the TChiChipmWoff and TChipChimWoffWoff simplified models. Most points have a weight of 10^{-3} fb to 10^{-2} fb and a mass difference of a few GeV, at most. No obvious correlation between the weight and the mass differences is visible.

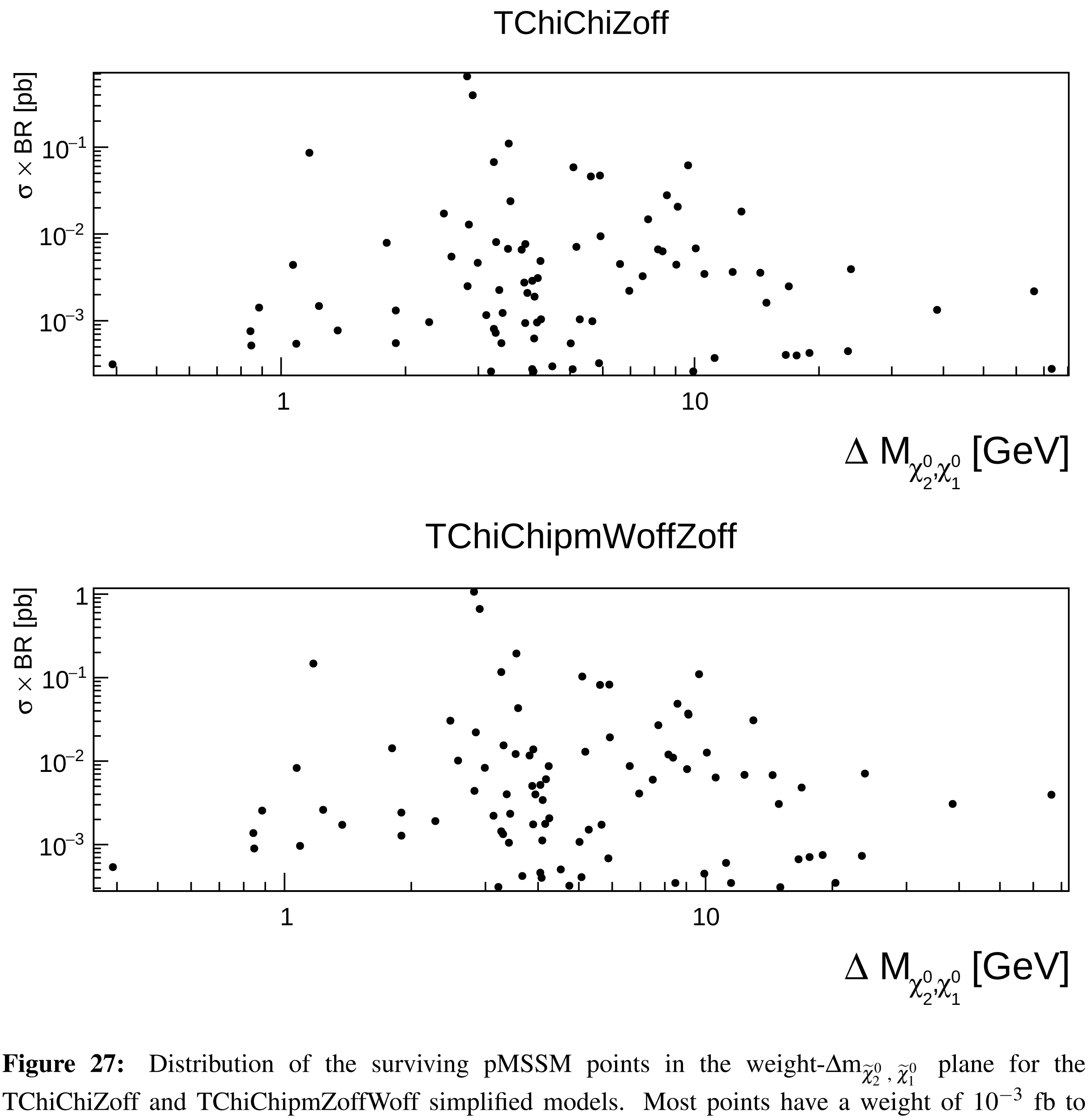

Figure 27: Distribution of the surviving pMSSM points in the weight-$\Delta m_{\tilde{\chi}_2^0,\tilde{\chi}_1^0}$ plane for the TChiChiZoff and TChiChipmZoffWoff simplified models. Most points have a weight of 10^{-3} fb to 10^{-2} fb and a mass difference of a few GeV, at most. No obvious correlation between the weight and the mass differences is visible.

6.3 Naturalness Study

An additional feature of the electroweak simplified models in Figure 24 is their tendency to occur in natural scenarios of the pMSSM that avoid the "little hierarchy problem" (see Section 3.1). The naturalness of a model is inversely related to its level of fine tuning. In general, measuring fine tuning is difficult and controversial. The method adopted in this thesis is to use the ΔEW [107] value of the model point. It is intended to measure the level of fine tuning in the electroweak sector (hence the EW). It is derived by minimizing the MSSM scalar potential, which yields the following Equation for the Z boson mass [15]:

$$\frac{\mathrm{m}_Z^2}{2} = \frac{\mathrm{m}_{H_d}^2 + \Sigma_d^d - \left(\mathrm{m}_{H_u}^2 + \Sigma_u^u\right)\tan^2\beta}{\tan^2\beta - 1} - \mu^2 \,. \tag{27}$$

The parameters on the right side of the equation are:

- $m_{H_d}^2$ and $m_{H_u}^2$: Soft SUSY breaking parameters;
- $\tan\beta$: The ratio of the Higgs field vacuum expectation values;
- μ: The higgsino mass parameter;
- $\sum_u^u$ and $\sum_d^d$: Various independent loop corrections.

Equation 27 can be written as a sum over the individual contributions $\mathrm{C}_i \in \mathrm{C}$, where

$$\mathrm{C} = \left\{ \frac{m_{H_d}^2}{\tan^2\beta - 1}, \frac{\Sigma_d^d}{\tan^2\beta - 1}, \frac{m_{H_u}^2 \cdot \tan^2\beta}{\tan^2\beta - 1}, \frac{\Sigma_u^u \cdot \tan^2\beta}{\tan^2\beta - 1}, \mu^2 \right\}.$$

ΔEW is then defined as [107]

$$\Delta\mathrm{EW} = \frac{\max(\mathrm{C}_i)}{\frac{m_Z}{2}} \,, \tag{28}$$

the maximum value of any summand in Equation 27 normalized to the Z mass. ΔEW is related to fine tuning in that if any summand in Equation 27 becomes large, i.e. is far removed from the Z mass, which results in a high value of ΔEW, there has to be fine tuning in the other parameters for the equation to remain valid. In this way, high values of ΔEW correspond to high levels of fine tuning and vice versa. However, there is no agreement on what level of fine tuning is "natural" and should be allowed, likewise what values of ΔEW should be considered natural. Figure 28 shows the ΔEW values of the parameter points of the scan and their distribution with respect to the four most commonly occurring electroweak simplified models. All of them are related to virtual W or Z bosons, resulting from nearly mass degenerate gauginos in the decay chain. The last bin is an overflow bin. It is clear from this that the electroweak simplified models tend to occur in models points which have comparatively low fine tuning, while those model points that do not contain these electroweak missing simplified models tend to have larger values of ΔEW. Considering these results, it was decided to take a closer look at these

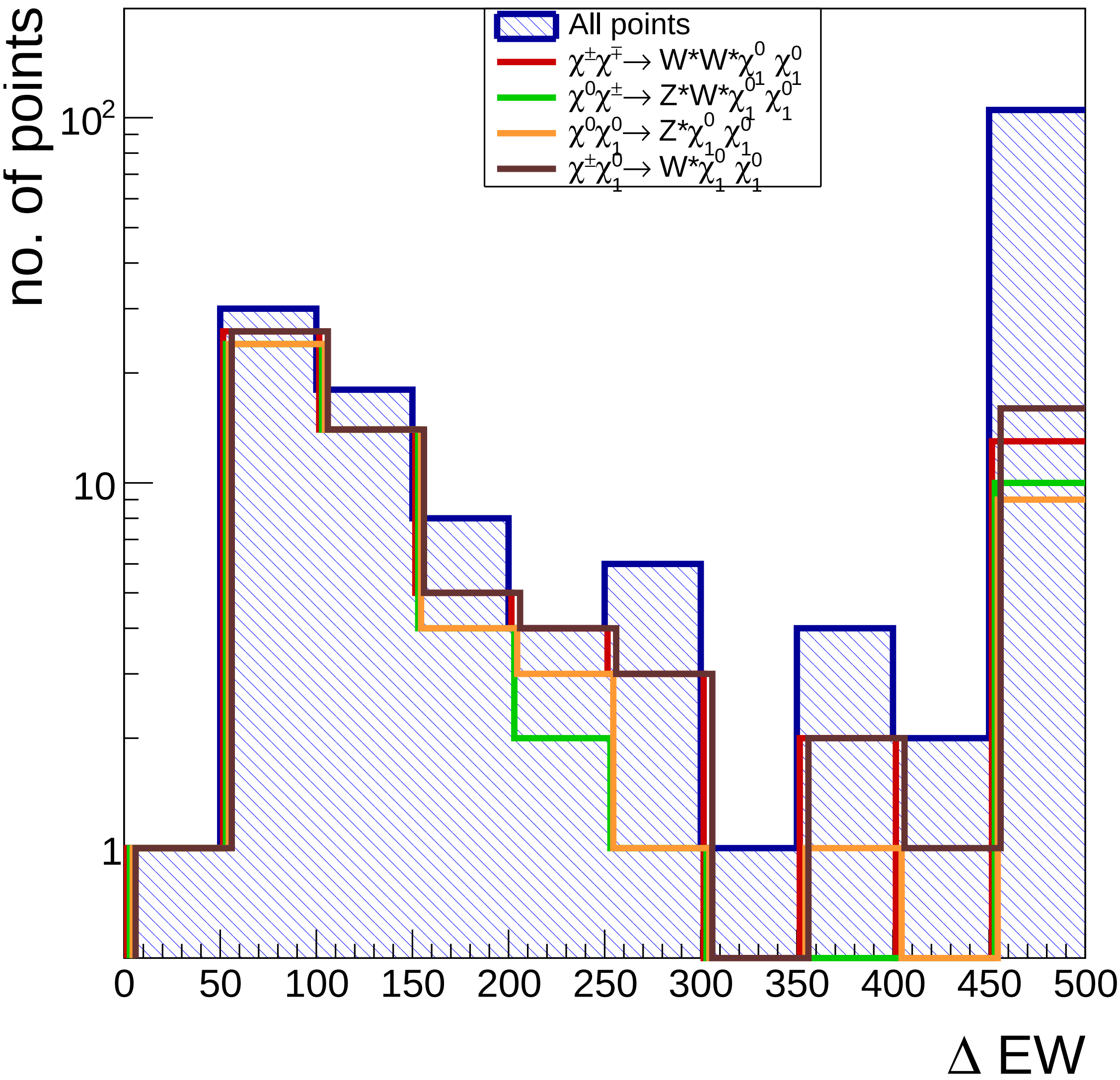

Figure 28: ΔEW values for points containing the respective electroweak simplified model. The last bin is an overflow bin. Points containing any of the electroweak simplified models with a weight above the `SmodelS` weight threshold tend to have low values of ΔEW, while those without any of the electroweak simplified models aggregate at high values of ΔEW. The differently colored histograms are offset slightly to increase readability. Note that the ΔEW was not available for every point in the scan, resulting in only 179 entries in this plot. However, the ratio of models containing the electroweak simplified models to models that do not is approximately the same in this plot as in for the full 329 points, so that no bias is introduced.

simplified models describing compressed gaugino spectra to ascertain whether a search can be sensitive to them.

7 Search for Signatures of Compressed Supersymmetric Particle Spectra

This section is on the study of very compressed electroweak gaugino models within the pMSSM. The phenomenological study in the previous sections showed that such models are not yet covered well by searches from the CMS and ATLAS collaborations. A general discussion of compressed electroweak models is given in Section 7.1. Section 7.2 describes a suitable benchmark model on which to optimize a search. The analysis proceeds with a detailed discussion of the target signature in Section 7.3, followed by a study of the most important backgrounds in Section 7.4. A baseline event selection is provided in Section 7.5. A procedure to increase the purity of the relevant tracks in signal events is described in Section 7.6. Section 7.7 contains a simultaneous optimization of event-level observables and a track selection.

7.1 Features of the Candidate Simplified Models

Four simplified model candidates for searches emerged from the phenomenological study in the previous chapters. All four simplified models feature the pair production of gauginos that decay to the LSP and a virtual gauge boson. The four simplified models are:

- TChipChimWoffWoff (see Figure 24, top left): This simplified model features just two new particles, the $\widetilde{\chi}_1^{\pm}$ and the $\widetilde{\chi}_1^0$. The $\widetilde{\chi}_1^{\pm}$ decays into the $\widetilde{\chi}_1^0$ and an off shell W boson (off shell in this context means $\Delta m_{\widetilde{\chi}_1^{\pm},\widetilde{\chi}_1^0} < m_W$). There are two identical branches in the simplified model, each featuring one such decay.

- TChiChipmZoffWoff (Figure 24, top right): This model features the production of a $\widetilde{\chi}_2^0$-$\widetilde{\chi}_1^{\pm}$ pair, where both decay into off shell gauge bosons and a $\widetilde{\chi}_1^0$. The simplified model contains one vertex per branch.

- TChiChiZoff (Figure 24, bottom left): This model described the production of a $\widetilde{\chi}_2^0$-$\widetilde{\chi}_1^0$ pair, where the $\widetilde{\chi}_2^0$ decays into an off shell Z boson and the $\widetilde{\chi}_1^0$.

- TChiChipmWoff (Figure 24, bottom right): This models features the production of a $\widetilde{\chi}_1^{\pm}$-$\widetilde{\chi}_1^0$ pair, where the $\widetilde{\chi}_1^{\pm}$ decays into an off shell W boson and the $\widetilde{\chi}_1^0$. Of the four models in consideration, it is the one that occurs most often among the surviving points of the scan.

The strategy of any search for the existence of these models is to identify characteristics of the decay products of the off shell Z or W bosons. The W has a high branching fraction of approximately 22% to a lepton (e,μ) neutrino pair, the rest of the time it decays to hadrons (33% with the tau lepton included). Generally, leptonic signatures are easier due to their rarity in the standard model, and the accuracy with which they are measured in the detector. However, the lepton identification efficiency drops sharply below 5 GeV, which means that in models with very compressed particle mass spectra, the decay products are difficult to reconstruct and identify. In addition, leptonic decays of the W always contain a neutrino, which can take away a large fraction of the energy of the decay and produces no visible signature in the CMS detector, contributing only to the missing transverse energy.

The Z boson has a very small branching fraction to leptons of approximately 6% (9% if the tau is included), the rest of the decays are hadronic. In contrast to the leptonic channel of the W boson, the leptonic decay of the Z boson does not produce any neutrinos and all of the energy of the decay goes into the leptons. This allows the probing of smaller mass splittings in the leptonic channel. However, the low branching fraction into leptons puts severe restrictions on the potential sensitivity of searches that target that decay channel. The alternative is to look at the hadronic decay modes of the Z boson, which is the focus of this part of the thesis.

7.2 Selection of a Benchmark Model

From the ΔEW study in Section 6, the parameter point with the lowest ΔEW, which corresponds to a value of ΔEW = 40.6, is selected as a benchmark model. The following analysis is optimized for that benchmark model. All of the simplified models discussed above occur for the benchmark model, their leading order cross sections are shown in Table 7. Of the four simplified models, TChiChipmWoff is assigned the highest weight by `SmodelS`, followed by TChipChimWoffWoff, TChiChipmZoffWoff, and TChiChiZoff, in that order. Around 20,000 Monte Carlo events were generated for the process $\tilde{\chi}_2^0\,\tilde{\chi}_1^{\pm} \rightarrow Z^* W^* \tilde{\chi}_1^0\,\tilde{\chi}_1^0$, corresponding to the simplified model TChiChipmZoffWoff. Note that the cross sections in Table 7 were not used to create Monte Carlo events, instead, `Pythia8` [41] was used at next-to-leading order precision (see Section 4.4). The masses of the SUSY particles, as well as the rest of the SUSY parameters of the benchmark point, can be found in Table 6.
The chosen model point contains a triplet of nearly mass degenerate gaugino states. The $\tilde{\chi}_1^0$ is the LSP, with a mass of $m_{\tilde{\chi}_1^0}$ = 303.8 GeV. The next to lightest sparticle (NLSP) is the $\tilde{\chi}_1^{\pm}$ with a mass of $m_{\tilde{\chi}_1^{\pm}}$ = 308.0 GeV. The third gaugino of the triplet is the $\tilde{\chi}_2^0$ with a mass of $m_{\tilde{\chi}_2^0}$ = 316.8 GeV. This leads to mass differences $\Delta m_{\tilde{\chi}_2^0,\tilde{\chi}_1^0}$ = 13 GeV and $\Delta m_{\tilde{\chi}_1^{\pm},\tilde{\chi}_1^0}$ = 4.2 GeV.

The very small value of $\Delta m_{\tilde{\chi}_1^{\pm},\tilde{\chi}_1^0}$ makes the identification of off shell W bosons extremely challenging, as the decay products are extremely soft in the rest frame of the $\tilde{\chi}_1^{\pm}$. The only way to use the leptonic channel of the off shell W boson is to select events in which the $\tilde{\chi}_1^{\pm}$ is boosted to such a degree that the lepton is likely to pass the lepton identification. Since the value of $m_{\tilde{\chi}_1^{\pm}}$ is large, we expect such events to be too rare given the size of LHC datasets, making this decay mode nonviable.

This leaves the hadronic decay mode of the W boson. However, the hadronic decay of the W offers no advantage over the hadronic decay mode of the Z boson from the $\tilde{\chi}_2^0$ decay, which has a much larger expected energy, since $\Delta m_{\tilde{\chi}_2^0,\tilde{\chi}_1^0}$ = 13 GeV. For this reason, the simplified models that produce a Z boson, the TChiChipmZoffWoff and the TChiChiZoff, are the target

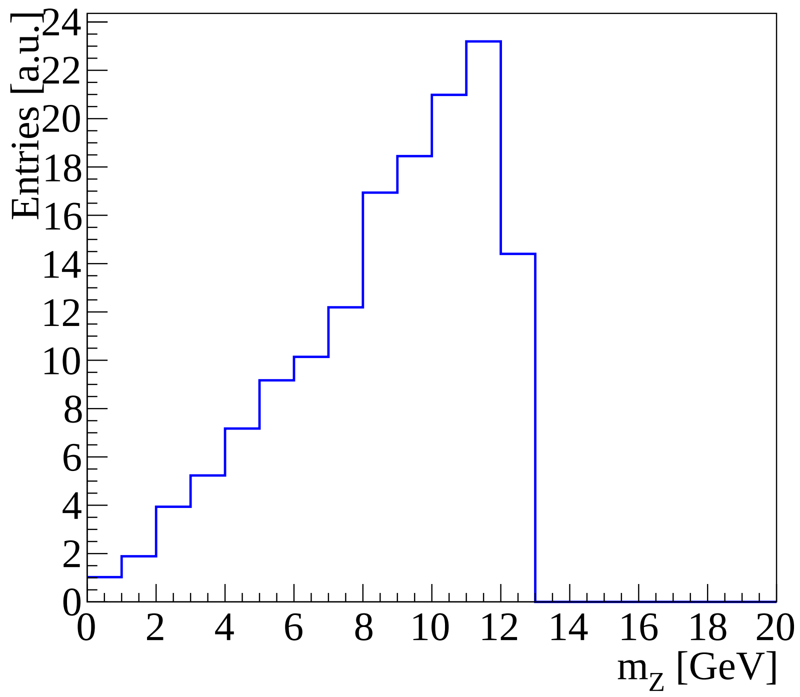

Figure 29: Invariant mass distribution of the off shell Z boson in the benchmark point. The distribution features a kinematic edge at $\Delta m_{\tilde{\chi}_2^0, \tilde{\chi}_1^0} = 13\,\text{GeV}$. This distribution shows the Monte Carlo truth, detector effects are not included.

of this analysis. Figure 29 shows the invariant mass distribution of the off shell Z boson in signal events before any cuts are applied. A promising analysis strategy is to reconstruct the mass distribution of the Z*, which exhibits a "shoulder" shape, falling off at the mass difference $\Delta m_{\tilde{\chi}_2^0, \tilde{\chi}_1^0} = 13$ GeV.

7.3 Analysis of Target Signature

The targeted processes are the simplified models TChiChipmZoffWoff and TChiChiZoff (see Figure 24). The first is the production of a $\tilde{\chi}_2^0$-$\tilde{\chi}_1^\pm$ pair, which then directly decay into the $\tilde{\chi}_1^0$ via off shell gauge boson. The second is the production of a $\tilde{\chi}_2^0$-$\tilde{\chi}_1^0$ pair, where the $\tilde{\chi}_2^0$ decays to the $\tilde{\chi}_1^0$ and an off shell Z boson. As a result of the small mass difference $\Delta m_{\tilde{\chi}_1^\pm, \tilde{\chi}_1^0}$ between the $\tilde{\chi}_1^\pm$ and the $\tilde{\chi}_1^0$, leading to a very low mass off shell W boson, the signatures of both simplified models are expected to look almost identical.

Because the mass differences of all three gauginos are very small compared to their absolute masses, the two primary gauginos in the process are expected to be produced back to back in the SUSY system, with almost identical energies. Because of this, there is very little $\not{E}_T$ inherent in the SUSY system. Any large value of $\not{E}_T$ is signal events must thus come from initial or final state radiation. The lack of significant $\not{E}_T$ presents a problem for triggering, since the only

Parameter	Value	Parameter	Value
$\tan\beta$	9.21	m_{t_R}	2138 GeV
M_1	1213 GeV	m_{d_R}	2470 GeV
M_2	724 GeV	m_{e_R}	1145 GeV
M_3	2340 GeV	m_{μ_R}	1145 GeV
A_t	-5877	m_{τ_R}	2460 GeV
A_b	-2016	$m_{q_{L,1}}$	2840 GeV
A_τ	5621	$m_{q_{L,2}}$	2840 GeV
μ	307 GeV	$m_{q_{L,3}}$	2303 GeV
m_A	2886 GeV	m_{u_R}	2037 GeV
m_{e_L}	366 GeV	m_{c_R}	2037 GeV
m_{μ_L}	366 GeV	m_{s_R}	2470 GeV
m_{τ_L}	744 GeV	m_{b_R}	669 GeV

Table 6: SUSY parameter values of the benchmark model

Simplified Model	$\sigma \times \sum \mathrm{BF}$
TChiChipmWoff	76 fb
TChiChipmWoffWoff	37 fb
TChiChipmZoffWoff	31 fb
TChiChiZoff	18 fb

Table 7: The four missing simplified models with the highest cross section in the benchmark model. The cross section given are computed using `Pythia8` at leading order precision. Note that these cross sections were not used to simulate events.

visible signature that is produced in the hard process has very little energy, in the order of a few GeV at most. Two possible choices of trigger remain:

- $\not{E}_T$ trigger: The trigger threshold is 100 GeV but does not become fully efficient until $\sim$ 200 GeV. The majority of signal events are lost with this trigger as it selects events in the tail of an exponential function.

- Combined $\not{E}_T$ + soft lepton trigger. Use of this trigger would allow the inclusion of events with smaller $\not{E}_T$. However, this trigger effectively limits the analysis to the leptonic decay channels and was thus deemed too restricting for this thesis.

In summary: The signal produces low-energy tracks in the order of a few GeV at most in the center of mass frame of the $\tilde{\chi}_2^0$. The energy of the tracks in the lab frame is expected to be of the same order, as no large Lorentz boost is expected for the SUSY system due to the large mass of the SUSY initial state of around 600 GeV. The SUSY system has very little inherent $\not{E}_T$, as the initial pair of SUSY particles is nearly mass degenerate with a mass difference of $\Delta m_{\tilde{\chi}_2^0, \tilde{\chi}_1^0}$ = 13 GeV. For values of $\not{E}_T$ above the trigger threshold, the $\not{E}_T$ derives almost exclusively from a boost of the SUSY system against one or more initial-state-radiation (ISR) jets.

7.4 Background Study

The most significant Standard Model background processes to the signal are discussed. The signal produces a low-energy final state with a value of $\not{E}_T$ that is close to the H_T of the event. H_T is defined as

$$H_T = \sum_{\text{Jets}} p_T^{\text{Jet}} \quad , \tag{29}$$

where jets are required to have p_T >30 GeV and $|\eta| < 3$.

QCD

Due to its enormous cross section, QCD can produce almost any signature to some degree. One of the few effective handles on the QCD background is the missing transverse energy. The only "real" missing transverse energy source in QCD events are rare low-energy neutrinos which can arise in the presence of 2^{nd} and 3^{nd} generation quark decays and induce low amounts of $\not{E}_T$. These real $\not{E}_T$ contributions are irrelevant compared to the missing transverse energy faked by the mis-measurement of jets.

QCD is the dominant background for small values of $\not{E}_T$, and decreases sharply for increasing values of $\not{E}_T$. Even after applying an $\not{E}_T$ cut to emulate the trigger, QCD remains a relevant background.

$t\bar{t}$ + Jets

Pair production of top quarks with associated jets. Neutrinos from leptonic W decays in the top quark decay chain generate $\not{E}_T$ in addition to fake contributions to the $\not{E}_T$ due to the mis-measurement of jets. An effective handle on $t\bar{t}$ + Jets is provided by a veto on b-tagged jets.

$\mathbf{Z + Jets \rightarrow \nu\nu + Jets}$

Production of a Z boson with an associated jet, where the Z boson decays to neutrinos, which produces a $\not{E}_T$ signature and thus mimics the signal. This process looks almost identical to the signal process and is an irreducible background.

$\mathbf{W + Jets \rightarrow l\nu + Jets}$

Production of a W boson decaying leptonically with additional jets in the event. The neutrino from leptonic W decays can create the $\not{E}_T$ to pass the trigger. If the lepton is not reconstructed, the process looks like an ISR induced $\not{E}_T$ signature and mimics the signal to a large degree. This background is sub dominant to the $Z + \text{Jets} \rightarrow \nu\nu + \text{Jets}$ background. If the lepton has a small p_T and is reconstructed, the process can fake the leptonic decay mode of the Z^* in the signal model.

7.5 Event Selection

A baseline event selection is defined using the following observables:

$\not{E}_T$

An $\not{E}_T$ > 150 GeV cut is applied. This cut is designed to mimic the trigger, and the threshold is chosen to ensure the trigger efficiency is reasonably high. The vast majority of QCD events, as well as a large fraction of the signal is cut away by this requirement.

H_T -$\not{E}_T$ Plane

A two-dimensional cut in the $\not{E}_T$ -H_T plane is applied by requiring H_T > $\not{E}_T$ + 100 GeV. This cut greatly reduces the QCD background, since $\not{E}_T$ in QCD events is usually present due to errors in the measurement of jet energies. Therefore, the $\not{E}_T$ in QCD events scales with the H_T. However, since $\not{E}_T$ is constructed vectorially and the jets contributing to $\not{E}_T$ can lie in different hemispheres, the total $\not{E}_T$ in QCD events can partially cancel. The same does not happen for H_T, as is is constructed as a scalar sum. This leads to high values of H_T compared to $\not{E}_T$ in QCD events. The specific value of H_T > $\not{E}_T$ + 100 GeV is fine-tuned to the model point and cannot be trivially propagated to other pMSSM points with different masses.

H_T -$\not{E}_T$ Fraction

The observable $\frac{H_T}{\not{E}_T}$ is similar to the two dimensional H_T cut, but less model specific. The cut employed in this work is $0.7 < \frac{H_T}{E_T} < 1.3$. It also helps to reject QCD events, but is less powerful than the two dimensional cut. There is still a gain on top of the two dimensional cut.

$\not{E}_T$ significance
A cut of $\not{E}_T$ significance < 25 $\sqrt{\text{GeV}}$ is applied, which is defined as

$$\not{E}_T \text{ significance} = \frac{\not{E}_T}{\sqrt{H_T}} \quad . \tag{30}$$

This observable again tries to exploit the different shape of background and signal events in the H_T -$\not{E}_T$ plane. The $\not{E}_T$ significance performs worse than either of the two observables relating $\not{E}_T$ and H_T discussed above.

$\Delta\Phi_{\text{jet1},\not{E}_T}$
In order to pass the $\not{E}_T$ cut, signal events have to be boosted by an initial state radiation jet. This usually leads to a large angular separation between the leading jet and the SUSY system, which is usually aligned with the $\not{E}_T$, in the azimuthal angle Φ and consequently large value of $\Delta\Phi_{\text{jet1},\not{E}_T}$, which is defined as

$$\Delta\Phi_{\text{jet1},\not{E}_T} = \left|\Phi_{\text{jet1}} - \Phi_{\not{E}_T}\right|, \tag{31}$$

where jet1 refers to the leading jet, i.e. the one with the highest p_T , and $\Phi_{\not{E}_T}$ is the Φ value of the vector assigned to the $\not{E}_T$. The cut chosen in this thesis is $\Delta\Phi_{\text{jet1},\not{E}_T} > 2.5$. This cut is used primarily to reduce the QCD background.

$\Delta\Phi_{\text{jet2},\not{E}_T}$
Similar to $\Delta\Phi_{\text{jet1},\not{E}_T}$, but instead of the jet with the highest p_T , the jet with the second highest p_T is used. The cut value that is chosen is $\Delta\Phi_{\text{jet2},\not{E}_T} > 1.5$.

Jet Multiplicity
The signal produces a negligible number of events with more than 4 jets, which is why events with $N_{\text{Jets}} > 4$ are rejected. In this context, jets are required to have a p_T of at least 30 GeV to be considered.

B-tag Veto
Finally, to reject $t\bar{t}$ background, a veto on b-tagged jets is applied, where b jets are those with a value of CSV > 0.8484.

Lepton Veto
A veto on events containing a lepton with a p_T > 10 GeV is applied. Leptons from the signal process have a low energy, so a veto on highly energetic leptons provides a handle on the $W + \text{Jets} \rightarrow l\nu + \text{Jets}$ background.

These cuts perform well in reducing the QCD and $t\bar{t}$ background, but are unable to significantly reduce the $Z + \text{Jets} \rightarrow \nu\nu + \text{Jets}$ and the $W + \text{Jets} \rightarrow l\nu + \text{Jets}$ background. However, none of these cuts use track information, and all the observables are event-level observables. A further optimization using track information is presented in Section 7.7.

Figures 30 and 31 show the signal and background event distributions in the event selection observables. The observables are all shown with the full event selection applied, except for the cut on the observable in question. For example, in the distribution of N_{Jets}, all cuts except the one on N_{Jets} itself are applied. The sole exception to this is the $\not{E}_T$ distribution, as the $\not{E}_T$ >150 GeV requirement is taken to represent the trigger and thus looking at values of $\not{E}_T$ <150 GeV is not needed. The 2-dimensional distributions in the $\not{E}_T$ - H_T-plane are shown in Figure 32. The distributions are shown with only the $\not{E}_T$ constraint applied.

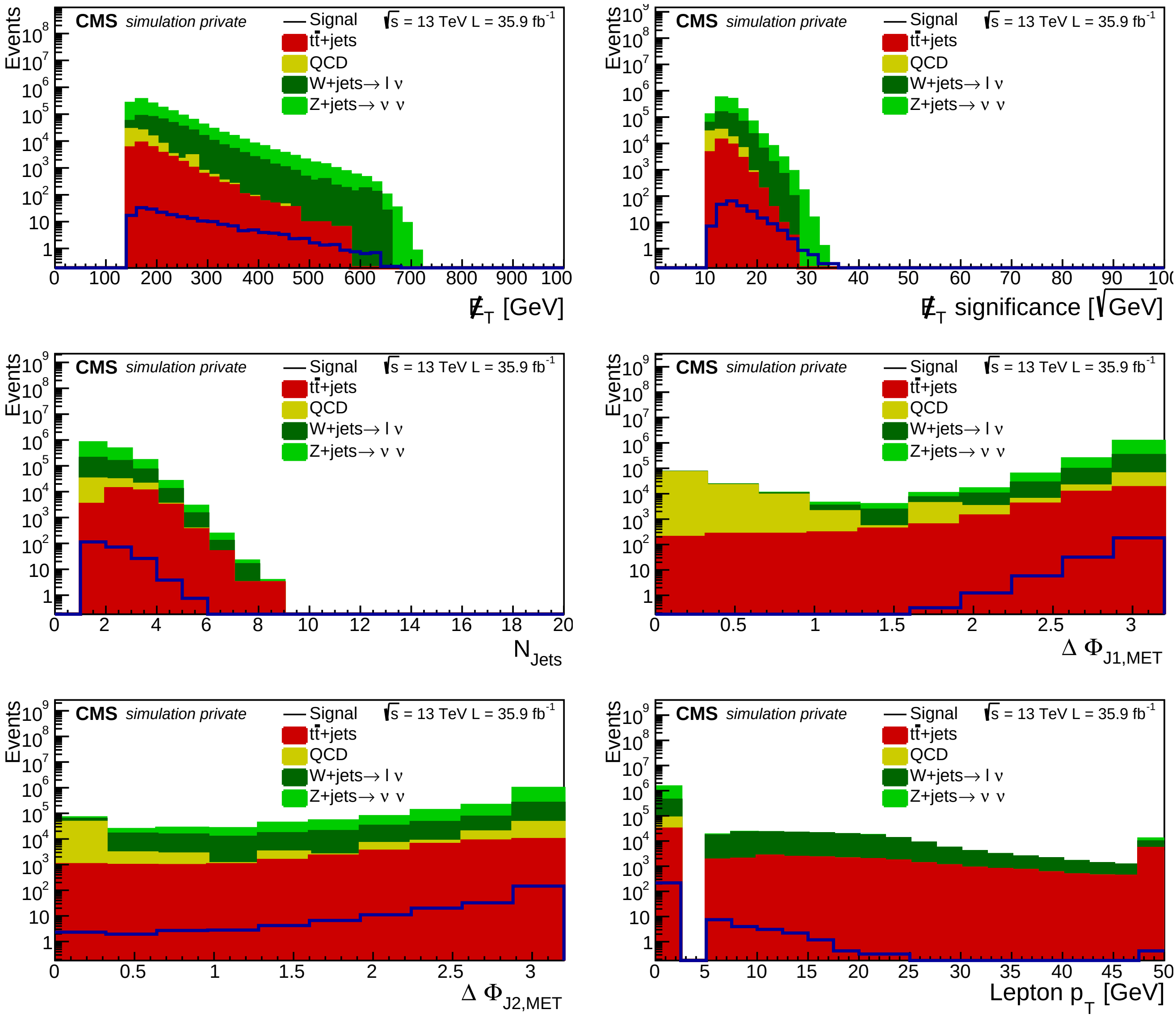

Figure 30: Distributions of signal and background in the observables used in the event selection. For each observable, the complete event selection is applied except for the cut on the observable itself. The exception to this is the $\not{E}_T$ distribution, in which the complete event selection is applied. The observables shown are $\not{E}_T$ (top left), $\not{E}_T$ significance (top right), Jet multiplicity (middle left), $\Delta\Phi_{\mathrm{jet1},\not{E}_T}$ (middle right), $\Delta\Phi_{\mathrm{jet2},\not{E}_T}$ (bottom left), and the p_T of the leading lepton (bottom right). The first bin of this last plot are exclusively events where no lepton was reconstructed

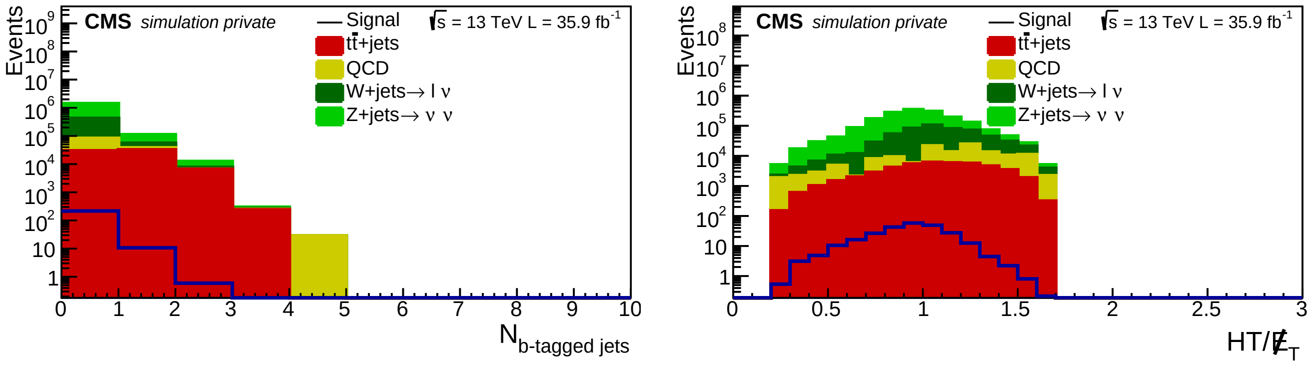

Figure 31: Distributions of signal and background in the observables used in the event selection. For each observable, the complete event selection is applied except for the cut on the observable itself. The observables shown are the multiplicity of b-tagged jets (left) and the fraction $\frac{H_T}{\not{E}_T}$ (right).

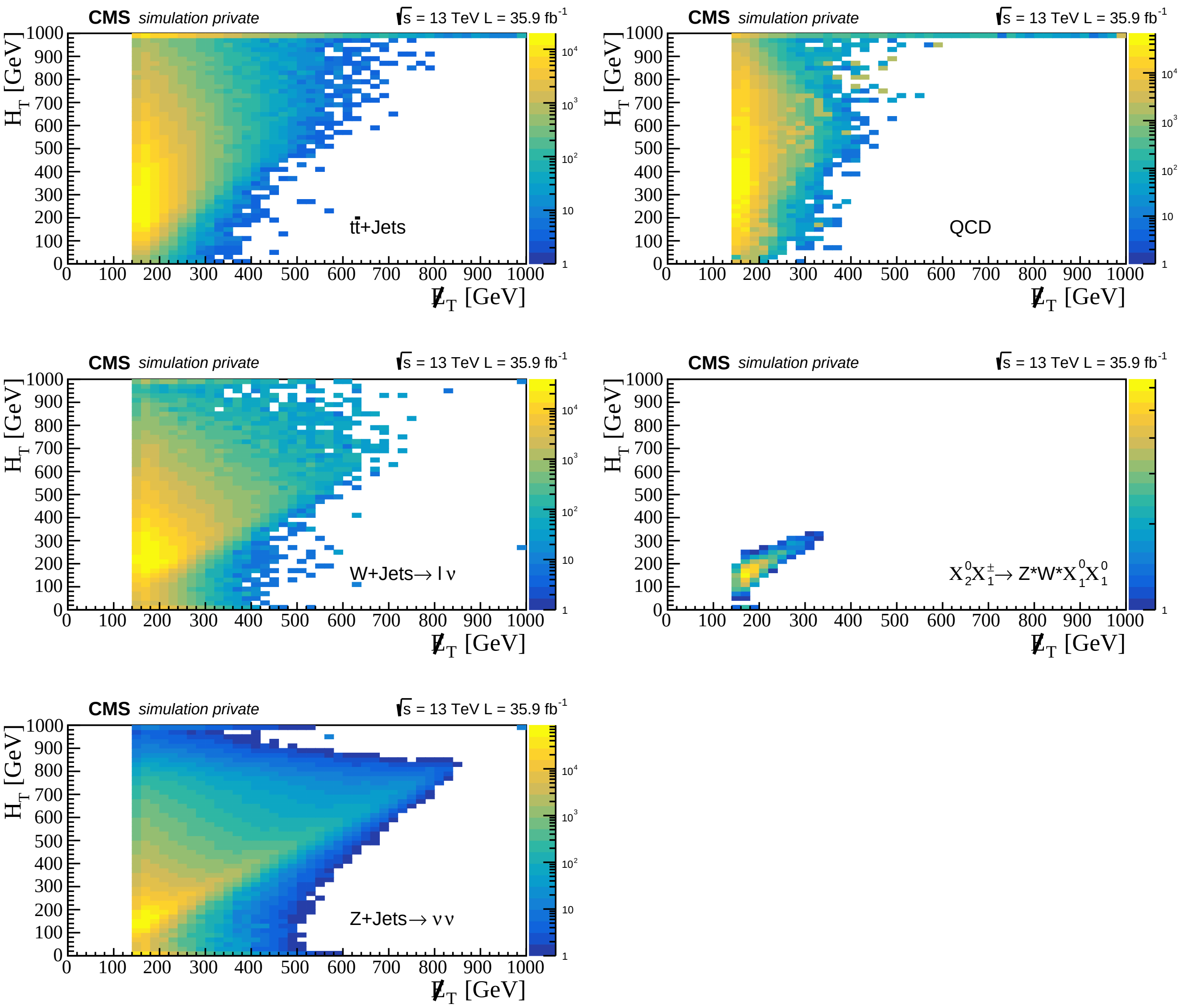

Figure 32: Distributions of the different background types and the signal in the H_T-$\not{E}_T$ plane. A diagonal cut that rejects $H_T > \not{E}_T + 100\,\mathrm{GeV}$ removes most of the QCD background while retaining almost all signal events.

7.6 Reconstruction of Z^* Hadronic Decay Products

This section presents a study that aims to select tracks from Z^* decays in signal events.

Since the most significant background is $Z + \text{Jets} \to \nu\nu + \text{Jets}$, a handle has to be found to discriminate against that process. The only significant difference between $Z + \text{Jets} \to \nu\nu +$ Jets events and signal events are the tracks (and calorimeter deposits) produced by the Z* decay in signal events, which are not present in $Z + \text{Jets} \to \nu\nu + \text{Jets}$ events. The underlying event of $Z + \text{Jets} \to \nu\nu + \text{Jets}$ events and signal events is expected to be very similar. Thus, an optimization of track purity should also serve as an effective way to reduce the $Z + \text{Jets} \to \nu\nu + \text{Jets}$ background, if a high enough purity can be reached.

Particle Flow Efficiency

A first attempt to reconstruct the Z^* decay product was to use particle flow candidates, with the aim of reconstructing the neutral and charged components of the Z*. However, the reconstruction efficiency of particle flow is low for low-energy neutral particles. For this reason, tracks are considered for the main study. The reconstruction efficiency of tracks is much higher than that of neutral particles, at least at low energies. The efficiencies for tracks of Z^* decay products to be reconstructed are shown in Figure 33. However, since the track collection only accounts for charged particles, the neutral component of the Z^* decay is not reconstructed at all.

Purity Optimization

The optimization is carried out in the following track observables:

- p_T : The transverse momentum of the track. Tracks coming from the Z^* decay are expected to have a low transverse momentum;
- η: The pseudo rapidity of the SUSY system is expected to be small, as the production of heavy particles tends to happen in low η regions.
- Relative isolation: Summed p_T in a cone of R=0.3 around the track, normalized to the track p_T (see also Equation 32). Comparatively few tracks are expected from the Z^* decay due to its low energy, leading to a lower isolation;
- Absolute isolation: Summed p_T in a cone of R=0.3 around the track. Using the same argument as above, the energy in a cone around tracks from a Z^* decay is expected to be low;
- $\Delta R^{min}_{Track,Jet}$: The minimal separation in ΔR of the track to any jet in the event. The event selection selects events where the $\not{E}_T$ has a large separation in Φ from the leading jet, which usually comes from initial state radiation. Because of the resulting Lorentz boost

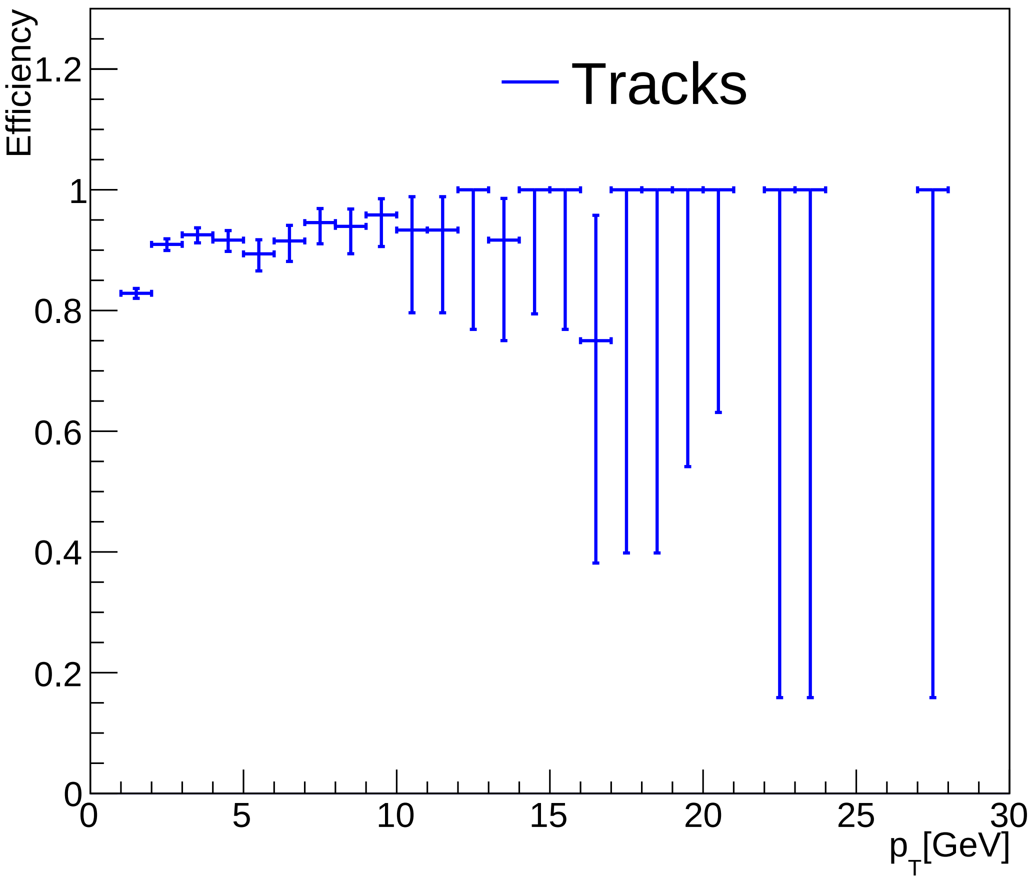

Figure 33: Efficiency of track reconstruction of the Z^* decay products in signal events. The efficiency is computed by a ΔR matching criterion, using Monte Carlo truth information. The efficiencies are given for signal events after the complete event selection defined in Section 7.5. A basic track selection is applied of $p_T > 1$ GeV and $|\eta| < 2$.

of the SUSY system, the Z^* decay products are expected to slightly favor the region opposite the leading Jet.

- ΔR_{min}: ΔR value between the track and the closest neighboring track. Because of the low energy of the off shell Z boson, comparatively few tracks are expected. This observable is an attempt to exploit this feature.

- $\Delta R_{\text{next to minimal}}$: ΔR value between the track and the second-closest neighboring track. As above, the observable is an attempt to use the low multiplicity of Z^* decay products.

- $\Delta\eta_{\mathrm{Track},\Sigma}$, with $\Sigma = \sum_{\mathrm{Tracks}} \vec{p}_{\mathrm{Track}}$: The absolute value of the difference between the track η and the η value of the vectorial sum of all tracks that passed the track selection. This observable is an attempt to use the fact that the decay products of the Z boson are close in η.

The relative isolation of a track A is defined as:

$$\mathrm{Isolation}_A = \frac{\sum_{i \neq A} \mathrm{p}_{\mathrm{T},i} \cdot \Theta\left(0.3 - \Delta\mathrm{R}_{A,i}\right)}{\mathrm{p}_{\mathrm{T},A}} \quad . \tag{32}$$

The step function Θ defines a cone of $\Delta R = 0.3$ around the track A. The sum is normalized to the p_T of the track A. As mentioned previously, comparatively few tracks are produced in the decay of the Z^*. In addition to that, the low boost of the Z^* means that the decay products are not collinear.

The optimization procedure is carried out as follows:

1. Pre-select tracks based on a loose set and track selection criteria;

2. Construct histograms of all track observables given above, using the previous track selection;

3. Calculate the best signal to background track ratio after a set of lower and upper cuts, scanning the range of each histogram of the track observables. Each cut optimum, together with the cuts obtained from previous iterations, defines the current track selection. The measure used in the optimization is the ratio of matched to non-matched tracks

$$\mathrm{p} = \frac{\mathrm{N}^{\mathrm{matched}}_{\mathrm{Tracks}}}{\mathrm{N}^{\text{non-matched}}_{\mathrm{Tracks}}} \quad , \tag{33}$$

   where $\mathrm{N}^{\mathrm{matched}}_{\mathrm{Tracks}}$ is the number of tracks coming from the decay of the $\tilde{\chi}^0_2$ and surviving the current track selection. $\mathrm{N}^{\text{non-matched}}_{\mathrm{Tracks}}$ is the number of tracks passing current the track selection.

Iteration	p_T	$\|\eta\|$	$\Delta R^{min}_{Track,Jet}$	$\Delta R_{next\ to\ minimal}$	$\Delta\Phi_{Track,\ Jet\ 1}$	$N^{matched}_{Tracks}$	$N^{non\text{-}matched}_{Tracks}$
baseline	$[1,\infty]$	$[0,2]$	-	-	-	188	3330
step 1	$[2,20]$	$[0,2]$	$[0.4,\infty]$	$[0.05,\infty]$	-	94	581
step 2	$[2,20]$	$[0,2]$	$[0.4,\infty]$	$[0.05,\infty]$	$[1,\infty]$	72	266
step 3	$[4,20]$	$[0,2]$	$[0.4,\infty]$	$[0.05,\infty]$	$[1,\infty]$	26	51
final	$[4,20]$	$[0,2]$	$[0.4,\infty]$	$[0.05,\infty]$	$[2.6,\infty]$	10	11

Table 8: Cutflow of the track purity optimization. The rows are the optimization iterations, the columns the track observables that were cut on. The colored fields are those that changed with respect to the previous iteration. $N^{matched}_{Tracks}$ refers to tracks matched in ΔR to truth level Z^* charged decay products. $N^{non\text{-}matched}_{Tracks}$ refers to the complement of $N^{matched}_{Tracks}$.

4. Select a cut candidate from the set of track observables above to incorporate into the next track selection iteration. There are two criteria for this choice:
   - The ratio of matched to non-matched tracks after the cut is implemented;
   - The relative amount of signal that is cut away; It is desirable to not perform a cut that reduces the signal tracks by, e.g. 90%, as this reduces the sensitivity of the analysis. When a best cut with respect to the ratio of matched to non-matched tracks is found, it is better to implement weaker versions of the cut first and approach the best cut in multiple steps, instead of immediately applying the best cut. Using this approach improves the chance to actually find the maximum sensitivity.
5. Visually check distributions after applying these cuts on the most significant observables to avoid the selection of statistical fluctuations in case of low statistics;
6. Include the cut in the track selection, and repeat procedure starting at point 2.

The optimization was done using the events selected according to Section 7.5. It is performed in 5 steps that are summarized in Table 8. The result can be found in Figures 34 to 41. Each step is displayed in two consecutive Figures, meaning that the baseline selection is given in Figures 34 and 35, the first optimization step in Figures 36 and 37 and so on.

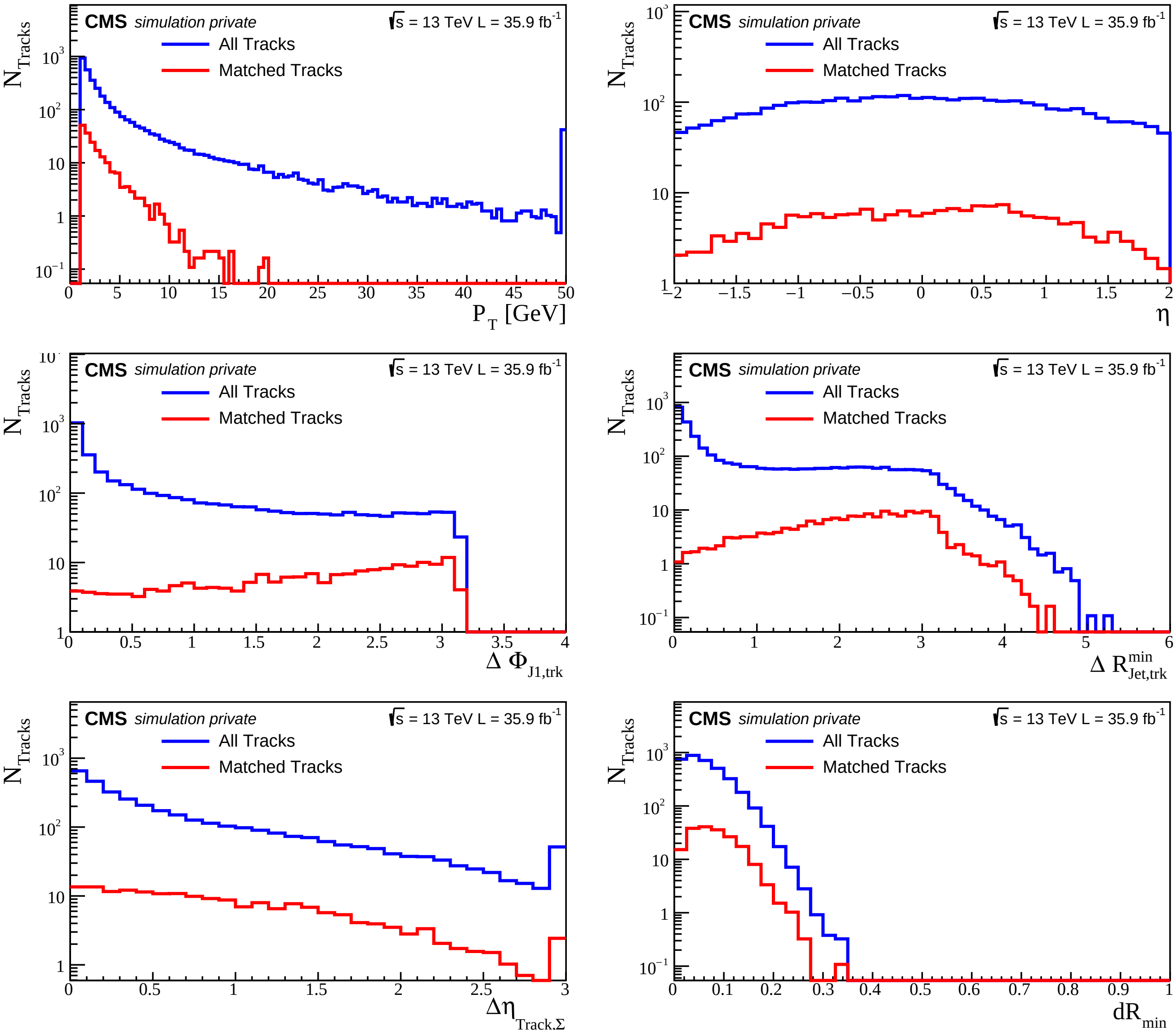

Figure 34: First six track observables of the track purity optimization in signal events. In all histograms depicted here, the event selection defined in Section 7.5 is applied. The red histograms contain exclusively tracks matched to Z^* decay products in the simulation, the blue histograms includes all tracks in the event, including the matched tracks. The track observables shown are p_T (top left), η (top right), $\Delta\Phi_{\mathrm{J1,\,Track}}$ (middle left), $\Delta R^{\mathrm{min}}_{\mathrm{Jet,\,Track}}$(middle right), $\Delta\eta_{\mathrm{Track},\Sigma}$(bottom left), ΔR_{min} (bottom right). The baseline track selection of $p_T > 1$ GeV and $|\eta| \in [0,2]$ is applied (see Table 8).

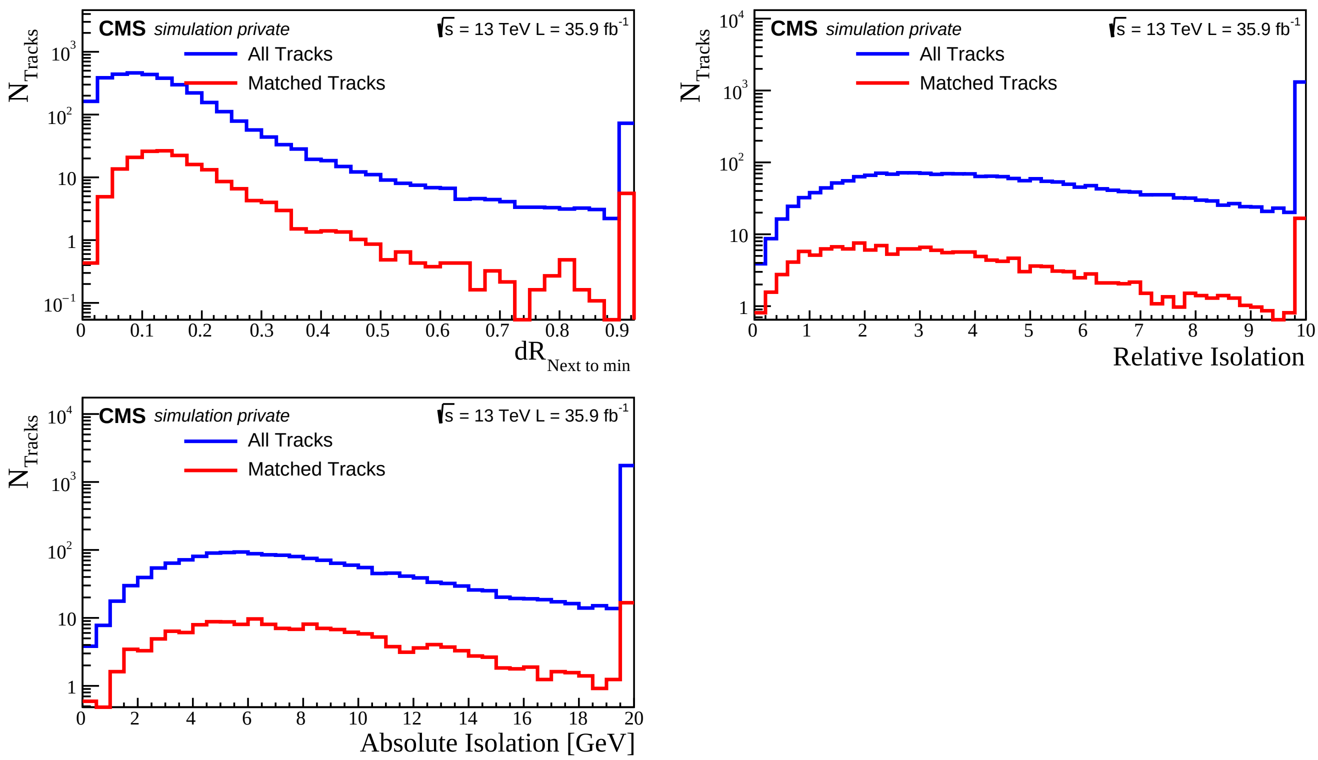

Figure 35: Remaining five track observables of the track purity optimization in signal events. In all histograms depicted here, the event selection defined in Section 7.5 is applied. The red histograms contain exclusively tracks matched to Z^* decay products in the simulation, the blue histograms includes all tracks in the event, including the matched tracks. The track observables shown are $\Delta R_{\text{next to minimal}}$ (top left), relative Isolation (top right), absolute isolation (bottom). The baseline track selection of $p_T >$ 1 GeV and $|\eta| \in [0,2]$ is applied (see Table 8).

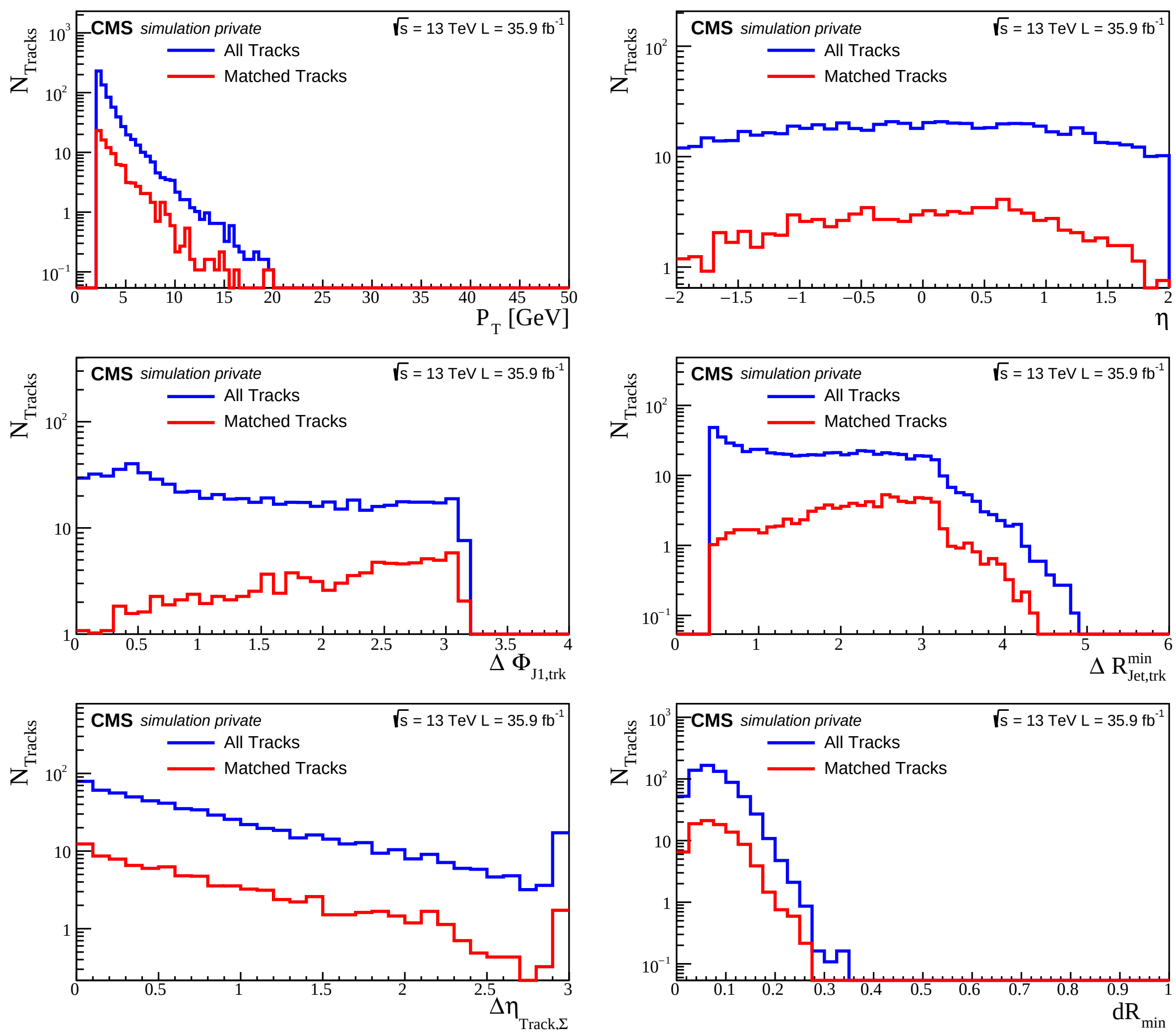

Figure 36: First six track observables of the track purity optimization in signal events. In all histograms depicted here, the event selection defined in Section 7.5 is applied. The red histograms contain exclusively tracks matched to Z^* decay products in the simulation, the blue histograms includes all tracks in the event, including the matched tracks. The selection is modified with respect to the baseline selection in the observables p_T , $\Delta R_{\text{Track,Jet 1}}$, $\min(\Delta R_{\text{Track,Jet}})$ and $\Delta R_{\text{next to minimal}}$ (see Table 8, step 1). The track observables shown are p_T (top left), η (top right), $\Delta\Phi_{\text{J1, Track}}$ (middle left), $\Delta R^{\text{min}}_{\text{Jet, Track}}$(middle right), $\Delta\eta_{\text{Track},\Sigma}$(bottom left), ΔR_{min} (bottom right).

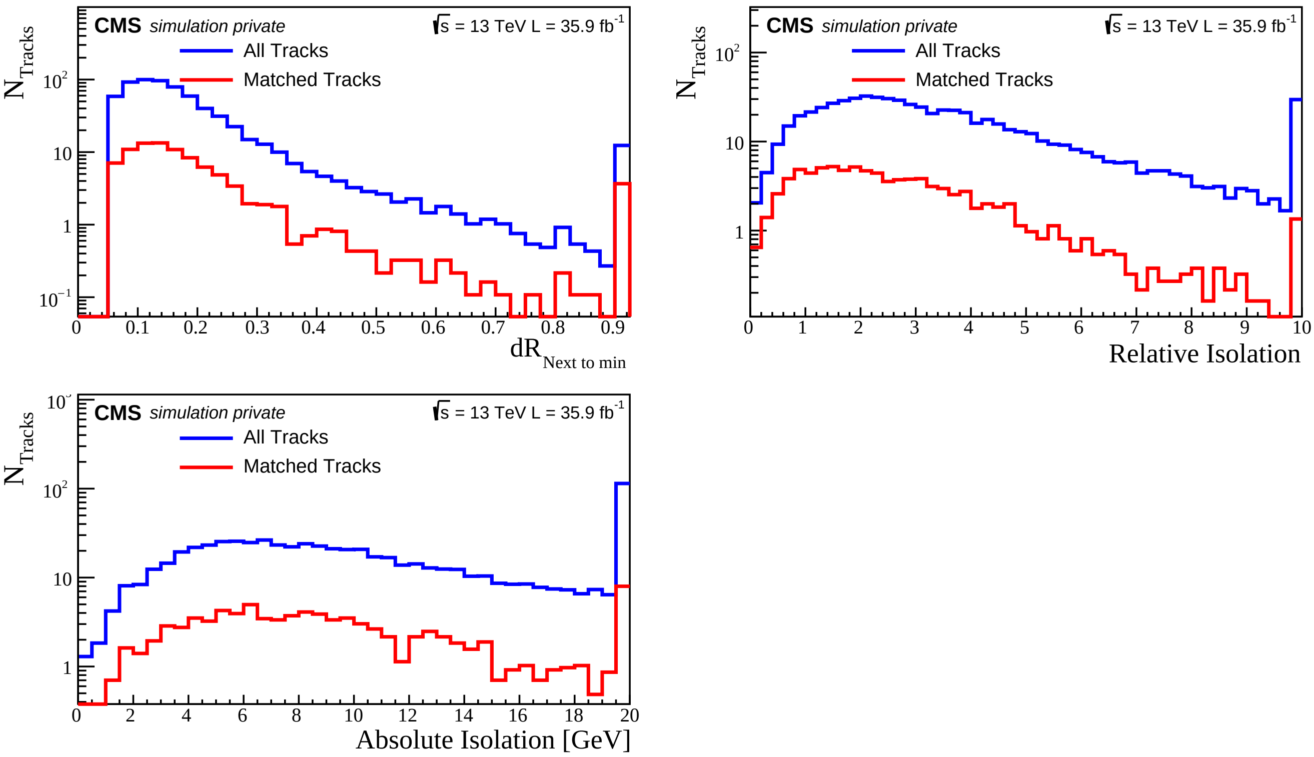

Figure 37: Remaining five track observables after the first step of the track purity optimization in signal events. In all histograms depicted here, the event selection defined in Section 7.5 is applied. The red histograms contain exclusively tracks matched to Z^* decay products in the simulation, the blue histograms includes all tracks in the event, including the matched tracks. This first step modifies the baseline selection in the observables p_T , $\Delta R_{\text{Track,Jet 1}}$, $\min(\Delta R_{\text{Track,Jet}})$ and $\Delta R_{\text{next to minimal}}$ (see Table 8, step 1). The track observables shown are $\Delta R_{\text{next to minimal}}$ (top left), relative Isolation (top right), absolute isolation (bottom).

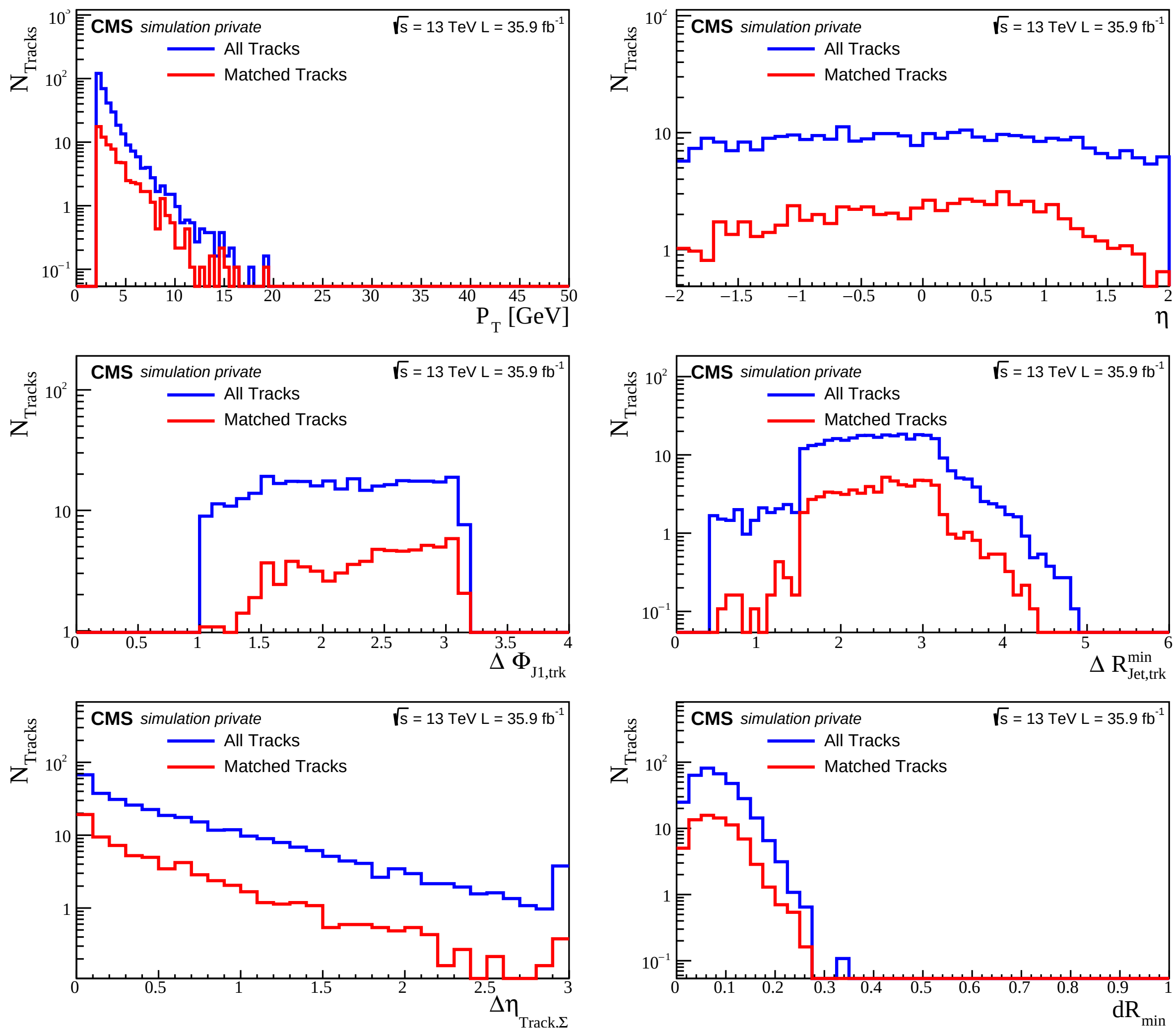

Figure 38: Second step of the track purity optimization (see Table 8). In all histograms depicted here, the event selection defined in Section 7.5 is applied. The red histograms contain exclusively tracks matched to Z^* decay products in the simulation, the blue histograms includes all tracks in the event, including the matched tracks. The constraint $\Delta\Phi_{\text{Track, Jet 1}} > 1$ is added to the previous selection. The track observables shown are p_T (top left), η (top right), $\Delta\Phi_{\text{J1, Track}}$ (middle left), $\Delta R^{\text{min}}_{\text{Jet, Track}}$(middle right), $\Delta\eta_{\text{Track},\Sigma}$(bottom left), ΔR_{min} (bottom right).

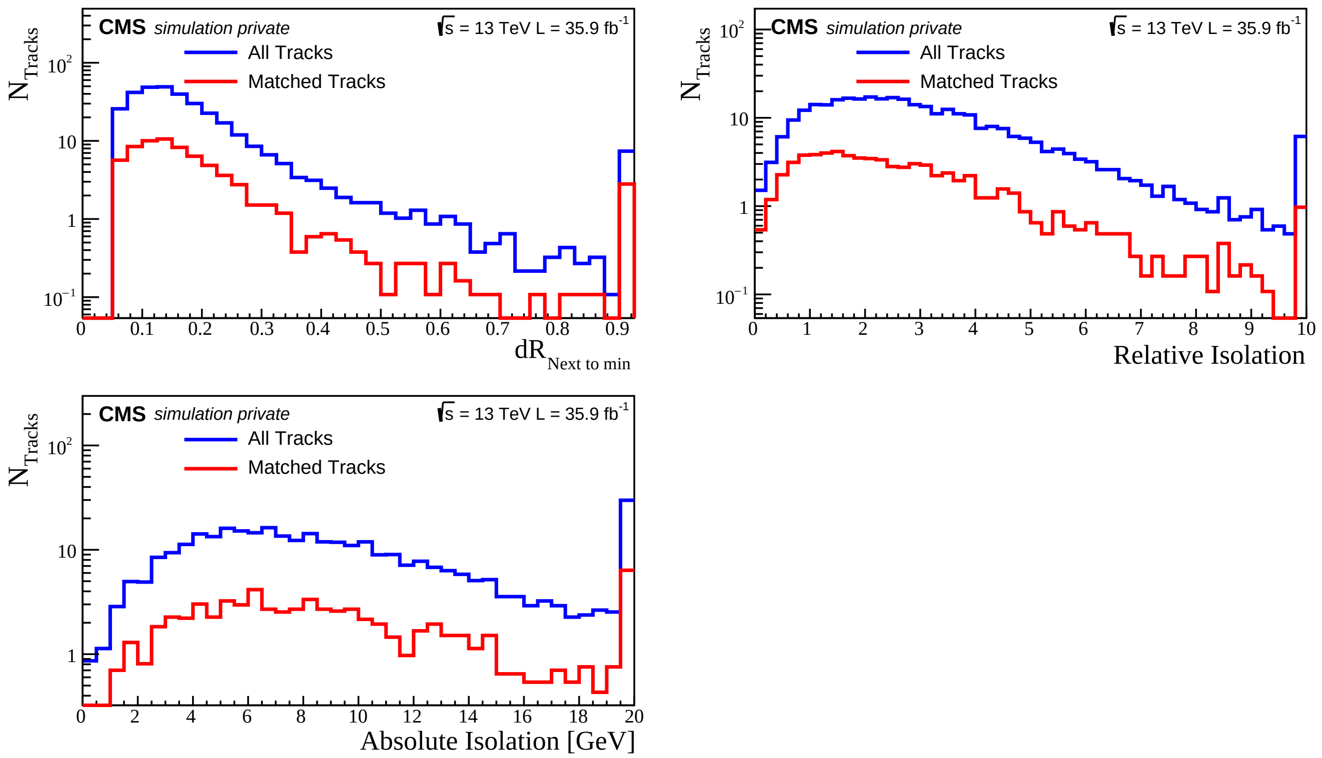

Figure 39: Second step of the track purity optimization (see Table 8). In all histograms depicted here, the event selection defined in Section 7.5 is applied. The red histograms contain exclusively tracks matched to Z^* decay products in the simulation, the blue histograms includes all tracks in the event, including the matched tracks. The constraint $\Delta\Phi_{\text{Track, Jet 1}} > 1$ is added to the previous selection. The track observables shown are $\Delta R_{\text{next to minimal}}$ (top left), relative Isolation (top right), absolute isolation (bottom).

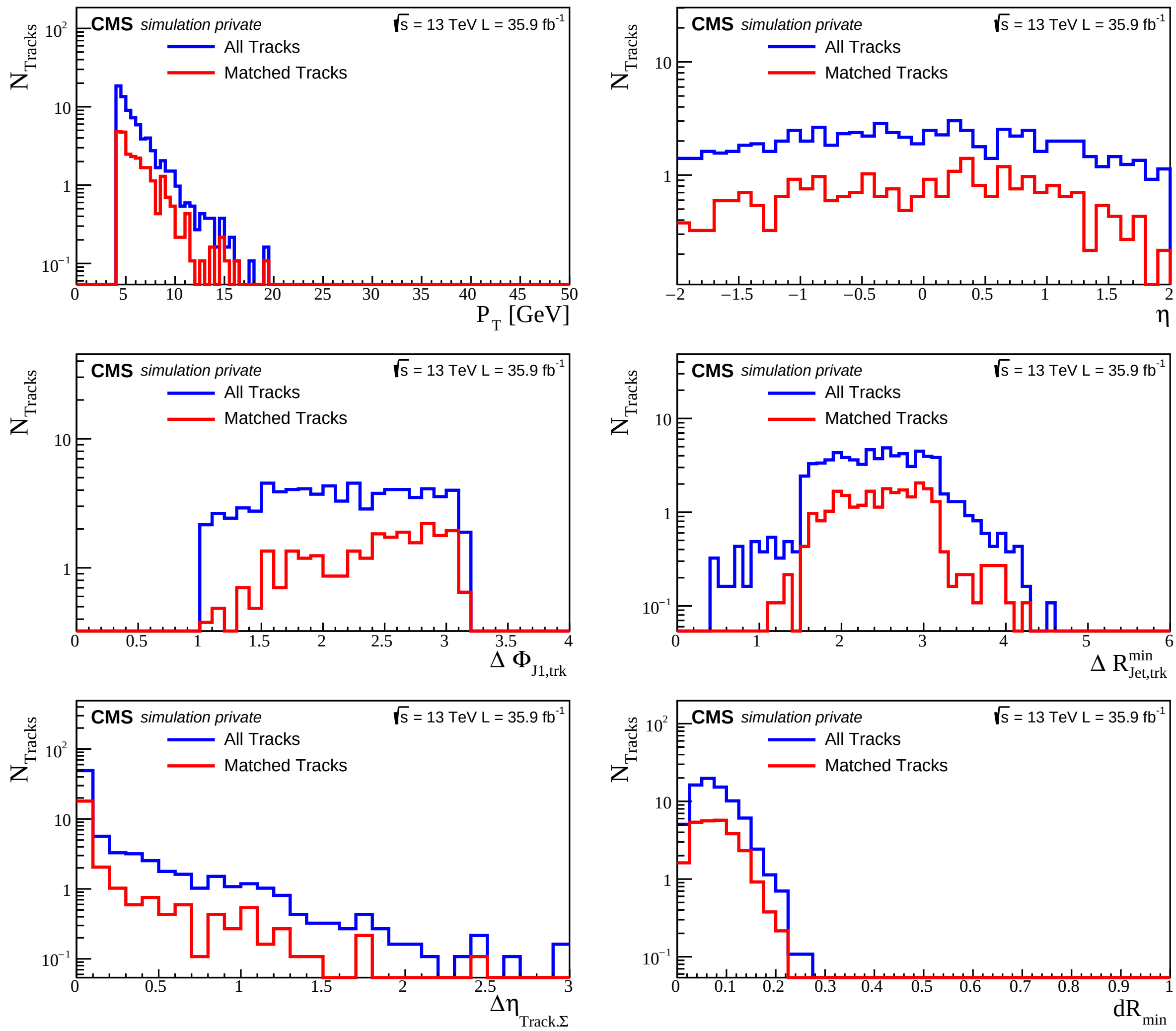

Figure 40: Third step of the track purity optimization (see Table 8. In all histograms depicted here, the event selection defined in Section 7.5 is applied. The red histograms contain exclusively tracks matched to Z^* decay products in the simulation, the blue histograms includes all tracks in the event, including the matched tracks. The constraint on the track p_T is tightened with respect to the second optimization step to $p_T > 4\,\mathrm{GeV}$. The track observables shown are p_T (top left), η (top right), $\Delta\Phi_{J1,\,\mathrm{Track}}$ (middle left), $\Delta R^{\mathrm{min}}_{\mathrm{Jet,\,Track}}$(middle right), $\Delta\eta_{\mathrm{Track},\Sigma}$(bottom left), ΔR_{min} (bottom right).

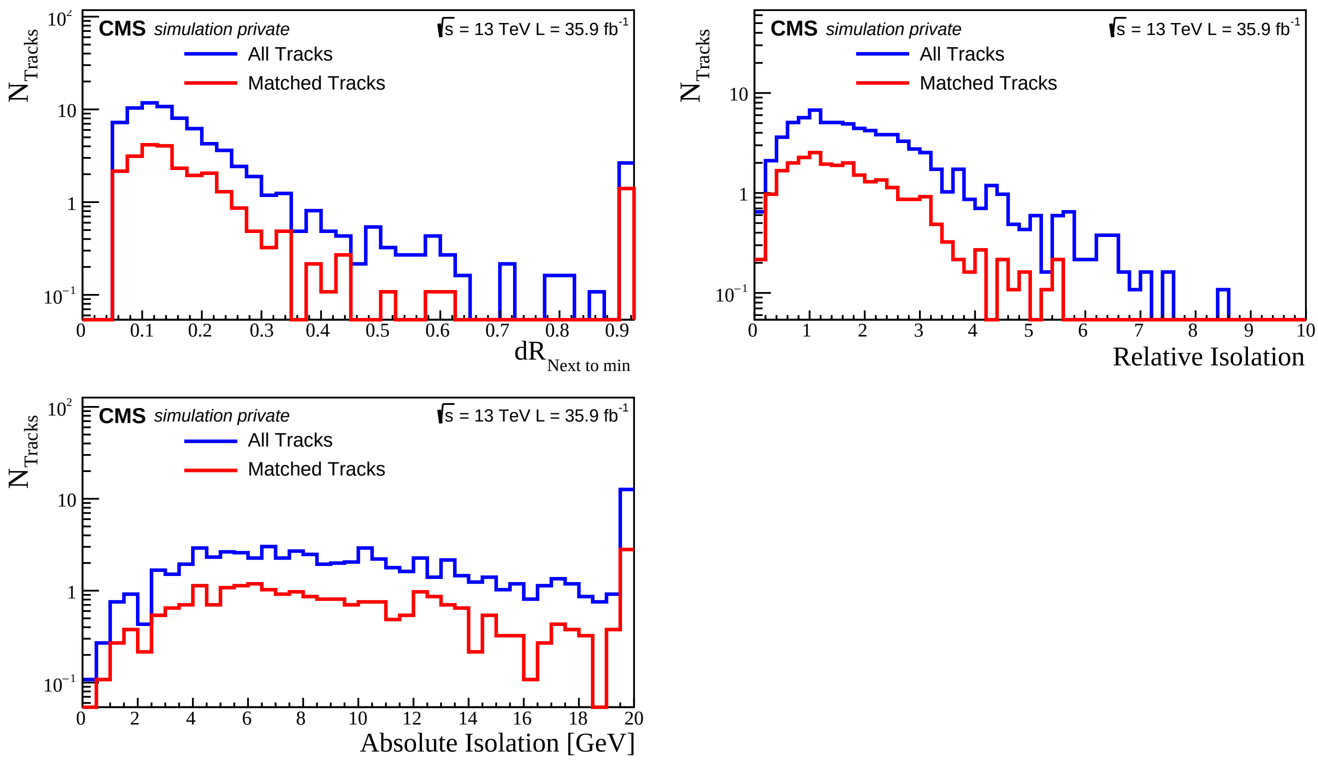

Figure 41: Third step of the track purity optimization (see Table 8). In all histograms depicted here, the event selection defined in Section 7.5 is applied. The red histograms contain exclusively tracks matched to Z^* decay products in the simulation, the blue histograms includes all tracks in the event, including the matched tracks. The constraint on the track p_T is tightened with respect to the second optimization step to $p_T > 4\,\mathrm{GeV}$. The track observables shown are $\Delta R_{\text{next to minimal}}$ (top left), relative Isolation (top right), absolute isolation (bottom).

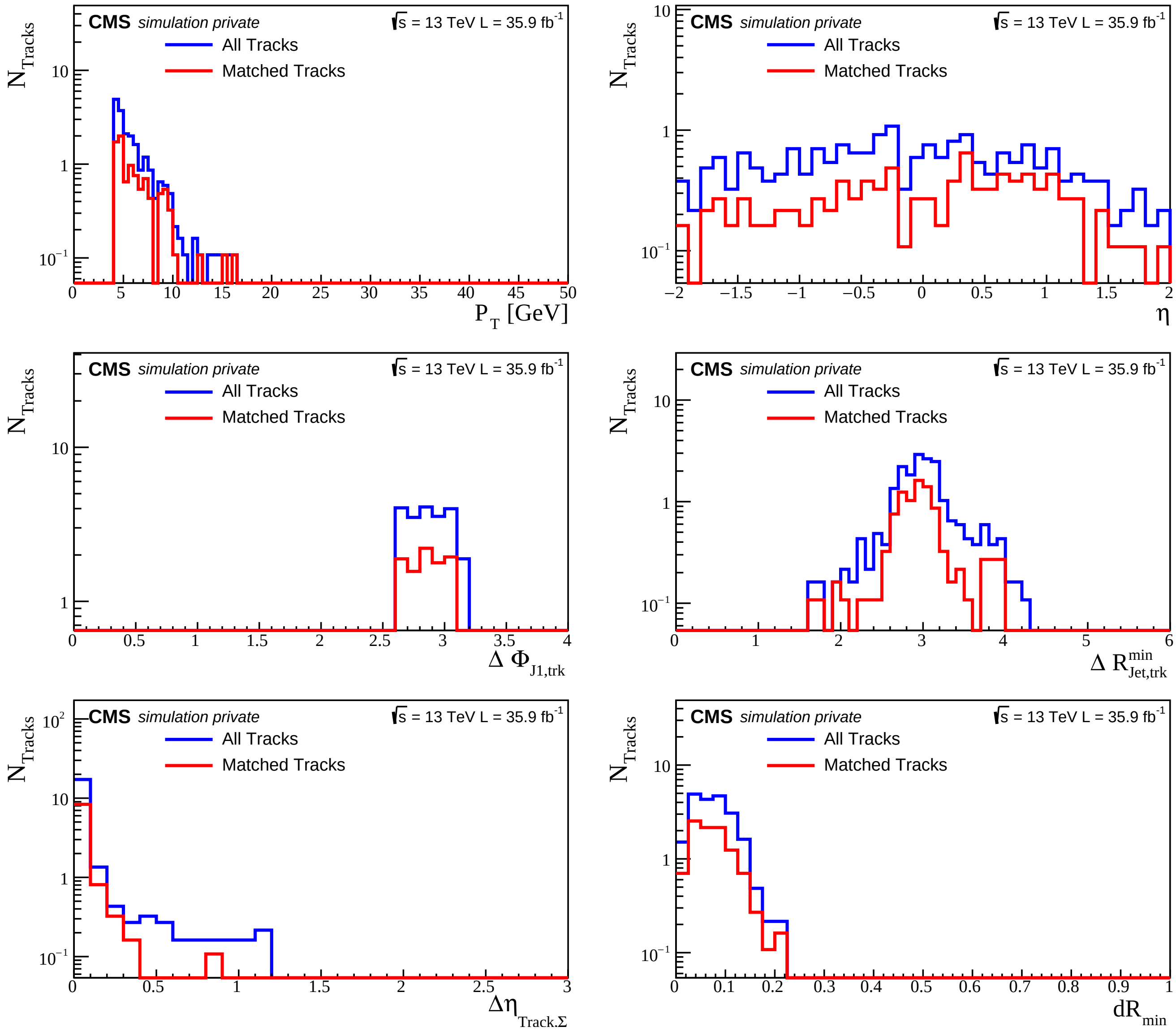

Figure 42: Fourth and final step of the track purity optimization (see Table 8). In all histograms depicted here, the event selection defined in Section 7.5 is applied. The red histograms contain exclusively tracks matched to Z^* decay products in the simulation, the blue histograms includes all tracks in the event, including the matched tracks. The constraint on $\Delta\Phi_{\text{Track, Jet 1}}$ is tightened with respect to the previous optimization steps to $\Delta\Phi_{\text{Track, Jet 1}} > 2.6$. The track observables shown are p_T (top left), η (top right), $\Delta\Phi_{\text{J1, Track}}$ (middle left), $\Delta R^{\text{min}}_{\text{Jet, Track}}$(middle right), $\Delta\eta_{\text{Track},\Sigma}$(bottom left), ΔR_{min} (bottom right).

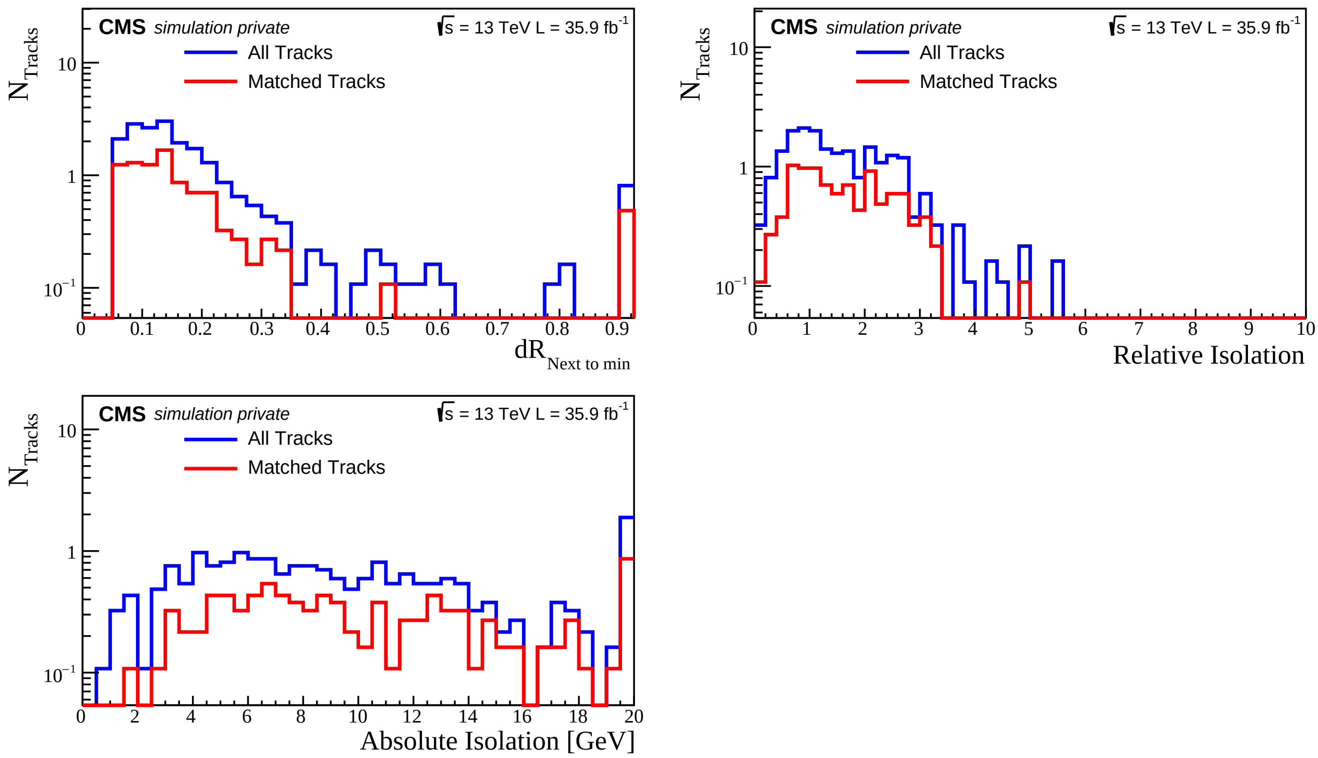

Figure 43: Fourth and final step of the track purity optimization (see Table 8). In all histograms depicted here, the event selection defined in Section 7.5 is applied. The red histograms contain exclusively tracks matched to Z^* decay products in the simulation, the blue histograms includes all tracks in the event, including the matched tracks. The constraint on $\Delta\Phi_{\text{Track, Jet 1}}$ is tightened with respect to the previous optimization steps to $\Delta\Phi_{\text{Track, Jet 1}} > 2.6$. The track observables shown are $\Delta R_{\text{next to minimal}}$ (top left), relative Isolation (top right), absolute isolation (bottom).

The best signal to background ratio, i.e. purity, that was reached is approximately $\frac{N_{\text{matched tracks}}}{N_{\text{non-matched tracks}}} \approx 1$, corresponding to approximately 6% signal acceptance and 99.5% background rejection. No further improvement could be achieved, primarily due to the lack of statistics with this event selection. Further attempts to optimize using this method would increasingly likely result in over optimization and may fall short due to statistical fluctuations.

This method only tries to optimize the track purity inside signal events. When trying to find the signal however, it is ultimately necessary to separate the signal against the Standard Model background. While an increased purity of matched tracks should lead to a separation from the Standard Model background, the preferred method is to directly optimize the signal against the background on an event-level basis. Such an optimization is attempted in the next section, using the same set of track observables, as this study has shown that the set of track observables that were chosen can work to isolate the Z^* decay products.

7.7 Inclusion of Track Based Event Observables

The baseline selection defined in Section 7.5 does not use any track-level information. In this section, further optimization of the signal significance is studied by using track-level information (e.g. track p_T and η) to define event-level quantities and finding optimal cuts on them. A simultaneous optimization of a track selection and these event-level quantities with respect to the signal significance is performed.
The constructed event-level track quantities chosen in this work are:

- N_{Tracks}: The number of tracks in an event that have passed the track selection;
- m_{All}: The invariant mass computed from all tracks in an event that have passed the track selection.

The track observables are the same as used in the track purity optimization in Section 7.6, namely:

- p_T
- η
- Relative isolation
- Absolute isolation
- $\Delta R^{min}_{Track,Jet}$: The minimal separation in ΔR of the track to any jet in the event.
- $\Delta\Phi_{Track,Jet1}$: Jet 1 is the leading jet in the event.
- ΔR_{min}:ΔR value between the track and the closes neighboring track.
- $\Delta R_{next\ to\ minimal}$:$\Delta R$ value between the track and the second-closest neighboring track.
- $\Delta\eta_{Track,\Sigma}$: The absolute value of the difference in pseudorapidity between the track and the vectorial sum of all tracks that passed the track selection.

The optimization is done in the following way (see also Table 9): For each track observable in the list above, a set of lower and upper thresholds is defined that spans the spectrum of values in that track observable. In this work, the thresholds are defined by the bin edges of histograms that store the distributions of each observable. For example, the p_T has a corresponding histogram in the range [0,50] in steps of 1 GeV. The set of lower and upper thresholds are chosen to cut away a linearly increasing number of bins. The sets of thresholds correspond to the allowed p_T ranges [1,50],[2,50],...,[50,50] for the lower thresholds, and [0,49],[0,48],...[0,0] for the upper thresholds. Note that in all of the track observable histograms used here, the last bin is an overflow bin.

For each of the cuts in the set, the event-level track observable distributions, which are the track multiplicity N_{Tracks} and the invariant mass of all tracks that pass the track selection, M_{All}

Track observable →	p_T	$\lvert\eta\rvert$	...
Optimization step ↓	max $\Sigma(N_{\text{Tracks}},\ \text{M}_{\text{all}})$ ↓	max $\Sigma(N_{\text{Tracks}},\ \text{M}_{\text{all}})$ ↓	...
1: current selection is applied on →	A_1^1	A_2^1	...
2: current selection $+\max_\Sigma(A_i^1)$ is applied on →	A_1^2 $\left(\Sigma(A_1^2) > \max_\Sigma(A_1^1, A_2^1, ...)\right)$	A_2^2 $(\Sigma(A_2^2) > \max_\Sigma(A_1^1, A_2^1, ...))$	...
⋮	...	...	...

Table 9: Schematic of the event optimization process. Σ refers to the significance, the A_j^i are the cuts on the jth track observable in the ith iteration of the optimization that lead to the best significance in N_{Tracks} or M_{all}. For each track observable, a set of cuts is defined that spans the whole spectrum of expected values. For each cut and each track observable, the cut on the track observable is temporarily included in the current track selection and an optimal cut on the event-level track observables N_{Tracks} and M_{all} is determined. The cut on the track observable that leads to the best cut on the event-level observable is permanently added to the track selection for the subsequent iterations. The cut on the event-level observable is only incorporated permanently at the end of the optimization. The process is repeated until no further optimization is possible.

are plotted while also respecting the previous track selection. In the resulting distributions of event-level track observables, an optimal cut with respect to the signal significance Σ, defined as

$$\Sigma = \frac{\text{N}_{\text{Signal}}}{\sqrt{\text{N}_{\text{Signal}} + \text{N}_{\text{Background}}}} \quad , \tag{34}$$

is found by introducing lower and upper thresholds on N_{Tracks} and M_{all} in the same way as for the track observables, using the bins of the corresponding histograms as the cut thresholds. The cut on the track observable that leads to a best cut on one of the event-level observables is added to the track selection, and the next iteration begins. This process is repeated until either the significance converges, the simulation statistics disallow further cuts, or the signal acceptance falls below a given threshold, e.g. when no events are expected for a target luminosity. The event selection optimization in N_{Tracks} and M_{all} is given in Figures 44 to 49. The best signal significance that was reached is $\Sigma = 0.1116$ with a cut of $\text{M}_{\text{all}} > 7\,\text{GeV}$, slightly improving on the value of $\Sigma = 0.1027$ present before the inclusion of track information. Table 10 shows the steps of the optimization, including the final track selection.

Figures 50, 51, and 52 show the final event selection. The optimization was unable to notably increase the signal significance. This is due to the fact that the signal producs a signature that is significantly contaminated by the underlying event, that is further diminished by the large masses of the SUSY particles in the specific model that was investigated here. The large masses result in both a lower cross section and a smaller boost of the SUSY system. The small boost results both in lower energies as well as an isotropic distribution of the final state, making it

Optimization step	p_T	$\|\eta\|$	$\Delta R^{min}_{Jet, Track}$	ΔR_{min}
baseline	[0.5,20]	[0,2.4]	[0.4,∞]	-
step 1	[0.5,20]	[0,2.4]	[0.4,∞]	[0.2, ∞]
final	[0.5,20]	[0,2.4]	[0.4,3]	[0.2, ∞]

Table 10: Cutflow of the track selection optimization. The rows are the optimization iterations, the columns the track observables that were added to the track selection. The colored fields are those that changed with respect to the previous iteration.

almost indistinguishable from the underlying event, as well as the background.

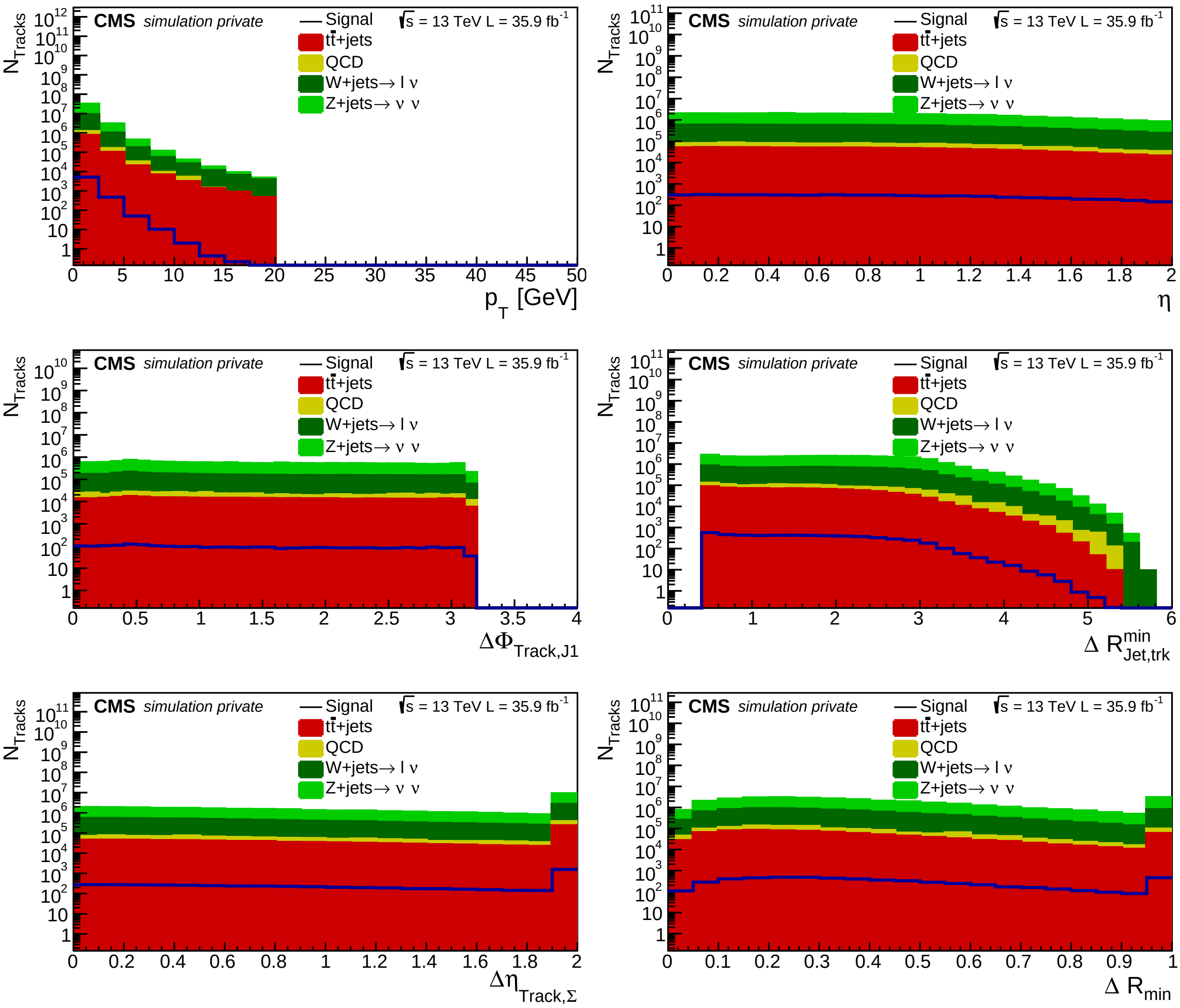

Figure 44: First six track observables of the track selection optimization. A baseline selection of $p_T \in [0.5\,\mathrm{GeV}, 20\,\mathrm{GeV}]$, $|\eta|<2.4$, and $\Delta R^{min}_{\text{Jet, Track}} > 0.4$ is applied (see Table 10). The track observables shown are p_T (top left), $|\eta|$ (top right), $\Delta\Phi_{\text{Track,J1}}$ (middle left), $\Delta R^{min}_{\text{Jet, Track}}$(middle right), $\Delta\eta_{\text{Track},\Sigma}$(bottom left), and ΔR_{min} (bottom right).

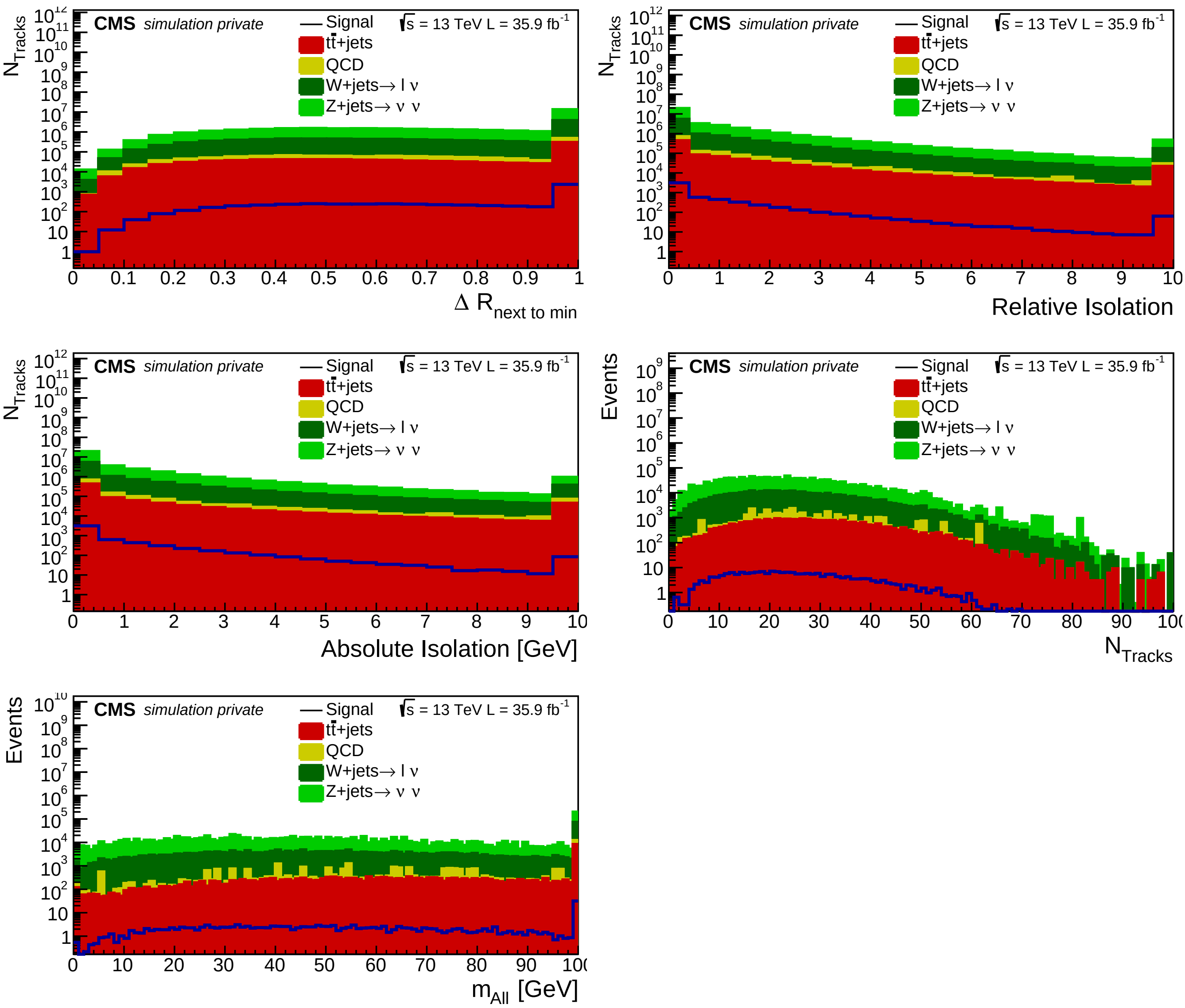

Figure 45: Last three track observables of the track selection optimization and the two event-level quantities with the current track selection. A baseline selection of $p_T \in [0.5\,\mathrm{GeV}, 20\,\mathrm{GeV}]$, $|\eta|$<2.4, and $\Delta R^{\mathrm{min}}_{\mathrm{Jet,\,Track}} > 0.4$ is applied (see Table 10). The track observables shown are $\Delta R_{\mathrm{next\ to\ min}}$ (top left), relative Isolation (top right), absolute Isolation (middle left), and the event-level quantities N_{Tracks} (middle right), and m_{All} (bottom).

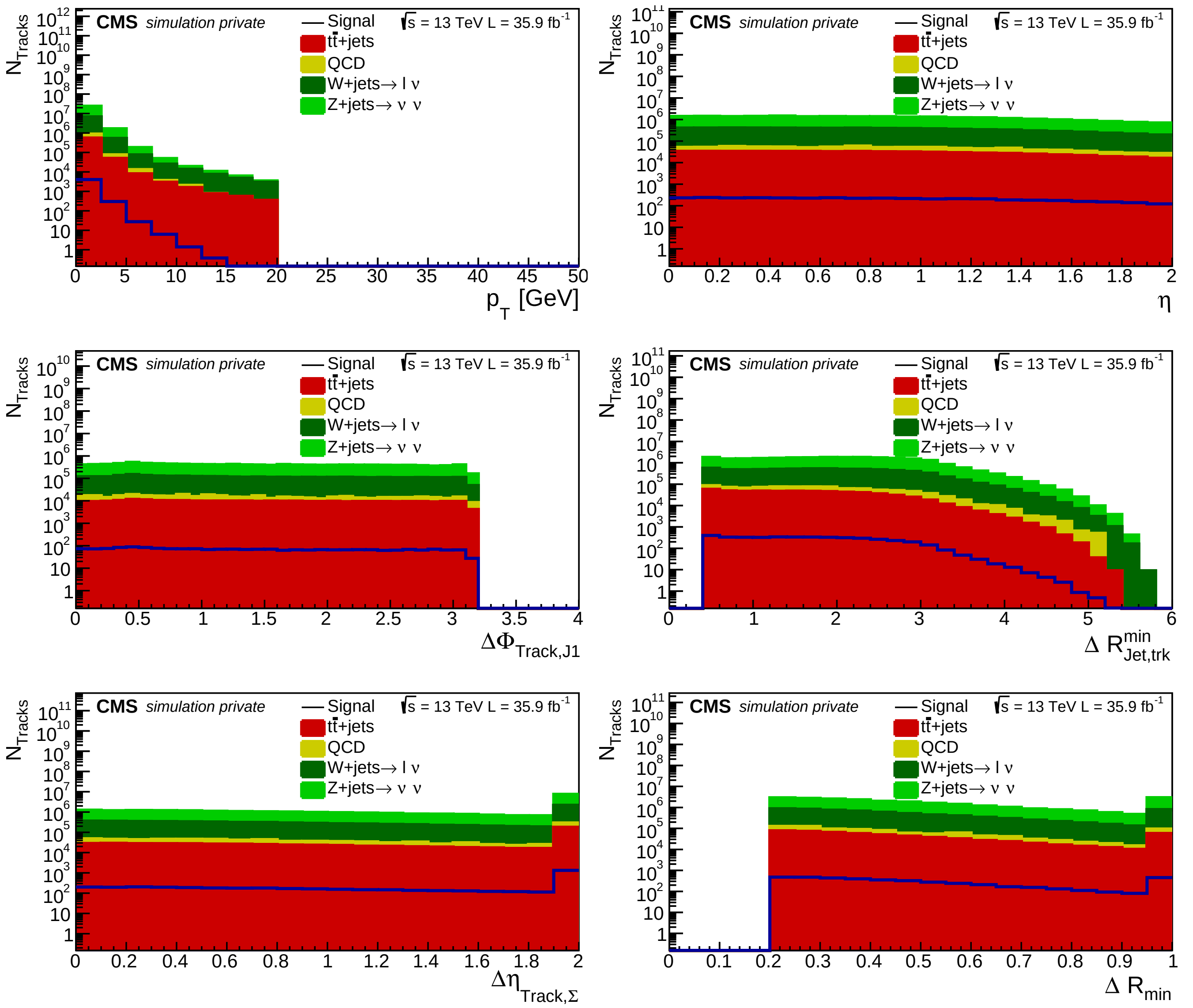

Figure 46: First six track observables of the track selection optimization. A cut of $\Delta R_{\text{min}} < 0.2$ is applied in addition to the baseline selection (see Table 10). The track observables shown are p_T (top left), $|\eta|$ (top right), $\Delta\Phi_{\text{Track,J1}}$ (middle left), $\Delta R^{\text{min}}_{\text{Jet, Track}}$(middle right), $\Delta\eta_{\text{Track},\Sigma}$(bottom left), and ΔR_{min} (bottom right).

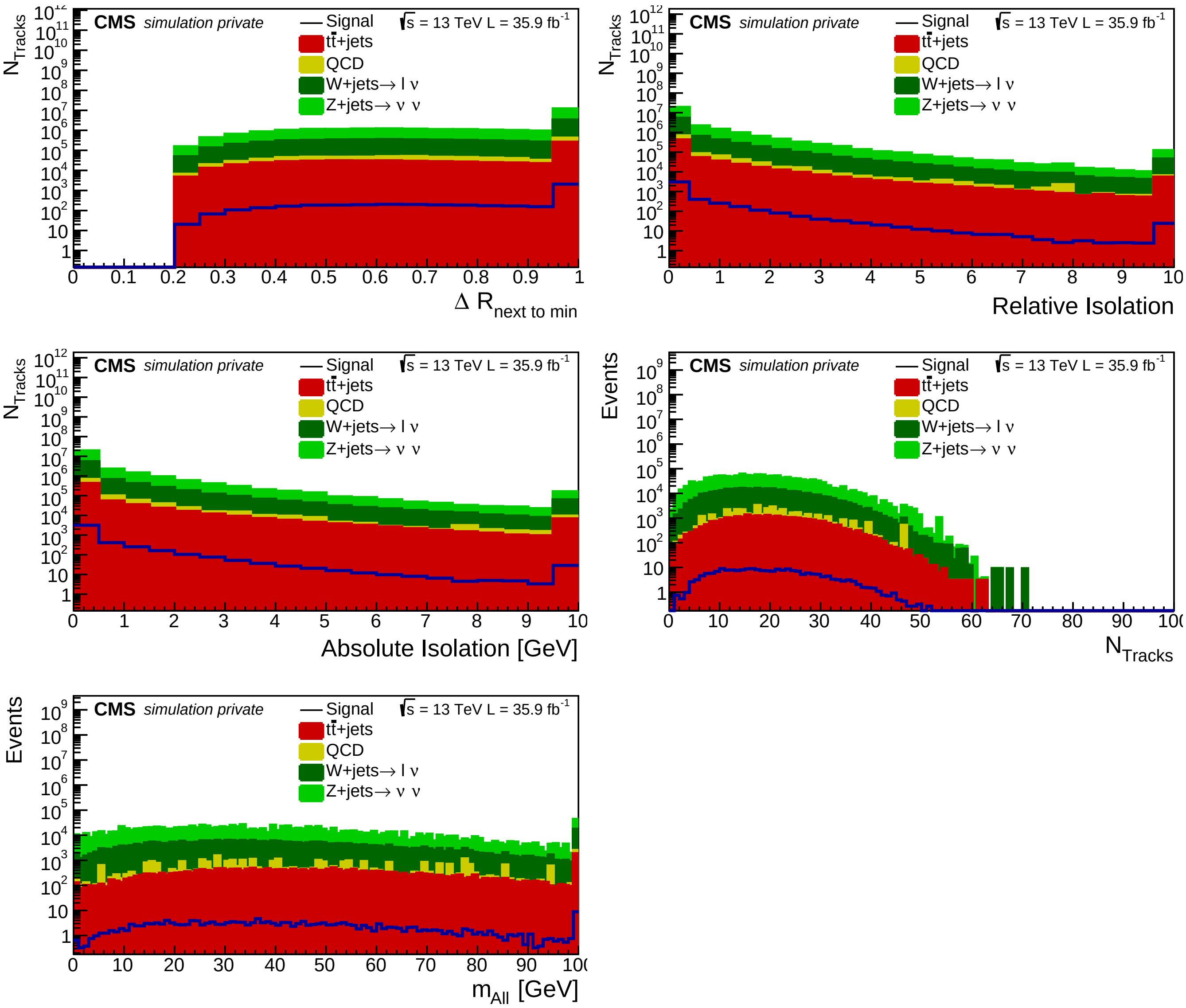

Figure 47: Last three track observables of the track selection optimization and the two event-level quantities with the current track selection. A cut of $\Delta R_{min} < 0.2$ is applied in addition to the baseline selection (see Table 10). The track observables shown are $\Delta R_{next\ to\ min}$ (top left), relative Isolation (top right), absolute Isolation (middle left), and the event-level quantities N_{Tracks} (middle right), and m_{All} (bottom).

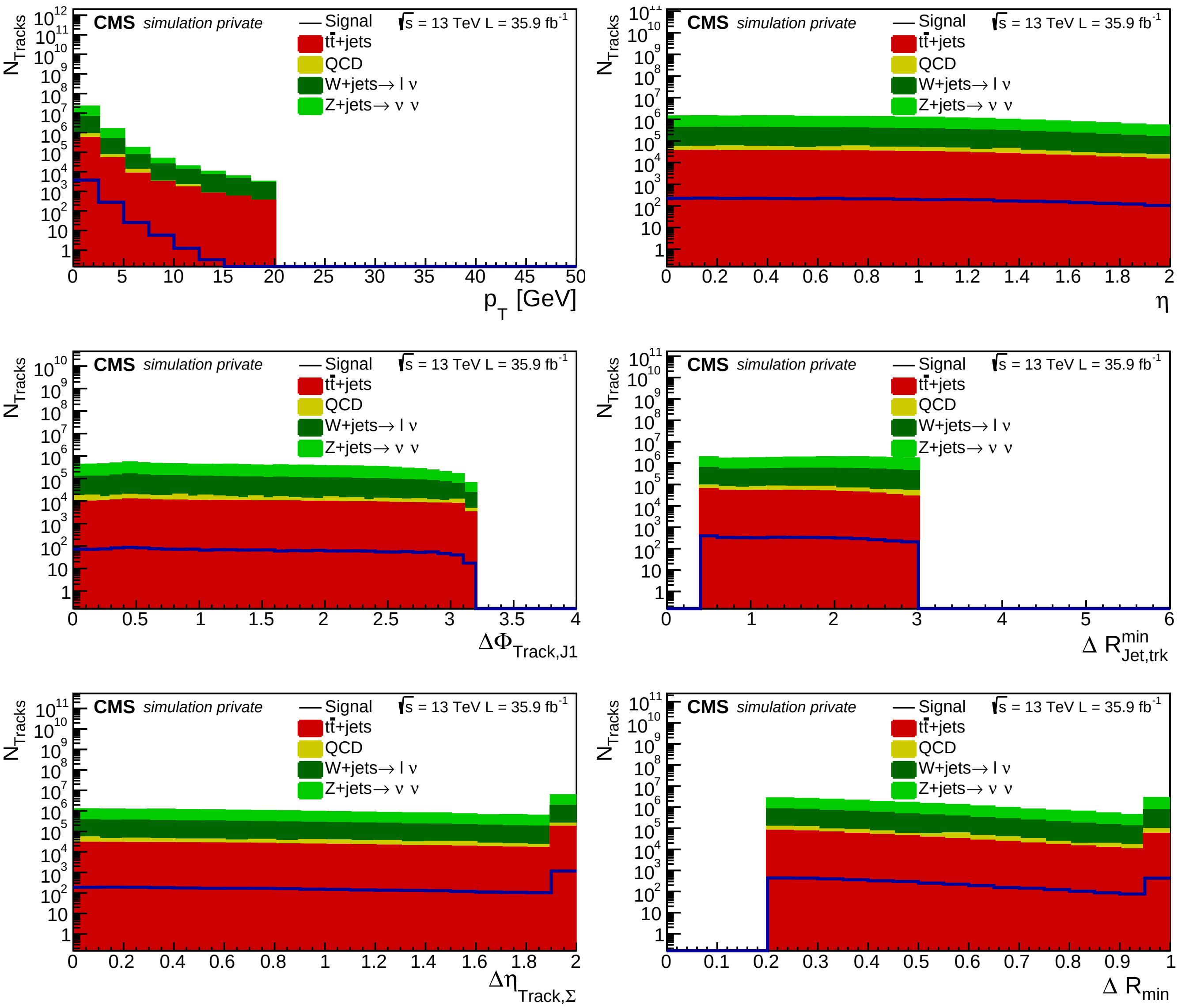

Figure 48: First six track observables of the track selection optimization. The requirement on $\Delta R^{min}_{Jet,\,Track}$ is tightened to $\Delta R^{min}_{Jet,\,Track} \in [0.4, 3]$ (see Table 10). The track observables shown are p_T (top left), $|\eta|$ (top right), $\Delta\Phi_{Track,J1}$ (middle left), $\Delta R^{min}_{Jet,\,Track}$ (middle right), $\Delta\eta_{Track,\Sigma}$ (bottom left), and ΔR_{min} (bottom right).

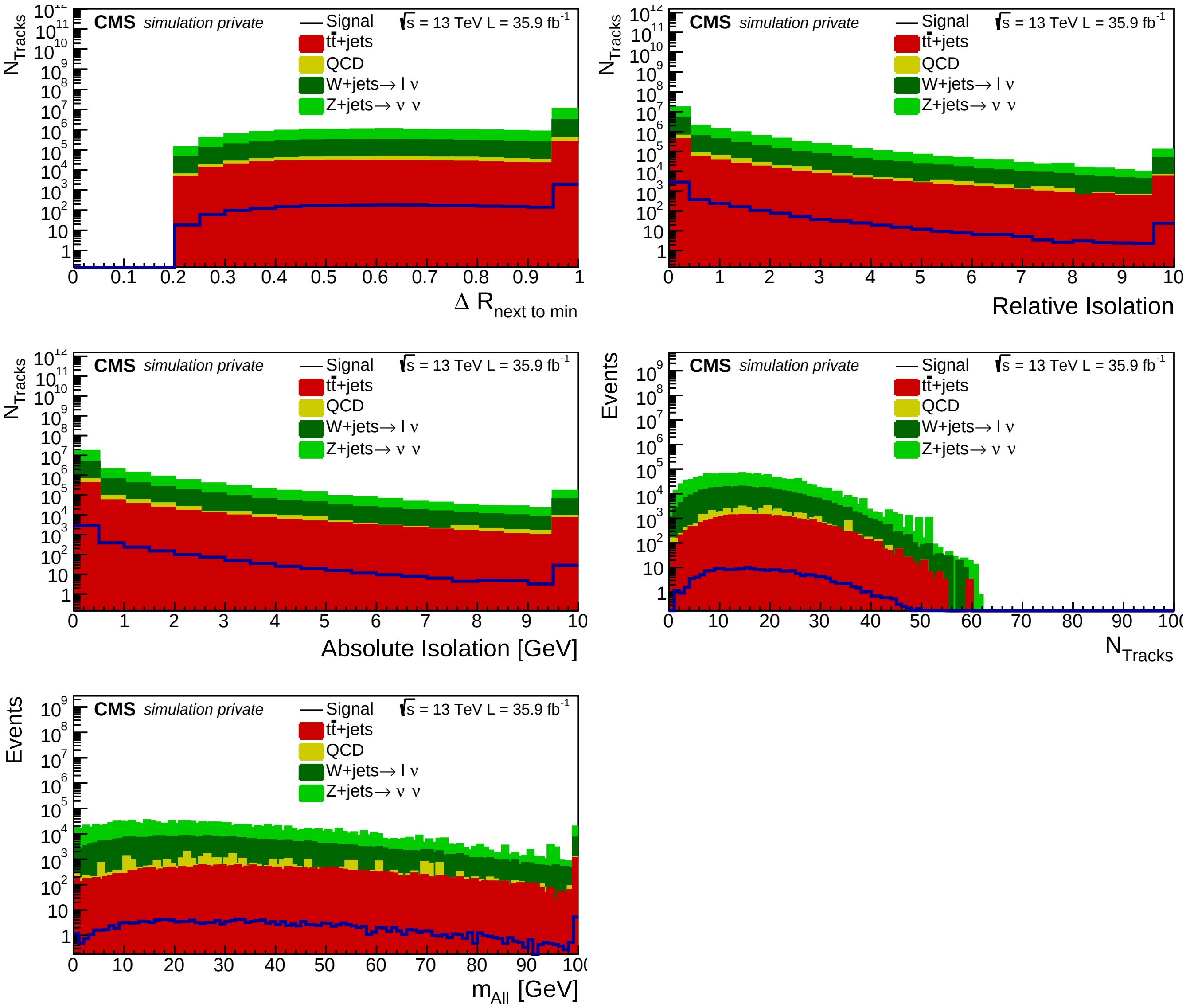

Figure 49: Last three track observables of the track selection optimization and the two event-level quantities with the current track selection. The requirement on $\Delta R^{min}_{Jet,\ Track}$ is tightened to $\Delta R^{min}_{Jet,\ Track} \in [0.4, 3]$ (see Table 10). The track observables shown are $\Delta R_{next\ to\ min}$ (top left), relative Isolation (top right), absolute Isolation (middle left), and the event-level quantities N_{Tracks} (middle right), and m_{All} (bottom).

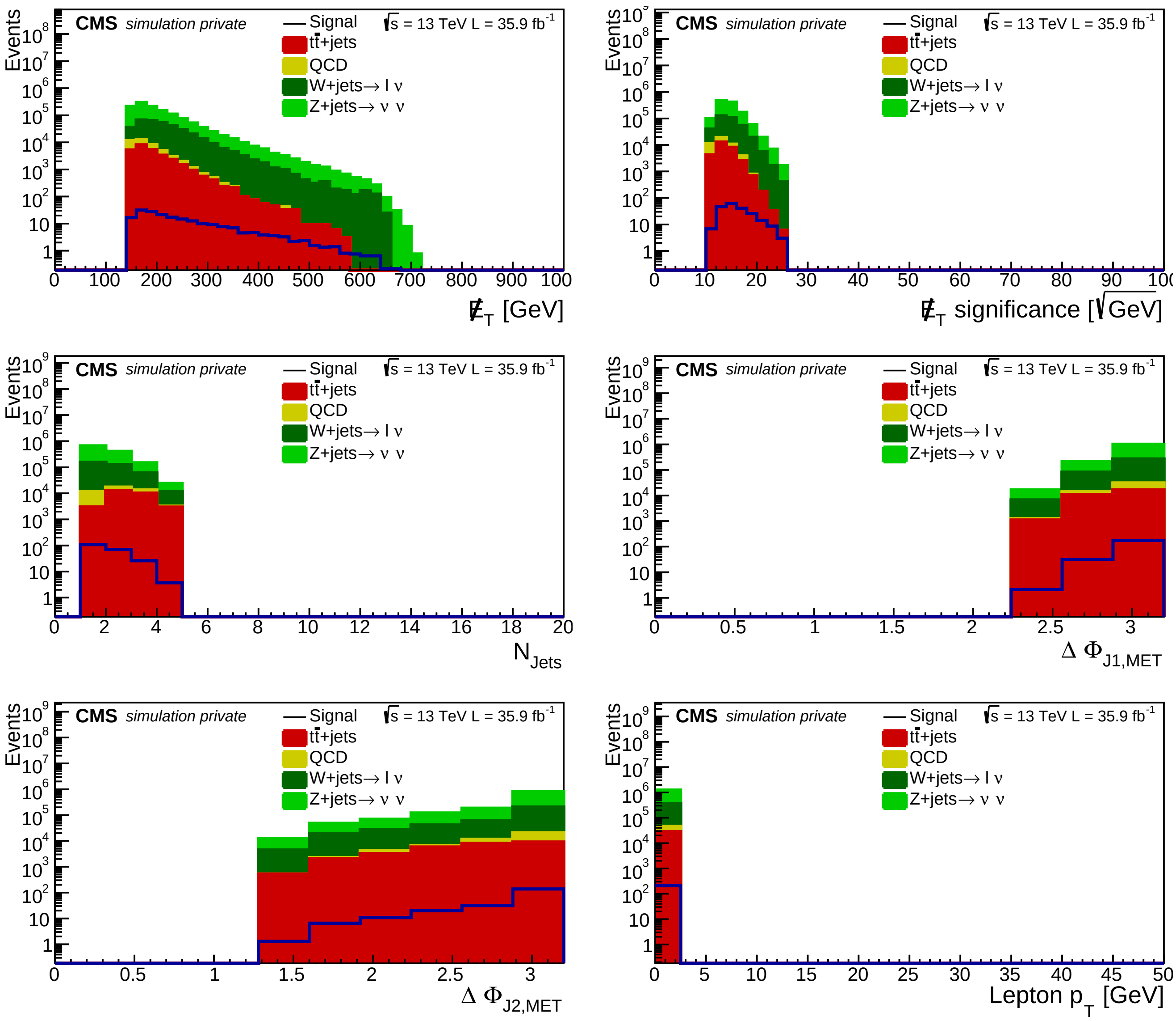

Figure 50: Final event selection distributions.

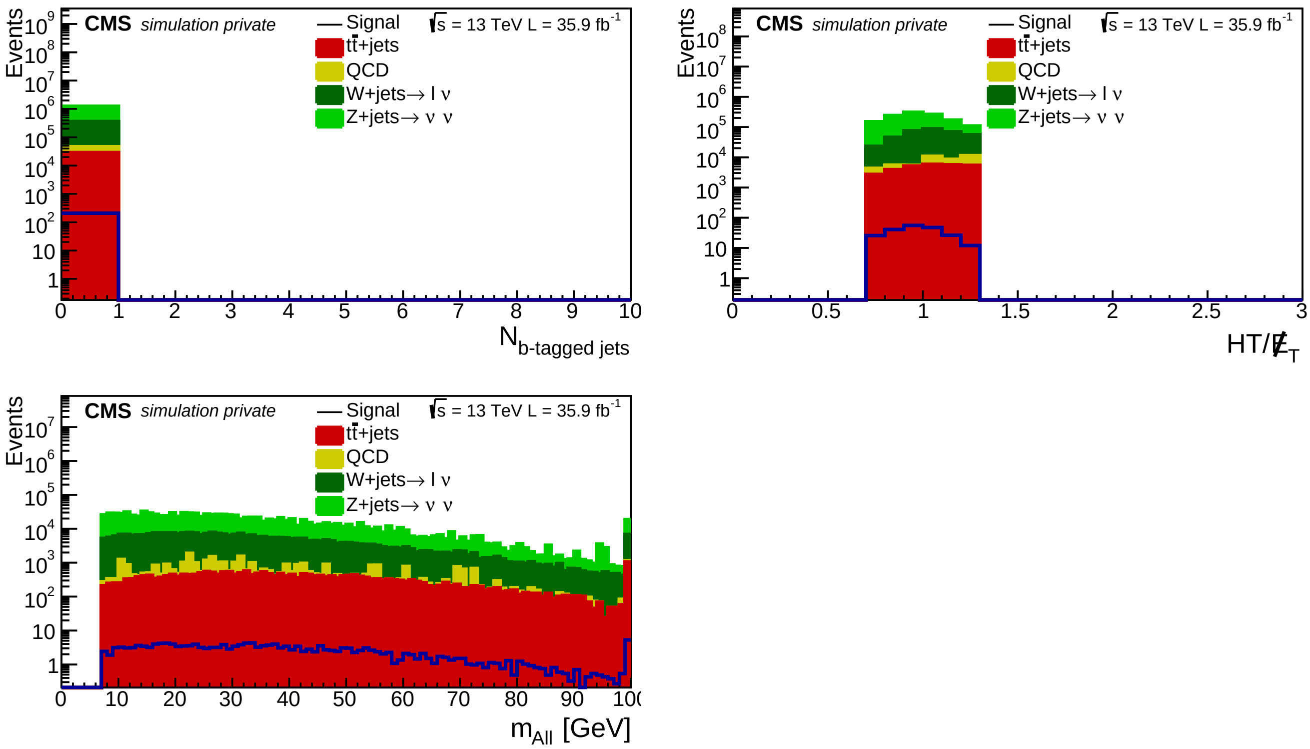

Figure 51: Final event selection distributions.

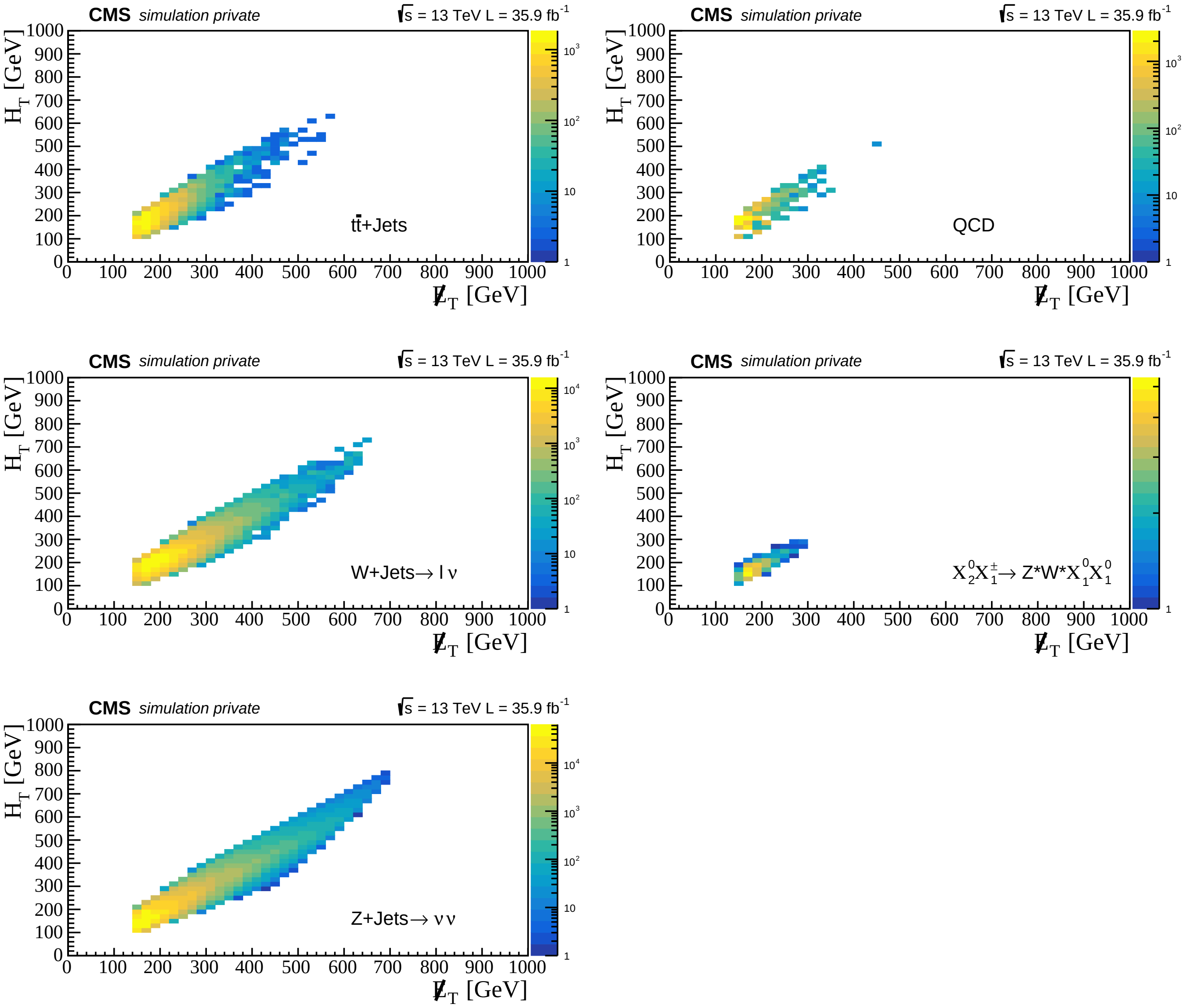

Figure 52: Final event selection distributions

8 Summary, Conclusions and Further Thoughts

This last section contains a summary, the main conclusions of this work, and some further thoughts.

Summary
The goal of the thesis was to use the tool `SmodelS` to find signatures within the pMSSM that warrant more attention, and to design a search for such a signature. To this purpose, `SmodelS` decomposes pMSSM models into their simplified model spectra, and tests the cross section of these simplified models against published results of ATLAS and CMS searches for new physics. Simplified models that are not targeted by CMS and ATLAS, and occur in numerous realizations of the pMSSM are identified in this way, and are the signatures that warrant more attention.

For this study, a set of pMSSM parameter points was studied, taken from a previous CMS analysis. In that analysis, 20 million pMSSM parameter points were considered after incorporating low-energy constraints from e.g. measurements of the anomalous magnetic moment, and constraints from B-meson decays. 7200 of these pMSSM points were randomly selected for simulation studies. The analysis goes on to subject the 7200 points to an extensive set of run I analyses, after which 3700 points remain that are not excluded. Of the 3700 remaining points, a further 90% of points are excluded in the context of a run II analysis [61], leaving a total of 329 non-excluded parameter points. In this thesis, `SmodelS` was used on this set of 329 parameter points.

Simplified models describing a mass degenerate triplet of the gaugino states $\widetilde{\chi}_1^{\pm}$, $\widetilde{\chi}_2^0$, and $\widetilde{\chi}_1^0$, with the $\widetilde{\chi}_1^0$ as the lightest supersymmetric particle, emerged as the most numerous simplified models among the remaining 329 pMSSM parameter points. It was shown that a feature of pMSSM points that contain such a mass degenerate triplet is that they tend to have low levels of fine tuning, as measured in the ΔEW variable. The parameter point with the lowest value of ΔEW was selected for a sensitivity study. Due to the higher mass difference of $\Delta m_{\widetilde{\chi}_2^0, \widetilde{\chi}_1^0} = 13\,\mathrm{GeV}$ compared to $\Delta m_{\widetilde{\chi}_1^{\pm}, \widetilde{\chi}_1^0} = 4.2\,\mathrm{GeV}$, the target signature chosen was that of an off shell Z boson from the decay $\widetilde{\chi}_2^0 \rightarrow Z^* \widetilde{\chi}_1^0$. In this thesis, it was decided to investigate the hadronic decay channel over the leptonic decay channel of the Z^* due to the favorable branching fraction of hadronic decay mode of the Z boson. An event selection using event-level observables, such as $\not{E}_T$ or H_T, could not reduce the Standard Model background to less than three orders of magnitude above the signal. The dominant Standard Model background is the process $Z + \mathrm{Jets} \rightarrow \nu\nu + \mathrm{Jets}$. Two studies regarding the impact of particle level observables were performed. Due to the low reconstruction efficiency of low-energy neutral particles with particle flow, it was decided to use track information only.

First, an optimization with respect to the ratio of the number of selected tracks from Z^* decays to the number of all tracks, $\frac{N_{Z^*\,\text{daughters}}}{N_{\text{Tracks}}}$, was performed in signal events. The best ratio achieved was of order $\mathcal{O}(1)$ for a working point with approximately 6% signal track efficiency and 99.5% background rejection. A second optimization was performed in order to maximize the signal significance Σ in terms of the number of signal and background events, by simultaneously scanning over track variables and a set of event-level observables that included the track multiplicity N_{Tracks}, and the invariant mass of all remaining tracks m_{All}. The method yielded an increase of the signal significance from $\Sigma = 0.1027$ to $\Sigma = 0.1116$, a small effect, which demonstrates the challenge of the hadronic channel of models with a very compressed gaugino spectrum.

Phenomenological Study

After the phenomenological study in Section 6, it is concluded that none of the employed ATLAS and CMS analyses given in Section 5.7 can exclude any of the remaining pMSSM points of the scan by using `SmodelS`. This is not unexpected, as the 329 parameter points that `SmodelS` was used on had already been subjected to an extensive set of run I CMS search results, and a run II result with exceptionally large exclusion power.

The most common missing simplified models that `SmodelS` identifies among the remaining parameter points are simplified models describing compressed gaugino spectra, shown in Figure 24. These compressed gaugino models emerged as very interesting candidates for study, both for their abundance among the pMSSM points and for the fact that they tend to be present in natural versions of the pMSSM (Section 6.3).

`SmodelS` does not contain Mono-X searches, which might well constrain the compressed gaugino models that `SmodelS` identified. To test the robustness of the results of this thesis, the remaining 329 points that were used here should be tested as to their exclusion by a tool that incorporates Mono-X searches, such as CheckMATE [48].

Finally, the parameter scan used here is a very sparse scan, containing only 7200 points in a 19 dimensional parameter space. It is unlikely that such a sparse scan sufficiently represents the whole range of phenomenology of the pMSSM. Additional interesting signatures may well be found using this method on a larger scan.

`SmodelS` is not restricted to the pMSSM, or event SUSY models. Now that the method of finding interesting physics signatures has been shown to work in the case of the pMSSM, it would be interesting to use `SmodelS` with other types of BSM models.

Search for Compressed Gaugino Models in the Hadronic Z^* Decay Channel

A search in the hadronic channel for electroweak gaugino models is dominated by the $\mathrm{Z}+\mathrm{Jets}\rightarrow\nu\nu+\mathrm{Jets}$ and, to a lesser degree, by the $\mathrm{W}+\mathrm{Jets}\rightarrow 1\nu+\mathrm{Jets}$ background. The background is larger than the signal by three to four orders of magnitude. The difficulty with this analysis can be attributed mainly to three factors:

1. The background for this signal model is very large in the hadronic channel.

2. The kinematic signature of the signal process with a small $\Delta m_{\tilde{\chi}_2^0,\tilde{\chi}_1^0}$ is very weak, making it hard to separate from the underlying event. The high masses of the SUSY particles lead to very small boosts of the SUSY system. This in turn leads to low-p_T final states compared the case of lower SUSY masses, as well as isotropic decays of the Z^* in the rest frame of the detector. This makes the signal almost indistinguishable from the underlying event and in turn from the background.

3. The neutral component of the hadronic Z^* decay cannot be reconstructed using tracks. At the same time, the efficiency of the particle flow reconstruction, which also includes the neutral particles, is very small at low energies, owing to thresholds, pileup, and the decreasing resolution of the calorimeters at low energies.

There are a number of prospects improving this search. A possible improvement in the hadronic channel is to try to reconstruct the neutral component of the Z^* decay. If this could be done successfully, the Z^* decay may be easier to distinguish from the underlying event and from the $\mathrm{Z}+\mathrm{Jets}\rightarrow\nu\nu+\mathrm{Jets}$ background.

Furthermore, the leptonic channel of the off shell Z boson should be investigated. It has several advantages over the hadronic channel:

- The main background in the analysis, the $\mathrm{Z}+\mathrm{Jets}\rightarrow\nu\nu+\mathrm{Jets}$ process, is almost completely eliminated by the requirement of a lepton in the event (see Figure 30, bottom right histogram);

- The energy of the leptons from a Z^* decay is higher than the energy of the charged particles in the equivalent hadronic decay;

- Less reliance on the calorimeters, as most of the energy can be associated to a track.

The benchmark model that was analyzed in this thesis has very high masses of the SUSY particles. Models with similar production and decay processes, but with an electroweak gaugino mass spectrum that is shifted down to $m_{\tilde{\chi}_1^0}\approx 160\,\mathrm{GeV}$ remain unexcluded, but may be much more explorable using the techniques described here. There are two main reasons for this:

1. The kinematic signature of the signal process is stronger for smaller SUSY masses. The smaller masses of the SUSY particles lead to a larger Lorentz boost, which directly translates to a larger p_T of the Z^* (and W^*) decay products. Additionally, the boost would modify the angular distribution of the otherwise isotropic Z^* decay, increasing the separation power of angular observables.

2. Smaller SUSY masses lead to larger production cross sections. A larger cross section directly increases the signal significance. In addition to that, the optimization procedures employed in this thesis are held back by the small number of signal events. A larger number of events would allow the selection of a more optimal signal region.

Even disregarding the positive effect on the track momenta that smaller SUSY masses would have, the cross section increase alone would make a huge difference. If one naively uses the cross section of the model TChipChimZoffWoff at masses of $m_{\tilde{\chi}_1^0}$, $m_{\tilde{\chi}_1^\pm}$, and $m_{\tilde{\chi}_2^0}$ of approximately 160 GeV, we would gain a factor of ≈ 20 [42] on the cross section compared to the one that was used in this thesis. This would push the signal significance to at least $\Sigma \approx 2$. Add to that the positive kinematic effects of lower masses of the primary SUSY particles, and it is clear that there is need for further study of this type of simplified model from an analysis perspective.

Concerning the Optimization Method

The simultaneous optimization procedure of event- and track-level observables could not be extensively tested in the context of this analysis, as the tracks produced in signal events offer too little separation power against background events. For obvious reasons, it is expected to perform much better in the context of analyses with higher-energy objects. The method is not limited to tracks in its application. Similar objects like particle flow candidates or jets could be used as well. It is noted that existing tools for signal to background optimization, such as TMVA multivariate classifiers and random grid searches, do not allow for this type of one-stage optimization.

References

[1] M. Thomson. *Modern Particle Physics*. Modern Particle Physics. Cambridge University Press, 2013. ISBN: 9781107034266. URL: `https://books.google.de/books?id=BV1sAAAAQBAJ`.

[2] M.E. Peskin and D.V. Schroeder. *An Introduction To Quantum Field Theory*. Frontiers in Physics. Avalon Publishing, 1995. ISBN: 9780813345437.

[3] L.H. Ryder. *Quantum Field Theory*. Cambridge University Press, 1996. ISBN: 9780521478144.

[4] D. Griffiths. *Introduction to Elementary Particles*. Physics textbook. Wiley, 2008. ISBN: 9783527406012.

[5] C. S. Wu et al. „Experimental Test of Parity Conservation in Beta Decay". In: *Phys. Rev.* 105 (4 1957), pp. 1413–1415. DOI: `10.1103/PhysRev.105.1413`. URL: `https://link.aps.org/doi/10.1103/PhysRev.105.1413`.

[6] MissMJ. *Standard Model of Elementary Particles*. accessed April 12, 2018. URL: `https://upload.wikimedia.org/wikipedia/commons/0/00/Standard_Model_of_Elementary_Particles.svg`.

[7] Latham Boyle. *Standard Model Of Particle Physics–Most Complete Diagram*. accessed April 8, 2018. 2015. URL: `https://commons.wikimedia.org/wiki/File:Standard_Model_Of_Particle_Physics--Most_Complete_Diagram.png`.

[8] D. Binosi and L. Theußl. „JaxoDraw: A graphical user interface for drawing Feynman diagrams". In: *Computer Physics Communications* 161.1 (2004), pp. 76 –86. ISSN: 0010-4655. DOI: `https://doi.org/10.1016/j.cpc.2004.05.001`. URL: `http://www.sciencedirect.com/science/article/pii/S0010465504002115`.

[9] Marc H. Goroff and Augusto Sagnotti. „The ultraviolet behavior of Einstein gravity". In: *Nuclear Physics B* 266.3 (1986), pp. 709 –736. ISSN: 0550-3213. DOI: `https://doi.org/10.1016/0550-3213(86)90193-8`. URL: `http://www.sciencedirect.com/science/article/pii/0550321386901938`.

[10] Gerard 't Hooft and M. J. G. Veltman. „One loop divergencies in the theory of gravitation". In: *Ann. Inst. H. Poincare Phys. Theor.* A20 (1974), pp. 69–94.

[11] Hitoshi Murayama. „Supersymmetry phenomenology". In: *Proceedings, Summer School in Particle Physics: Trieste, Italy, June 21-July 9, 1999*. 2000, pp. 296–335. arXiv: `hep-ph/0002232 [hep-ph]`.

[12] Massimo Persic, Paolo Salucci, and Fulvio Stel. „The Universal rotation curve of spiral galaxies: 1. The Dark matter connection". In: *Mon. Not. Roy. Astron. Soc.* 281 (1996), p. 27. DOI: `10.1093/mnras/281.1.27, 10.1093/mnras/278.1.27`. arXiv: `astro-ph/9506004 [astro-ph]`.

[13] Virginia Trimble. „Existence and Nature of Dark Matter in the Universe“. In: *Annual Review of Astronomy and Astrophysics* 25.1 (1987), pp. 425–472. DOI: 10.1146/annurev.aa.25.090187.002233. eprint: https://doi.org/10.1146/annurev.aa.25.090187.002233. URL: https://doi.org/10.1146/annurev.aa.25.090187.002233.

[14] P. A. R. Ade et al. „Planck 2015 results. XIII. Cosmological parameters“. In: *Astron. Astrophys.* 594 (2016), A13. DOI: 10.1051/0004-6361/201525830. arXiv: 1502.01589 [astro-ph.CO].

[15] Stephen P. Martin. „A Supersymmetry primer“. In: (1997). [Adv. Ser. Direct. High Energy Phys.18,1(1998)], pp. 1–98. DOI: 10.1142/9789812839657_0001, 10.1142/9789814307505_0001. arXiv: hep-ph/9709356 [hep-ph].

[16] Rudolf Haag, Jan T. Łopuszański, and Martin Sohnius. „All possible generators of supersymmetries of the S-matrix“. In: *Nuclear Physics B* 88.2 (1975), pp. 257 –274. ISSN: 0550-3213. DOI: https://doi.org/10.1016/0550-3213(75)90279-5. URL: http://www.sciencedirect.com/science/article/pii/0550321375902795.

[17] Katherine Garrett and Gintaras Duda. „Dark Matter: A Primer“. In: *Adv. Astron.* 2011 (2011), p. 968283. DOI: 10.1155/2011/968283. arXiv: 1006.2483 [hep-ph].

[18] D. I. Kazakov. „Supersymmetry on the Run: LHC and Dark Matter“. In: *Nucl. Phys. Proc. Suppl.* 203-204 (2010), pp. 118–154. DOI: 10.1016/j.nuclphysbps.2010.08.007. arXiv: 1010.5419 [hep-ph].

[19] F. Gabbiani et al. „A Complete analysis of FCNC and CP constraints in general SUSY extensions of the standard model“. In: *Nucl. Phys.* B477 (1996), pp. 321–352. DOI: 10.1016/0550-3213(96)00390-2. arXiv: hep-ph/9604387 [hep-ph].

[20] Maxim Pospelov and Adam Ritz. „Electric dipole moments as probes of new physics“. In: *Annals Phys.* 318 (2005), pp. 119–169. DOI: 10.1016/j.aop.2005.04.002. arXiv: hep-ph/0504231 [hep-ph].

[21] S. Abel, S. Khalil, and O. Lebedev. „EDM constraints in supersymmetric theories“. In: *Nucl. Phys.* B606 (2001), pp. 151–182. DOI: 10.1016/S0550-3213(01)00233-4. arXiv: hep-ph/0103320 [hep-ph].

[22] A. Djouadi et al. „The Minimal supersymmetric standard model: Group summary report“. In: *GDR (Groupement De Recherche) - Supersymetrie Montpellier, France, April 15-17, 1998*. 1998. arXiv: hep-ph/9901246 [hep-ph]. URL: https://inspirehep.net/record/481987/files/arXiv:hep-ph_9901246.pdf.

[23] Daniele Alves. „Simplified Models for LHC New Physics Searches“. In: *J. Phys.* G39 (2012). Ed. by Nima Arkani-Hamed et al., p. 105005. DOI: 10.1088/0954-3899/39/10/105005. arXiv: 1105.2838 [hep-ph].

[24] G. L. Bayatian et al. „CMS Physics“. In: (2006).

[25] The ATLAS Collaboration and G Aad; et al. „The ATLAS Experiment at the CERN Large Hadron Collider“. In: *Journal of Instrumentation* 3.08 (2008), S08003. URL: http://stacks.iop.org/1748-0221/3/i=08/a=S08003.

[26] The CMS Collaboration and S Chatrchyan; et al. „The CMS experiment at the CERN LHC“. In: *Journal of Instrumentation* 3.08 (2008), S08004. URL: http://stacks.iop.org/1748-0221/3/i=08/a=S08004.

[27] LHCb Collaboration. URL: http://lhcb.web.cern.ch/lhcb/.

[28] ALICE Collaboration. URL: http://alice-collaboration.web.cern.ch/.

[29] The TOTEM Collaboration and G Anelli; et al. „The TOTEM Experiment at the CERN Large Hadron Collider“. In: *Journal of Instrumentation* 3.08 (2008), S08007. URL: http://stacks.iop.org/1748-0221/3/i=08/a=S08007.

[30] The LHCf Collaboration and O Adriani; et al. „The LHCf detector at the CERN Large Hadron Collider“. In: *Journal of Instrumentation* 3.08 (2008), S08006. URL: http://stacks.iop.org/1748-0221/3/i=08/a=S08006.

[31] James Pinfold et al. „Technical Design Report of the MoEDAL Experiment“. In: (2009).

[32] Christiane Lefèvre. „The CERN accelerator complex. Complexe des accélérateurs du CERN“. 2008. URL: https://cds.cern.ch/record/1260465.

[33] Tai Sakuma and Thomas McCauley. „Detector and Event Visualization with SketchUp at the CMS Experiment“. In: *Journal of Physics: Conference Series* 513.2 (2014), p. 022032. URL: http://stacks.iop.org/1742-6596/513/i=2/a=022032.

[34] The CMS Collaboration. „Description and performance of track and primary-vertex reconstruction with the CMS tracker“. In: *Journal of Instrumentation* 9.10 (2014), P10009. URL: http://stacks.iop.org/1748-0221/9/i=10/a=P10009.

[35] A. M. Sirunyan et al. „Particle-flow reconstruction and global event description with the CMS detector“. In: *JINST* 12.10 (2017), P10003. DOI: 10.1088/1748-0221/12/10/P10003. arXiv: 1706.04965 [physics.ins-det].

[36] Matteo Cacciari, Gavin P. Salam, and Gregory Soyez. „The Anti-k(t) jet clustering algorithm“. In: *JHEP* 04 (2008), p. 063. DOI: 10.1088/1126-6708/2008/04/063. arXiv: 0802.1189 [hep-ph].

[37] CMS Collaboration. „Jet energy scale uncertainty correlations between ATLAS and CMS at 8 TeV“. In: (2015).

[38] Vardan Khachatryan et al. „Jet energy scale and resolution in the CMS experiment in pp collisions at 8 TeV“. In: *JINST* 12.02 (2017), P02014. DOI: 10.1088/1748-0221/12/02/P02014. arXiv: 1607.03663 [hep-ex].

[39] CMS Collaboration. „Identification of b quark jets at the CMS Experiment in the LHC Run 2“. In: (2016).

[40] J. Alwall et al. „The automated computation of tree-level and next-to-leading order differential cross sections, and their matching to parton shower simulations“. In: *JHEP* 07 (2014), p. 079. DOI: 10.1007/JHEP07(2014)079. arXiv: 1405.0301 [hep-ph].

[41] Torbjörn Sjöstrand et al. „An Introduction to PYTHIA 8.2“. In: *Comput. Phys. Commun.* 191 (2015), pp. 159–177. DOI: 10.1016/j.cpc.2015.01.024. arXiv: 1410.3012 [hep-ph].

[42] *LHC SUSY Cross Section Working Group*. URL: https://twiki.cern.ch/twiki/bin/view/LHCPhysics/SUSYCrossSections.

[43] Benjamin Fuks et al. „Gaugino production in proton-proton collisions at a center-of-mass energy of 8 TeV“. In: *JHEP* 10 (2012), p. 081. DOI: 10.1007/JHEP10(2012)081. arXiv: 1207.2159 [hep-ph].

[44] Benjamin Fuks et al. „Precision predictions for electroweak superpartner production at hadron colliders with RESUMMINO“. In: *Eur. Phys. J. C* 73 (2013), p. 2480. DOI: 10.1140/epjc/s10052-013-2480-0. arXiv: 1304.0790 [hep-ph].

[45] Federico Ambrogi et al. „SModelS v1.1 user manual“. In: (2017). arXiv: 1701.06586 [hep-ph].

[46] Sabine Kraml et al. „SModelS: a tool for interpreting simplified-model results from the LHC and its application to supersymmetry“. In: *Eur.Phys.J.* C74 (2014), p. 2868. DOI: 10.1140/epjc/s10052-014-2868-5. arXiv: 1312.4175 [hep-ph].

[47] http://smodels.hephy.at.

[48] Manuel Drees et al. „CheckMATE: Confronting your Favourite New Physics Model with LHC Data“. In: *Comput. Phys. Commun.* 187 (2015), pp. 227–265. DOI: 10.1016/j.cpc.2014.10.018. arXiv: 1312.2591 [hep-ph].

[49] Daniel Dercks et al. „CheckMATE 2: From the model to the limit“. In: *Comput. Phys. Commun.* 221 (2017), pp. 383–418. DOI: 10.1016/j.cpc.2017.08.021. arXiv: 1611.09856 [hep-ph].

[50] Peter Z. Skands et al. „SUSY Les Houches accord: Interfacing SUSY spectrum calculators, decay packages, and event generators“. In: *JHEP* 0407 (2004), p. 036. DOI: 10.1088/1126-6708/2004/07/036. arXiv: hep-ph/0311123 [hep-ph].

[51] Johan Alwall et al. „A Standard format for Les Houches event files“. In: *Comput.Phys.Commun.* 176 (2007), pp. 300–304. DOI: 10.1016/j.cpc.2006.11.010. arXiv: hep-ph/0609017 [hep-ph].

[52] Serguei Chatrchyan et al. „Interpretation of Searches for Supersymmetry with simplified Models“. In: *Phys. Rev.* D88.5 (2013), p. 052017. DOI: 10.1103/PhysRevD.88.052017. arXiv: 1301.2175 [hep-ex].

[53] Torbjorn Sjostrand, Stephen Mrenna, and Peter Z. Skands. „PYTHIA 6.4 Physics and Manual". In: *JHEP* 0605 (2006), p. 026. DOI: 10.1088/1126-6708/2006/05/026. arXiv: hep-ph/0603175 [hep-ph].

[54] W. Beenakker et al. „Squark and gluino production at hadron colliders". In: *Nucl.Phys.* B492 (1997), pp. 51–103. DOI: 10.1016/S0550-3213(97)80027-2. arXiv: hep-ph/9610490 [hep-ph].

[55] W. Beenakker et al. „Stop production at hadron colliders". In: *Nucl.Phys.* B515 (1998), pp. 3–14. DOI: 10.1016/S0550-3213(98)00014-5. arXiv: hep-ph/9710451 [hep-ph].

[56] A. Kulesza and L. Motyka. „Threshold resummation for squark-antisquark and gluino-pair production at the LHC". In: *Phys.Rev.Lett.* 102 (2009), p. 111802. DOI: 10.1103/PhysRevLett.102.111802. arXiv: 0807.2405 [hep-ph].

[57] A. Kulesza and L. Motyka. „Soft gluon resummation for the production of gluino-gluino and squark-antisquark pairs at the LHC". In: *Phys.Rev.* D80 (2009), p. 095004. DOI: 10.1103/PhysRevD.80.095004. arXiv: 0905.4749 [hep-ph].

[58] Wim Beenakker et al. „Soft-gluon resummation for squark and gluino hadroproduction". In: *JHEP* 0912 (2009), p. 041. DOI: 10.1088/1126-6708/2009/12/041. arXiv: 0909.4418 [hep-ph].

[59] Wim Beenakker et al. „Supersymmetric top and bottom squark production at hadron colliders". In: *JHEP* 1008 (2010), p. 098. DOI: 10.1007/JHEP08(2010)098. arXiv: 1006.4771 [hep-ph].

[60] W. Beenakker et al. „Squark and Gluino Hadroproduction". In: *Int.J.Mod.Phys.* A26 (2011), pp. 2637–2664. DOI: 10.1142/S0217751X11053560. arXiv: 1105.1110 [hep-ph].

[61] Albert M Sirunyan et al. „Search for supersymmetry in multijet events with missing transverse momentum in proton-proton collisions at 13 TeV". In: *Phys. Rev.* D96.3 (2017), p. 032003. DOI: 10.1103/PhysRevD.96.032003. arXiv: 1704.07781 [hep-ex].

[62] *Search for top squarks in multijet events with large missing momentum in proton-proton collisions at 8 TeV*. Tech. rep. CMS-PAS-SUS-13-015. Geneva: CERN, 2013. URL: http://cds.cern.ch/record/1635353.

[63] Georges Aad et al. „Search for top squark pair production in final states with one isolated lepton, jets, and missing transverse momentum in $\sqrt{s} = 8$ TeV pp collisions with the ATLAS detector". In: *JHEP* 11 (2014), p. 118. DOI: 10.1007/JHEP11(2014)118. arXiv: 1407.0583 [hep-ex].

[64] *Search for supersymmetry in pp collisions at sqrt(s) = 8 Tev in events with two opposite sign leptons, large number of jets, b-tagged jets, and large missing transverse energy.* Tech. rep. CMS-PAS-SUS-13-016. Geneva: CERN, 2013. URL: http://cds.cern.ch/record/1623818.

[65] *Search for strongly produced superpartners in final states with two same sign leptons with the ATLAS detector using 21 fb-1 of proton-proton collisions at $\sqrt{s} = 8$ TeV.* Tech. rep. ATLAS-CONF-2013-007. Geneva: CERN, 2013. URL: http://cds.cern.ch/record/1522430.

[66] *Search for direct production of bottom squark pairs.* Tech. rep. CMS-PAS-SUS-13-018. Geneva: CERN, 2014. URL: https://cds.cern.ch/record/1693164.

[67] *Search for strong production of supersymmetric particles in final states with missing transverse momentum and at least three b-jets using 20.1 fb-1 of pp collisions at sqrt(s) = 8 TeV with the ATLAS Detector.* Tech. rep. ATLAS-CONF-2013-061. Geneva: CERN, 2013. URL: http://cds.cern.ch/record/1557778.

[68] *A Search for Scalar Top Quark Production and Decay to All Hadronic Final States in pp Collisions at sqrt(s) = 8 TeV.* Tech. rep. CMS-PAS-SUS-13-023. Geneva: CERN, 2015. URL: http://cds.cern.ch/record/2044441.

[69] *Search for strongly produced supersymmetric particles in decays with two leptons at $\sqrt{s}$ = 8 TeV.* Tech. rep. ATLAS-CONF-2013-089. Geneva: CERN, 2013. URL: http://cds.cern.ch/record/1595272.

[70] CMS collaboration. „Search for gluino mediated bottom- and top-squark production in multijet final states in pp collisions at 8 TeV“. In: *Phys. Lett. B* 725.arXiv:1305.2390. CMS-SUS-12-024. CERN-PH-EP-2013-076 (2013), 243–270. 39 p. URL: https://cds.cern.ch/record/1546693.

[71] Georges Aad et al. „Search for squarks and gluinos with the ATLAS detector in final states with jets and missing transverse momentum using $\sqrt{s} = 8$ TeV proton–proton collision data“. In: *JHEP* 09 (2014), p. 176. DOI: 10.1007/JHEP09(2014)176. arXiv: 1405.7875 [hep-ex].

[72] CMS collaboration. „Search for supersymmetry in hadronic final states with missing transverse energy using the variables α_T and b-quark multiplicity in pp collisions at $\sqrt{s} = 8$ TeV“. In: *Eur. Phys. J. C* 73.CMS-SUS-12-028. CMS-SUS-12-028. CERN-PH-EP-2013-037 (2013), 2568. 45 p. URL: https://cds.cern.ch/record/1527115.

[73] Georges Aad et al. „Search for new phenomena in final states with large jet multiplicities and missing transverse momentum at $\sqrt{s} = 8$ TeV proton-proton collisions using the ATLAS experiment“. In: *JHEP* 10 (2013). [Erratum: JHEP01,109(2014)], p. 130. DOI: 10.1007/JHEP10(2013)130, 10.1007/JHEP01(2014)109. arXiv: 1308.1841 [hep-ex].

[74] CMS collaboration. „Search for anomalous production of events with three or more leptons in pp collisions at $\sqrt{s} = 8$ TeV“. In: *Phys. Rev. D* 90.arXiv:1404.5801. CMS-SUS-13-002-003. CERN-PH-EP-2014-039 (2014), 032006. 43 p. URL: `https://cds.cern.ch/record/1696925`.

[75] Georges Aad et al. „Search for direct third-generation squark pair production in final states with missing transverse momentum and two b-jets in $\sqrt{s} = 8$ TeV pp collisions with the ATLAS detector“. In: *JHEP* 10 (2013), p. 189. DOI: `10.1007/JHEP10(2013)189`. arXiv: `1308.2631 [hep-ex]`.

[76] CMS collaboration. „Search for supersymmetry using razor variables in events with b-tagged jets in pp collisions at $\sqrt{s} = 8$ TeV“. In: *Phys. Rev. D* 91.arXiv:1502.00300. CERN-PH-EP-2015-005. CMS-SUS-13-004 (2015), 052018. 45 p. URL: `https://cds.cern.ch/record/1984165`.

[77] Georges Aad et al. „Search for direct top squark pair production in events with a Z boson, b-jets and missing transverse momentum in sqrt(s)=8 TeV pp collisions with the ATLAS detector“. In: *Eur. Phys. J.* C74.6 (2014), p. 2883. DOI: `10.1140/epjc/s10052-014-2883-6`. arXiv: `1403.5222 [hep-ex]`.

[78] CMS collaboration. „Searches for electroweak production of charginos, neutralinos, and sleptons decaying to leptons and W, Z, and Higgs bosons in pp collisions at 8 TeV“. In: *Eur. Phys. J. C* 74.arXiv:1405.7570. CMS-SUS-13-006. CERN-PH-EP-2014-098 (2014), 3036. 61 p. URL: `https://cds.cern.ch/record/1704963`.

[79] Georges Aad et al. „Search for supersymmetry at $\sqrt{s} = 8$ TeV in final states with jets and two same-sign leptons or three leptons with the ATLAS detector“. In: *JHEP* 06 (2014), p. 035. DOI: `10.1007/JHEP06(2014)035`. arXiv: `1404.2500 [hep-ex]`.

[80] *Search for Supersymmetry in pp collisions at 8 TeV in events with a single lepton, multiple jets and b-tags*. Tech. rep. CMS-PAS-SUS-13-007. Geneva: CERN, 2013. URL: `http://cds.cern.ch/record/1523786`.

[81] Georges Aad et al. „Search for direct production of charginos, neutralinos and sleptons in final states with two leptons and missing transverse momentum in pp collisions at $\sqrt{s} = 8$ TeV with the ATLAS detector“. In: *JHEP* 05 (2014), p. 071. DOI: `10.1007/JHEP05(2014)071`. arXiv: `1403.5294 [hep-ex]`.

[82] CMS collaboration. „Search for top-squark pair production in the single-lepton final state in pp collisions at $\sqrt{s} = 8$ TeV“. In: *Eur. Phys. J. C* 73.arXiv:1308.1586. CMS-SUS-13-011. CERN-PH-EP-2013-148 (2013), 2677. 61 p. URL: `https://cds.cern.ch/record/1567175`.

[83] Georges Aad et al. „Search for direct production of charginos and neutralinos in events with three leptons and missing transverse momentum in $\sqrt{s} = 8$ TeV pp collisions with the ATLAS detector“. In: *JHEP* 04 (2014), p. 169. DOI: `10.1007/JHEP04(2014)169`. arXiv: `1402.7029 [hep-ex]`.

[84] CMS collaboration. „Search for new physics in the multijet and missing transverse momentum final state in proton-proton collisions at $\sqrt{s} = 8$ TeV“. In: *JHEP* 06.arXiv:1402.4770. CMS-SUS-13-012. CERN-PH-EP-2014-015 (2014), 055. 37 p. URL: `https://cds.cern.ch/record/1662652`.

[85] CMS collaboration. „Search for new physics in events with same-sign dileptons and jets in pp collisions at $\sqrt{s} = 8$ TeV“. In: *JHEP* 01.arXiv:1311.6736. CMS-SUS-13-013. CERN-PH-EP-2013-213 (2013), 163. 43 p. URL: `https://cds.cern.ch/record/1631468`.

[86] Georges Aad et al. „Search for direct pair production of the top squark in all-hadronic final states in proton-proton collisions at $\sqrt{s} = 8$ TeV with the ATLAS detector“. In: *JHEP* 09 (2014), p. 015. DOI: `10.1007/JHEP09(2014)015`. arXiv: `1406.1122 [hep-ex]`.

[87] CMS collaboration. „Searches for supersymmetry using the M_{T2} variable in hadronic events produced in pp collisions at 8 TeV“. In: *JHEP* 05.arXiv:1502.04358. CMS-SUS-13-019. CERN-PH-EP-2015-017 (2015), 078. 51 p. URL: `https://cds.cern.ch/record/1989788`.

[88] Georges Aad et al. „Search for strong production of supersymmetric particles in final states with missing transverse momentum and at least three b-jets at $\sqrt{s} = 8$ TeV proton-proton collisions with the ATLAS detector“. In: *JHEP* 10 (2014), p. 024. DOI: `10.1007/JHEP10(2014)024`. arXiv: `1407.0600 [hep-ex]`.

[89] CMS collaboration. „Searches for supersymmetry based on events with b jets and four W bosons in pp collisions at 8 TeV“. In: *Phys. Lett. B* 745.arXiv:1412.4109. CERN-PH-EP-2014-286. CMS-SUS-14-010 (2014), 5. 35 p. URL: `http://cds.cern.ch/record/1976453`.

[90] Georges Aad et al. „Search for direct top-squark pair production in final states with two leptons in pp collisions at $\sqrt{s} = 8$ TeV with the ATLAS detector“. In: *JHEP* 06 (2014), p. 124. DOI: `10.1007/JHEP06(2014)124`. arXiv: `1403.4853 [hep-ex]`.

[91] CMS collaboration. „Search for supersymmetry in events with soft leptons, low jet multiplicity, and missing transverse energy in proton-proton collisions at $\sqrt{s} = 8$ TeV“. In: *Phys. Lett. B* 759.CMS-SUS-14-021. CERN-PH-EP-2015-307. CMS-SUS-14-021 (2015), 9–35. 40 p. URL: `https://cds.cern.ch/record/2117955`.

[92] Georges Aad et al. „Search for pair-produced third-generation squarks decaying via charm quarks or in compressed supersymmetric scenarios in pp collisions at $\sqrt{s} =$ 8 TeV with the ATLAS detector“. In: *Phys. Rev.* D90.5 (2014), p. 052008. DOI: `10.1103/PhysRevD.90.052008`. arXiv: `1407.0608 [hep-ex]`.

[93] Georges Aad et al. „Search for direct pair production of a chargino and a neutralino decaying to the 125 GeV Higgs boson in $\sqrt{s} = 8$ TeV pp collisions with the ATLAS detector“. In: *Eur. Phys. J.* C75.5 (2015), p. 208. DOI: 10.1140/epjc/s10052-015-3408-7. arXiv: 1501.07110 [hep-ex].

[94] Georges Aad et al. „Search for Scalar Charm Quark Pair Production in pp Collisions at $\sqrt{s} = 8$ TeV with the ATLAS Detector“. In: *Phys. Rev. Lett.* 114.16 (2015), p. 161801. DOI: 10.1103/PhysRevLett.114.161801. arXiv: 1501.01325 [hep-ex].

[95] *Search for supersymmetry in events with jets and missing transverse momentum in proton-proton collisions at 13 TeV*. Tech. rep. CMS-PAS-SUS-16-014. Geneva: CERN, 2016. URL: https://cds.cern.ch/record/2205158.

[96] Morad Aaboud et al. „Search for bottom squark pair production in proton–proton collisions at $\sqrt{s} = 13$ TeV with the ATLAS detector“. In: *Eur. Phys. J.* C76.10 (2016), p. 547. DOI: 10.1140/epjc/s10052-016-4382-4. arXiv: 1606.08772 [hep-ex].

[97] *Search for new physics in the all-hadronic final state with the MT2 variable*. Tech. rep. CMS-PAS-SUS-16-015. Geneva: CERN, 2016. URL: https://cds.cern.ch/record/2205162.

[98] Morad Aaboud et al. „Search for top squarks in final states with one isolated lepton, jets, and missing transverse momentum in $\sqrt{s} = 13$ TeV pp collisions with the ATLAS detector“. In: *Phys. Rev.* D94.5 (2016), p. 052009. DOI: 10.1103/PhysRevD.94.052009. arXiv: 1606.03903 [hep-ex].

[99] *An inclusive search for new phenomena in final states with one or more jets and missing transverse momentum at 13 TeV with the AlphaT variable*. Tech. rep. CMS-PAS-SUS-16-016. Geneva: CERN, 2016. URL: https://cds.cern.ch/record/2205163.

[100] Morad Aaboud et al. „Search for squarks and gluinos in final states with jets and missing transverse momentum at $\sqrt{s} = 13$ TeV with the ATLAS detector“. In: *Eur. Phys. J.* C76.7 (2016), p. 392. DOI: 10.1140/epjc/s10052-016-4184-8. arXiv: 1605.03814 [hep-ex].

[101] *Search for supersymmetry in events with one lepton and multiple jets in proton-proton collisions at $\sqrt{s} = 13$ TeV in 2016*. Tech. rep. CMS-PAS-SUS-16-019. Geneva: CERN, 2016. URL: https://cds.cern.ch/record/2204932.

[102] Georges Aad et al. „Search for supersymmetry at $\sqrt{s} = 13$ TeV in final states with jets and two same-sign leptons or three leptons with the ATLAS detector“. In: *Eur. Phys. J.* C76.5 (2016), p. 259. DOI: 10.1140/epjc/s10052-016-4095-8. arXiv: 1602.09058 [hep-ex].

[103] *Search for SUSY with multileptons in 13 TeV data*. Tech. rep. CMS-PAS-SUS-16-022. Geneva: CERN, 2016. URL: https://cds.cern.ch/record/2205165.

[104] CMS collaboration. „Search for new physics in same-sign dilepton events in proton-proton collisions at $\sqrt{s} = 13$ TeV“. In: *Eur. Phys. J. C* 76.CMS-SUS-15-008. CMS-SUS-15-008. CERN-EP-2016-119 (2016), 439. 40 p. URL: `https://cds.cern.ch/record/2151851`.

[105] Vardan Khachatryan et al. „Phenomenological MSSM interpretation of CMS searches in pp collisions at sqrt(s) = 7 and 8 TeV“. In: *JHEP* 10 (2016), p. 129. DOI: `10.1007/JHEP10(2016)129`. arXiv: `1606.03577 [hep-ex]`.

[106] Albert M Sirunyan et al. „Search for new phenomena with the M_{T2} variable in the all-hadronic final state produced in proton–proton collisions at $\sqrt{s} = 13$ TeV“. In: *Eur. Phys. J.* C77.10 (2017), p. 710. DOI: `10.1140/epjc/s10052-017-5267-x`. arXiv: `1705.04650 [hep-ex]`.

[107] Howard Baer, Vernon Barger, and Maren Padeffke-Kirkland. „Electroweak versus high scale finetuning in the 19-parameter SUGRA model“. In: *Phys. Rev.* D88 (2013), p. 055026. DOI: `10.1103/PhysRevD.88.055026`. arXiv: `1304.6732 [hep-ph]`.

Erklärung

Hiermit bestätige ich, dass die vorliegende Arbeit von mir selbständig verfasst wurde und ich keine anderen als die angegebenen Hilfsmittel – insbesondere keine im Quellenverzeichnis nicht benannten Internet-Quellen – benutzt habe und die Arbeit von mir vorher nicht einem anderen Prüfungsverfahren eingereicht wurde. Die eingereichte schriftliche Fassung entspricht der auf dem elektronischen Speichermedium. Ich bin damit einverstanden, dass die Masterarbeit veröffentlicht wird.

....	....
Ort, Datum	Unterschrift